NORTHWESTERN UNIVERSITY

Reconfigurable Nanostructures from Wrinkling of Soft Skin Materials

A DISSERTATION

SUBMITTED TO THE GRADUATE SCHOOL
IN PARTIAL FULFILLMENT OF THE REQUIREMENTS

for the degree

DOCTOR OF PHILOSOPHY

Field of Materials Science and Engineering

By

Dongjoon Rhee

EVANSTON, ILLINOIS

March 2021

ABSTRACT

Reconfigurable Nanostructures from Wrinkling of Soft Skin Materials

Dongjoon Rhee

Surface patterns that can reconfigure under external stimuli are important for tailoring diverse properties such as surface adhesion, optical transmittance, and wettability depending on the feature size and orientation. Wrinkling a stiff skin layer on a pre-strained elastomer substrate has emerged as a method to create responsive structures without using complex lithographic processes involving multistep masking and etching. Most efforts to fabricate wrinkles used metal or silica films as skin layers with Young's moduli much larger than the substrate. This hard-skin-based approach, however, has limited control over functional responses of the patterned surface because (1) the skin/substrate system cannot readily access nanoscale textures and (2) cracks form at random locations in the skin layer and prevent precise tuning of properties. Although cracks can be suppressed by using softer polymer skin layers, solution-based coating techniques commonly used to form these layers have limited control over the film thickness and the resulting wrinkle wavelength.

This dissertation presents mechano-responsive wrinkles based on chemical vapor deposition of polymer skin materials. Soft fluoropolymer layers resulting from fluorine-containing plasma treatment allowed for switching of wrinkle orientation without crack formation or delamination at high tensile strains. The plasma process featured nanometer-scale tunability in skin thickness necessary for engineering the wrinkle wavelength both in nano- and micrometer regimes. Because the soft skin layer formed a robust interface with two-dimensional electronic materials, the

composite skin exhibited conformal wrinkles that can switch orientation with suppressed crack formation. By patterning local thicknesses of soft skin layers or applying sequential wrinkling processes, we could design structural hierarchy of the patterns in-plane or out-of-plane. With control over characteristic feature sizes and orientations at multiple length scales, our strategy can serve as a promising bottom-up strategy to support a range of functional responses for applications in water harvesting systems, antibacterial fouling surfaces, nanoelectronics, and nanophotonics.

ACKNOWLEDGEMENTS

I would like to start by extending my sincere gratitude to Prof. Teri W. Odom for her support and guidance over the past five years. I am very thankful that she took me in her group after I did not make a satisfactory research progress during my first year in another group. Without her willingness to trust my potential and to offer me a chance to continue research, I would not have been able to finish my Ph.D. studies at Northwestern. Prof. Odom has provided rigorous training that help me think bigger and more creatively to initiate good scientific projects. She also has been a good role model for me to develop my skills to pursue high impact research: I learned a lot from her how to manage a research group and external collaborations for producing outcomes and to communicate data in the form of manuscript and scientific presentation.

I thank my thesis committee members, Prof. Lincoln J. Lauhon, Prof. Jiaxing Huang, and Prof. George C. Schatz for their critical feedback and insightful advice that helped me make progress in my research. I am especially thankful for Prof. Lauhon for giving me a second chance to continue my work at Northwestern after my first year. I thank Prof. Huang, who offered me to a chance to join his group when my advisor selection process did not work. I also thank Prof. Schatz, who did not know me but gladly became my committee member without hesitation.

I also would like to acknowledge Odom group members and other collaborators who made my academic journey more enjoyable. First, I appreciate Dr. Mark D. Huntington, Dr. Clifford J. Engel, and Dr. Won-Kyu Lee for initiating the nanowrinkles research in the Odom group, which has been vital to my Ph.D. study. Especially, Won-Kyu served as a great mentor for me to gain technical expertise and scientific insights. I also thank Dr. Shikai Deng, Young-Ah Lucy Lee, and Jenny

Gyeongbae Park, Dr. Jung Sik Kim, Seunghwan Kim, Youngbin Suh, Jinhwan Kim, Brian Eunhwan Lee, Bumhee Lee, and Taeshik Yoon. I also want to appreciate non-Korean friends at Northwestern especially Dr. Xiaomi Zhang, Annie Tran, Alane Lim, Dr. Nick Wagner, Prof. Kevin Chiou, Dr. Kazi Sadman, Anthony Krenselewski, Dr. Shengshuang Zhu, Travis Schmauss, Dr. Justin Finkle, and Dr. Carissa Heath.

Lastly and most importantly, I want to thank my family for their love and support. My father Joonwoo Rhee and mother Youngnam Rhee have always believed in my abilities and decisions related to my career. I am grateful that my younger brother Donghyun Rhee stays with my parents and provides them emotional support while I am absent for studying abroad. Finally, I thank my grandfather and eldest uncle who influenced me, through their career, to discover my aptitude for science and engineering from my childhood and devote myself to build fundamentals in a variety of fields including solid state physics, materials science, nano- and microelectronics, phonics, plasmonics, mechanics, polymer physics and chemistry, surface engineering, electrochemistry, and chemical engineering throughout my undergraduate and graduate studies. Thank you all.

LIST OF ABBREVIATIONS

1D	One-dimensional
2D	Two-dimensional
3D	Three-dimensional
AFM	Atomic force microscopy
Al	Aluminum
ASTM	American Society for Testing Materials standards
Au	Gold
C	Carbon
CdS	Cadmium sulfide
CdSe	Cadmium selenide
CF_x	Fluoropolymer
Cr	Chromium
Cu	Copper
CVD	Chemical vapor deposition
F	Fluorine
FEM	Finite element method
FFT	Fast Fourier transform
FWHM	Full width at half maximum
G	Generation
G1	First generation

G2	Second generation
G3	Third generation
Gn	n-th generation
IPA	Isopropyl alcohol
MoS_2	Molybdenum disulfide
O	Oxygen
PBS	Phosphate buffered saline
Pd	Palladium
PDMS	Polydimethylsiloxane
PET	Poly(ethylene terephthalate)
PL	Photoluminescence
PMMA	Poly(methyl methacrylate)
PR	Photoresist
PS	Polystyrene
Pt	Platinum
PVA	Poly(vinyl alcohol)
PVP	Polyvinylpyrrolidone
QD	Quantum dot
RIE	Reactive ion etching
S. aureus	*Staphylococcus aureus*
SEM	Scanning electron microscopy
Si	Silicon
SiO_2	Silicon dioxide

SiO$_x$	Silica
TSB	Tryptic soy broth
UV-CF$_x$	Ultraviolet-curable fluoropolymer
XPS	X-ray photoelectron spectroscopy
XRR	X-ray reflectivity

TABLE OF CONTENTS

LIST OF TABLES

LIST OF FIGURES

Chapter 1

Introduction to Reconfigurable Soft Skin Wrinkles

Wrinkling skin layers on pre-strained polymer sheets has drawn significant interest as a method to create reconfigurable surface patterns. Compared to widely studied metal or silica films, softer polymer skins are more tolerant to crack formation when the surface topography is tuned under applied strain. This Mini-review discusses recent progress in mechano-responsive wrinkles based on polymer skin materials. Control over the skin thickness with nanometer accuracy allows for tuning of the wrinkle wavelength and orientation over length scales from nanometer to micrometer regimes. Furthermore, soft skin layers enable texturing of two-dimensional electronic materials with programmable feature sizes and structural hierarchy because of the conformal adhesion to the substrates. Soft skin systems open prospects to tailor a range of surface properties *via* external stimuli important for applications such as smart windows, microfluidics, and nanoelectronics.

Related publication:

1.1. Introduction to Conventional Stimuli-Responsive Patterns

Reconfigurable surface patterns are topographical features that can change dimension and orientation in response to external stimuli.[1-3] These structures support physical and chemical properties that can be reversibly tuned, which are beneficial for applications in smart windows, sensors, and actuators.[4-6] Most work on creating responsive systems has focused on combining three-dimensional (3D) structures with deformable soft materials.[7,8] For example, arrays of silicon nano- or microstructures integrated with hydrogels can change their orientation depending on the swelling state of the gel (**Figure 1.1**).[1] To realize this system, 3D silicon structures such as pillars and fins are first fabricated using the Bosch deep reactive ion etching process (**Figure 1.1a**). The lateral dimensions and height can be designed to achieve a target range of tilting during actuation of the patterns. The hydrogel component is then created by forming an anchoring layer on the surface and grafting gel by photo- or thermo-initiated radical polymerization of monomers and
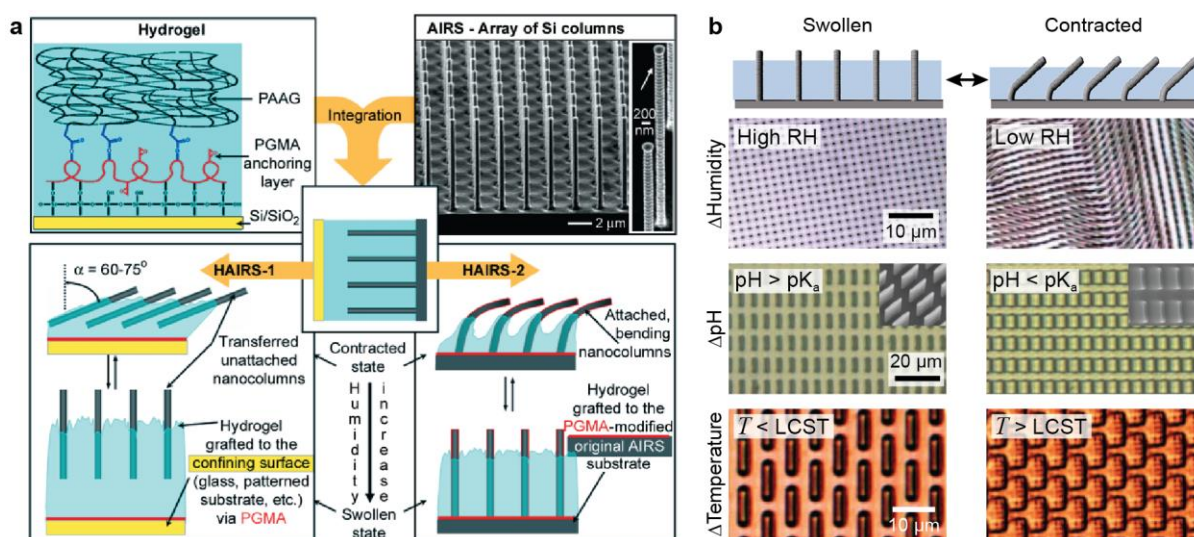
Figure 1.1. Conventional stimuli-responsive patterns consisting of silicon pillar arrays and hydrogels. (a) Scheme describing the fabrication process. **(b)** Operation of the patterns under different environmental stimuli. Panel a adapted with permission from ref 1. Panel b adapted with permission from refs 1, 3, 5, and 6.

cross-linking agents with the presence of a confining substrate over the patterned silicon. By selecting the surface to form the anchoring layer, the arrays can either be transferred to a secondary substrate and become free-standing (HAIRS-1 in Figure 1.1a; anchoring layer on the confining surface) or remain fixed on the original wafer (HAIRS-2 in Figure 1.1a; anchoring layer on the silicon surface). The 3D silicon arrays assume a tilted orientation when they are bent by tensile forces that result from shrinking of the gel and return to the vertical orientation when the tension is released upon re-swelling of the gel (**Figure 1.1b**). Depending on functional moieties within the hydrogel, the 3D structure/hydrogel hybrid system respond to different types of external stimuli such as changes in humidity, pH, and temperature.[1,5,6] Alternatively, reconfigurable features can also be produced by replicating surface topography of a patterned master on a deformable polymer substrate *via* molding, where spacing between the resulting features can be modified by external strain or other stimuli.[9]

The functional response of surface patterns can be engineered through their length scales; microscale features are typically used to tune surface adhesion, optical transparency, and antibiofouling properties,[10,11] while nanotextures are advantageous to tailor hydrophobicity/hydrophilicity and structural color (**Figure 1.2**).[12,13] For example, arrays of gold-coated epoxy microfins partially embedded into hydrogels can switch between upright (transparent) and tilted (opaque) states when the matrix swells or contracts under environmental changes (**Figure 1.2a**).[4] Also, elastomer nanopillar arrays can transition from a closer spaced (blue diffractive color) to a wider spaced configuration (red diffractive color) under tensile strain applied to the substrate (**Figure 1.2b**).[9] One drawback of conventional reconfigurable patterns is that they require complex lithographic processes with multiple steps of masking and etching to control the periodicity and orientation of nano- and micrometer-sized patterns for targeted properties.
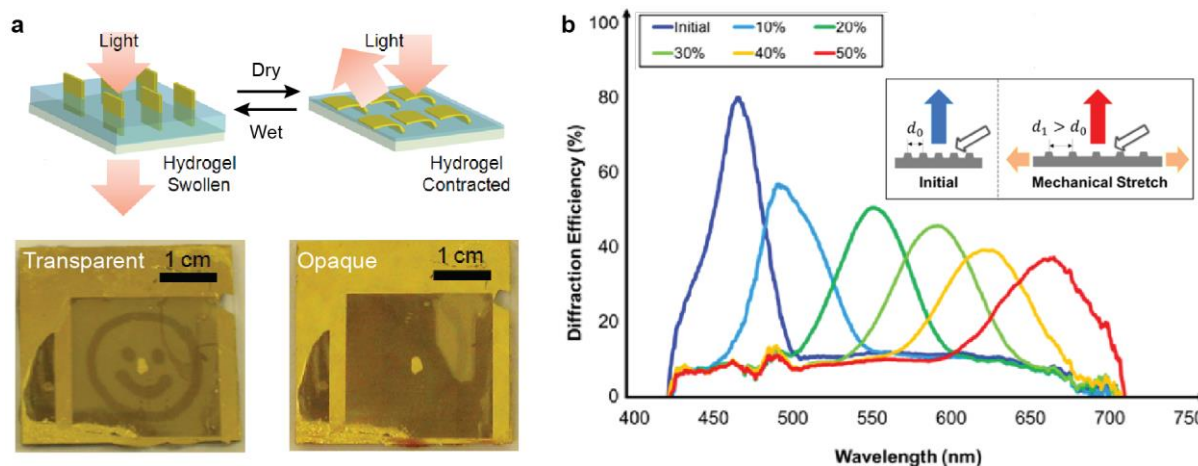
Figure 1.2. Reconfigurable patterns with reversibly tunable functional responses. (a) Gold-coated epoxy microfin arrays with switchable optical transparency. **(b)** Elastomeric pillar arrays with tunable structural colors. Panel a adapted with permission from ref 4. Panel b adapted with permission from ref 9.

1.2. **Background of Surface Textures Based on Wrinkling**

1.2.1. *Buckling Instabilities from Compression of Skin Layer/Substrate Systems*

Mechanical instabilities that result from the compression of a thin material—often referred to as a skin layer—on a pre-strained polymer substrate have emerged as an approach to create surface textures spontaneously over multiple length scales without using lithography.[14] Various types of patterns can form depending on the Young's moduli of the skin layer (E_S) and substrate (E_B), the skin thickness (h), the adhesion energy (Γ, work required to detach the skin layer from a unit area of the substrate), and the amount of compressive strain (ε) that results from releasing the pre-strain (ε_{pre}). When the adhesion energy is low compared to the skin thickness and the modulus of the substrate ($\Gamma/hE_B < 1$), the skin layer partially detaches from the substrate to form delaminated buckles (**Figure 1.3a**). If the adhesion energy is high enough to prevent delamination, other types of surface patterns can develop. For a bilayer system with a skin layer exhibiting a modulus close
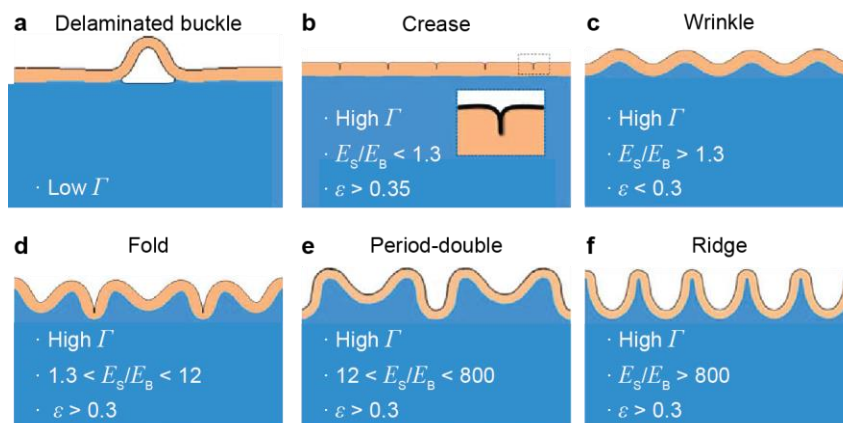
Figure 1.3. Types of surface instabilities that can result from compressing a skin layer on a polymer substrate. (a) Delaminated buckles, **(b)** creases, **(c)** wrinkles, **(d)** folds, **(e)** period-doubles, and **(f)** ridges. Adapted with permission from ref 14.

to that of the substrate or smaller ($E_S/E_B < 1.3$), creases are formed, where the skin layer locally folds and make self-contacts with sharp tips without deforming the substrate out-of-plane (**Figure 1.3b**). The transition from flat to crease state occurs when the compressive strain is higher than a threshold ($\varepsilon > 0.35$). When the skin layer is stiffer than the substrate ($E_S/E_B > 1.3$), the skin layer bends out-of-plane into a sinusoidal geometry upon strain relief to produce wrinkles while deforming the substrate near the interface (**Figure 1.3c**). For high strains ($\varepsilon > 0.3$), wrinkles transform into various secondary structures, such as folds—the skin layer make self-contacts within some valleys of wrinkles ($1.3 < E_S/E_B < 12$), period-doubles—the system exhibit patterns with a periodicity twice the wrinkle wavelength ($12 < E_S/E_B < 800$), and ridges—some wrinkles grow in amplitude while the others become flat ($E_S/E_B > 800$) (**Figure 1.3d-f**). Among different types of strain-induced textures, wrinkles have been widely investigated as a promising method for surface patterning because feature dimensions and orientations can be precisely tuned compared to other patterns.[15,16]

1.2.2. Design Principles of Wrinkle Patterns

Wrinkles are commonly produced by mechanically stretching an elastomer substrate to apply pre-strain, forming a skin layer, and then releasing the pre-strain (**Figure 1.4a**).[17-19] Wrinkle wavelength (λ, peak-to-peak distance) and amplitude (A, vertical displacement between peaks and valleys) can be designed based on the materials properties of the system and applied strain. At low strain ($\varepsilon_{pre} < 10\%$), the wrinkle amplitude increases with ε_{pre} while the wavelength remains the same (linear model):[20,21]

$$\lambda_{linear} = 2\pi h (\bar{E}_S / 3\bar{E}_B)^{1/3} \tag{1.1}$$

$$A_{linear} = 2h\sqrt{\varepsilon_{pre}/\varepsilon_c - 1} \tag{1.2}$$

where $\bar{E} = E/(1 - v^2)$ is the plane-strain modulus, v is the Poisson's ratio, ε_c is the critical pre-strain to generate wrinkles. At higher strain ($\varepsilon_{pre} > 10\%$), λ decreases with the pre-strain and A increases with a more complicated dependence on the strain (nonlinear model):

$$\lambda_{nonlinear} = \frac{\lambda_{linear}}{(1+\varepsilon_{pre})(1+\xi)^{1/3}} \tag{1.3}$$

$$A_{nonlinear} = \frac{A_{linear}}{\sqrt{1+\varepsilon_{pre}}(1+\xi)^{1/3}} \tag{1.4}$$

where $\xi = 5\varepsilon_{pre}(1 + \varepsilon_{pre})/32$. Besides the length scale, wrinkle orientation can be controlled based on the direction of strain;[22] uniaxial strain relief results in highly aligned one-dimensional (1D) wrinkles in a single direction, while biaxial strain relief produces two-dimensional (2D) wrinkles with quasi-random orientations (**Figure 1.4b**).

After the wrinkle formation, the patterns can be further changed by mechanically strain. For example, when the uniaxially-aligned wrinkles are stretched perpendicular to their orientation, the
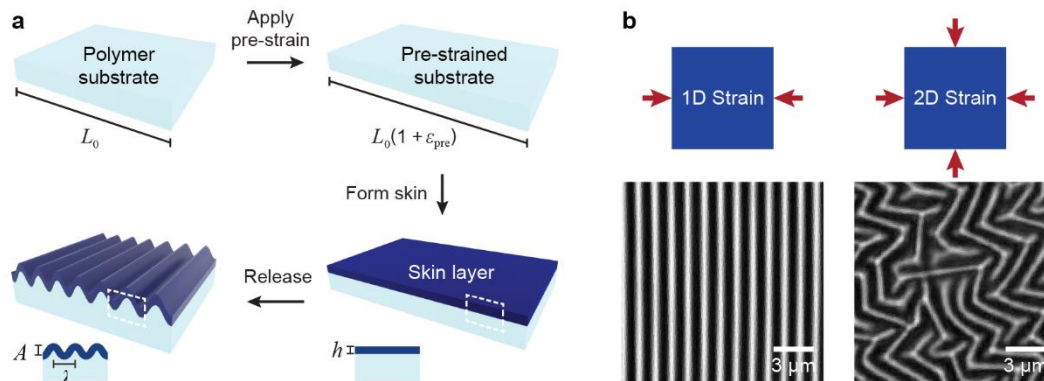
Figure 1.4. Wrinkle patterns with tunable feature sizes and orientations. (a) Schematic illustration of wrinkle fabrication. **(b)** Wrinkles formed with different strain relief directions. Panel b adapted with permission from ref 22.

textures respond to the applied tensile strain (ε) by increasing λ and decreasing A until the surface becomes flat at $\varepsilon = \varepsilon_{pre}$. Further stretching ($\varepsilon > \varepsilon_{pre}$) creates wrinkles oriented perpendicular to the as-fabricated wrinkles.[23] The wrinkles with the switched orientation decrease in the wavelength and increase in the amplitude with increasing strain. Upon release of the substrate, the system can recover wrinkles with the initial orientation. Because the wrinkle wavelength, amplitude, and orientation can be tuned in response to the substrate strain, reversible modification of properties such as optical transmittance and surface adhesion is possible by applying external stimuli.[23,24]

1.3. Skin/Substrate Systems for Reconfigurable Wrinkles

1.3.1. Conventional Systems Based on Hard Skin Layers

Conventional stimuli-responsive wrinkles are based on a bilayer architecture of elastomer substrates coated with skin layers of a thin metal film (**Figure 1.5a**).[25-27] A range of metals such as gold, silver, chromium, aluminum, and nickel can be deposited on pre-strained polydimethylsiloxane (PDMS) sheet using physical vapor deposition techniques, which form
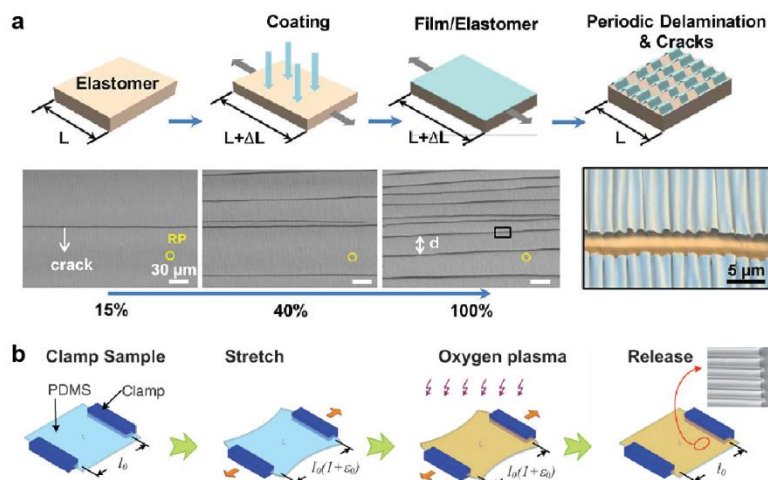
Figure 1.5. Conventional wrinkle systems based on hard skin layers on elastomer substrates. Wrinkle fabrication with (**a**) thin metal films and (**b**) silica layers. Panel a adapted with permission from ref 26. Panel b adapted with permission from ref 24.

wrinkles upon strain relief.[25-29] Another method commonly used to form a skin layer is to treat the PDMS substrate with an oxygen plasma (**Figure 1.5b**).[19,24,30] This plasma process convert the top surface of PDMS into silica, which is stiffer than the bulk PDMS. Wrinkles based on metal or silica films, however, have been limited as a general strategy for realizing reconfigurable surface patterns because cracks form at random locations in the skin layers under tensile strain exceeding 10%.[25,31] Although cracks can be useful for preparing functional surfaces that are sensitive to applied strain,[32-34] they hinder tuning of directional properties such as anisotropic water spreading and light diffraction.[23,35] Mechanical instabilities can also result in delamination of the skin layer when the wrinkle topography is changed under substrate stretching.[23,25] Although the wrinkle wavelength in these bilayer systems can be controlled at the microscale, nanowrinkles are difficult to achieve because the Young's modulus of the skin (typically 40-280 GPa)[19,25-27] is much larger than the substrate (0.5-4 MPa).[36]

1.3.2. *Solution-Processed Polymer Skin Layers for Crack-Free Wrinkles*

In general, a skin/substrate bilayer system can accommodate more tensile strain without crack formation when the modulus ratio E_S/E_B is small.[37] Polymer skin layers with Young's moduli ranging from hundreds of MPa to several GPa ($E_S/E_B < 5000$)[38-41] are advantageous for fabricating crack-free wrinkles compared with metal or silica (E_S/E_B ranging from 2.4×10^4 to 1.8×10^5).[19,25-27] The most common method to produce soft skin layers is by drop casting polymer solutions such as poly(vinyl alcohol) (PVA).[38,42] Depositing PVA on a pre-strained PDMS slab followed by solvent evaporation results in films with an average thickness of a few micrometers.[38,42] Upon strain relief, the PVA/PDMS system ($E_S/E_B \approx 1900$) forms wrinkles ($\lambda \approx 40\text{-}110$ µm; $h \approx 4\text{-}7$ µm) that can be repeatedly switched between wrinkled and flat states up to high strain ($\varepsilon_{pre} = 90\%$).[42] This approach, however, cannot achieve uniform λ over centimeter-scale areas since the thickness of the skin layer is uneven because of coffee-ring features and aggregation after drying.[43] The fabrication of wrinkles with sub-micrometer wavelengths is also difficult because the films tend to be thicker than one micron.[38,42,44] Meniscus-guided coating techniques such as solution shearing and dip coating can also create polymer skin layers with controlled thickness;[45,46] however, these strategies often result in discontinuous films for thicknesses < 100 nm because the solution meniscus pins and de-pins during the coating process.[47]

In contrast, spin coating can produce continuous skin layers with a uniform thickness ranging from tens to hundreds of nanometers (**Figure 1.6**).[39,40,48-50] This technique has been used to process a range of polymers on pre-strained elastomer substrates and to generate wrinkles for stretchable electronics (**Figure 1.6a**). For example, a composite organic semiconductor spin-cast on a pre-strained ($\varepsilon_{pre} = 20\%$) PDMS substrate ($E_S/E_B \approx 800\text{-}4100$) formed microscale wrinkles ($\lambda \approx 10$
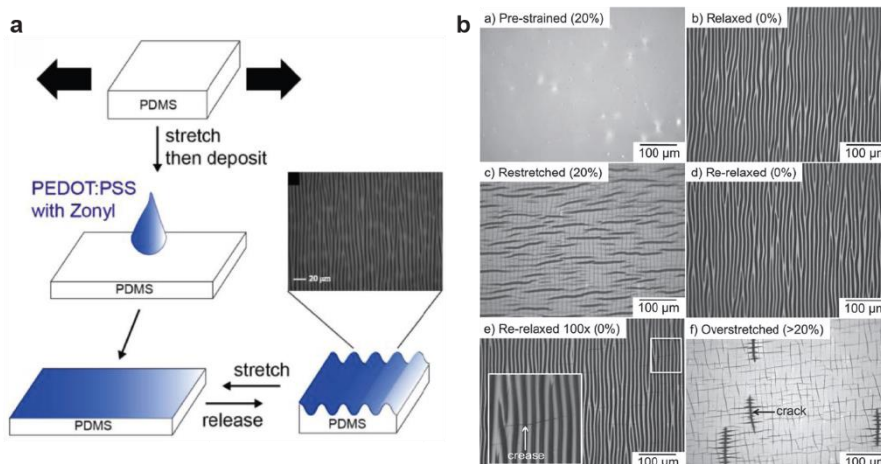
Figure 1.6. Mechano-responsive patterns from wrinkling solution-processed polymer skin layers. (a) Fabrication of polymer wrinkles based on spin-coating. **(b)** Structural evolution of wrinkled organic semiconductor film at different strains. Panel a adapted with permission from ref 40. Panel b adapted with permission from ref 39.

µm) upon strain relief that could be stretched without cracking up to the pre-strain amount (**Figure 1.6b**).[39] As a result, the photovoltaic properties of the wrinkled composite were nearly identical after stretch-release cycles. Although spin coating can control the length scale of features by varying *h*, this method is limited because (1) defects such as voids and striation patterns result in skin layers that are not uniform in thickness, especially for *h* < 20 nm, and thus controlling topography for sub-200 nm wrinkles is difficult;[48,51] and (2) oxygen plasma treatment used to improve wetting of the precursor solution can form brittle silica films that result in cracking in the skin layer when the substrate is stretched more than 10%.[52]

1.3.3. Conformal Polymer Skin Layers from Chemical Vapor Deposition

Chemical vapor deposition (CVD) can also form soft skin layers of organic semiconductors as well as fluoropolymers conformally coated on pre-strained substrates.[53,54] CVD polymers are commonly synthesized based on two mechanisms: (1) free radical chain growth or (2) oxidative

step growth (**Figure 1.7a-b**).[53,54] For the former case, vapor-phase monomers and initiator molecules are delivered to the substrate (**Figure 1.7a**). When the initiators are activated by an energy source such as heat, light, or plasma, radicals are generated and react with monomer to create one-mer with an active center. Polymer chains grow when other monomers bond to this active center, which transfers to the chain end for each addition of monomer until the growth terminates. In the latter oxidative step growth strategy, monomers are oxidized into positively charged radicals with the presence of oxidizing agents (**Figure 1.7b**). These radicals then react with each other to form dimers, followed by production of progressively longer chains through repeated oxidation and reaction with other monomeric or oligomeric species. Because CVD process does not rely on solution processing, ultra-thin (< 10 nm) skin layers can be created without needing the surface to be hydrophilic, which is typically realized by applying an oxygen plasma.[53-]
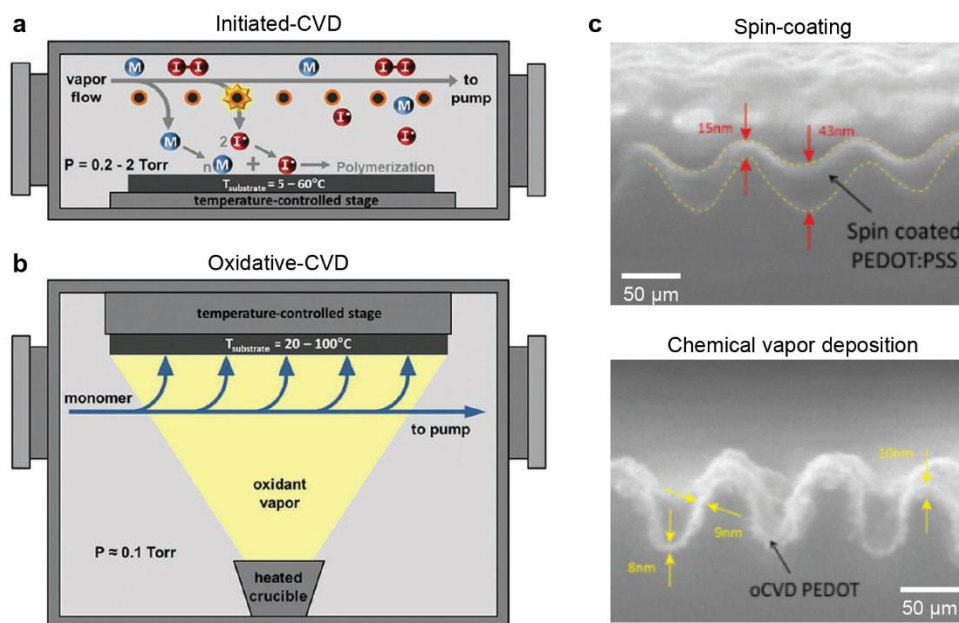
Figure 1.7. Chemical vapor deposition enables conformal coating of polymer skin layers. **(a)** Initiated CVD (free radical chain growth) and **(b)** oxidative-CVD (oxidative step growth) processes. **(c)** Conformality of CVD skin layers compared to spin-coated films. Panels a and b adapted with permission from ref 54. Panel c adapted with permission from ref 56.

[55] Moreover, CVD produces skin layers conformal to complex 3D topography, which is not possible with spin coating that results in thicker films at the bottom of surface patterns than the top (**Figure 1.7c**).[56]

1.4. **Objective and Outline of Thesis**

This thesis aims to develop reconfigurable, multiscale wrinkles based on soft skin layers. In particular, we establish a plasma-mediated deposition process that form thin films of mechanically robust fluoropolymers (CF_x) with nanometer scale control over thickness. **Chapter 2** describes a crack-free, responsive wrinkles enabled by the soft CF_x skin layer on pre-strained PDMS substrates. Side-by-side comparisons between this bilayer composite and conventional silica-coated PDMS are provided to highlight the durability of the soft skin during repeated wrinkle orientation switching by strain. **Chapter 3** depicts a strategy to introduce multiscale textures into two-dimensional (2D) materials by conformal wrinkling of 2D materials on PDMS substrates patterned with different spatial CF_x thicknesses. Using graphene as a representative 2D material, we show that the CF_x layer mediates structural transformation of wrinkles without crack formation or delamination. Generality of our method for structuring other 2D materials such as monolayer molybdenum disulfide is also presented. **Chapter 4** focuses on patterning various 2D materials with in-plane and out-of-plane hierarchical wrinkles based on soluble, sacrificial polymer skin layers. Structural hierarchy and feature sizes can be controlled at multiple length scales by controlling the sacrificial skin thickness both in global and local areas of the substrate. Lastly, **Chapter 5** reports functional surfaces enabled by hierarchical wrinkles with a rational design of characteristic feature sizes and orientations. We also demonstrate the feasibility of transferring the

patterns into other functional materials to engineer the properties.

Chapter 2

Crack-Free Wrinkles with Switchable Anisotropic Wetting

This chapter describes how soft skin layers on elastomeric substrates support mechano-responsive wrinkle patterns that do not exhibit cracking under applied strain. Soft fluoropolymer skin layers on pre-strained polydimethylsiloxane slabs achieved crack-free surface wrinkling at high strain regimes not possible by conventional stiff skin layers. A side-by-side comparison between the soft and hard skin layers after multiple cycles of stretching and releasing revealed that the soft skin layer enabled dynamic control over wrinkle topography without cracks or delamination. We systematically characterized the evolution of wrinkle wavelength, amplitude, and orientation as a function of tensile strain to resolve the crack-free structural transformation. We demonstrated that wrinkled surfaces can guide water spreading along wrinkle orientation, and hence switchable, anisotropic wetting was realized.

2.1. **Introduction**

Wrinkling of stiff skin layers on elastomer substrates have been used as a simple method to create surface patterns that are responsive to mechanical stimuli.[18-20,23,57] Because periodicity, amplitude, and orientation of the resulting wrinkles can change under stretching or bending, dynamic and reversible tuning of functional responses such as optical transmittance, wettability, and surface adhesion is possible.[18,23,58,59] One drawback of conventional systems based on metal or silica films, however, is that the skin layers crack when the applied tensile strain exceeds 10%.[18,25,31,60-62] Because locations of cracks cannot be controlled precisely, designing functionalities that require controlled structural features, such as for anisotropic wetting and light diffraction, has been challenging.[23,35,63,64] Furthermore, cracks limit the long-term stability of the patterns by causing delamination of the skin layer from the substrate under repeated mechanical deformations.[23,25]

Crack formation in wrinkled substrates can be suppressed by using soft polymer skin layers.[38,39,42,48,65] Most efforts have been based on polymer thin films created by solution processing techniques that can generate crack-free wrinkles with wavelengths ranging from hundreds of nanometers to tens of micrometers.[38,39,42,48] Systematic design of nanoscale features using solution-based methods, however, is challenging because of limited control over the skin thickness. Recently, chemical vapor deposition has been investigated to produce polymer skin layers with nm-scale tunable thickness, which allows the wrinkle wavelength to be tailored from several micrometers down to tens of nanometers.[55,65] Introducing skin layers of mechanically robust materials such as fluoropolymers would enable access to high strain regimes ($\varepsilon > 0.6$) without crack formation and delamination,[66-69] which is beneficial for increasing tunability in

wrinkle topography by substrate stretching.

In this chapter, we report a crack-free bilayer system that can achieve both nano- and microscale wrinkles with dynamically tunable surface topography under mechanical strain. A soft, fluoropolymer (CF_x) skin layer deposited on PDMS *via* a CHF_3-plasma treatment was compared side-by-side to a hard, silica-like (SiO_x) skin to confirm the advantages of soft skin materials. Soft skins achieved more than a 10-fold increase in the amount of pre-strain that could be relieved without cracking compared to hard skins, which offers a wider range of tunability over wrinkle wavelength and amplitude in a crack-free regime. Furthermore, the orientation of wrinkles could be modulated under cycles of stretching and releasing without cracks or delamination. We revealed the mechanism of the orientation switching by investigating changes of characteristic wrinkle features in the soft skin layer under increased strain. Taking advantage of soft-skin-based wrinkles, we demonstrated switching of anisotropic water spreading that has not been possible with the traditional wrinkling systems.

2.2. **Process for Creating Soft Skin Wrinkles on Elastomer Substrates**

Figure 2.1 depicts the method to produce wrinkles in soft and hard skin layers (CF_x and SiO_x, respectively) on PDMS substrates using two types of reactive ion etching (RIE) plasma treatments. Note that we designate the CF_x skin layer as "soft" because the Young's modulus is 40 times less than that of the "hard" silica skin layer. First, a PDMS substrate was clamped in a custom-designed stretching apparatus and uniaxially stretched to apply a pre-strain, $\varepsilon_{pre} = (L - L_0)/L_0$, where L_0 and L are lengths before and after stretching (**Figure 2.1a**). CHF_3 plasma created the soft skin layer[65,70] on the pre-strained substrate with a thickness (h) (**Figure 2.1b**). Releasing ε_{pre} after plasma
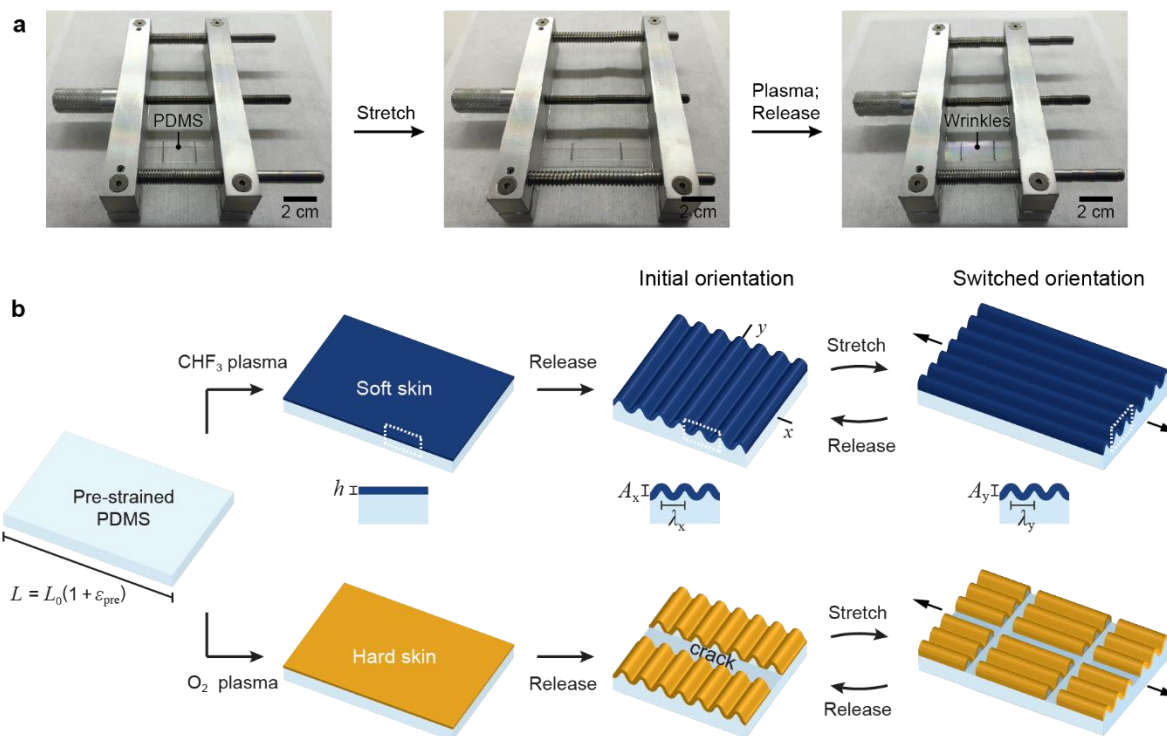
Figure 2.1. Soft fluoropolymer skin layer for crack-free wrinkling. (a) Optical images of PDMS substrates mounted in a stretching apparatus for wrinkle fabrication. **(b)** Scheme describing the overall process. CHF_3 plasma treatment created a soft fluoropolymer on a pre-strained PDMS, which formed wrinkles upon strain relief. The soft skin layer was directly compared to the hard silica-like skin formed from O_2 plasma under stretching and releasing of the substrate.

treatment created ordered, one-dimensional (1D) wrinkles with the wavelength (λ) and amplitude (A) proportional to h.[20,23] For comparison, we also formed wrinkles in hard skin layers from O_2 plasma treatment of PDMS. The directions parallel and perpendicular to the pre-strain direction are denoted as x and y, respectively, to describe surface topography.

2.3. **Mechanism for Plasma-Mediated Skin Layer Formation**

2.3.1. *Soft Fluoropolymer Skin Layer from CHF_3 Plasma Treatment*

To reveal the mechanism how the soft, fluoropolymer skin layer forms on PDMS substrates,

we analyzed samples as a function of CHF_3 plasma time (t) using x-ray photoelectron spectroscopy (XPS) and variable-angle spectroscopic ellipsometry. The plasma process generates fluorine-containing species (e.g. CHF_2^+ and CF_3^+) that bombard the surface of PDMS.[71,72] By analyzing the XPS C1s, Si 2p, and F 1s spectra as a function of t, we quantified the ratio of atoms and chemical bonding at different stages of skin layer formation. During a short treatment ($t = 5$ s), F content significantly increased (from 0 at% to ~50 at%) while Si decreased in content (**Table 2.1**). C and F contents became unchanged (~ 43 at% C and ~57 at% F) whereas Si was not detected after $t = 40$ s, which suggested that the fluoropolymer was deposited on the PDMS surface.

The C 1s spectra could be deconvoluted into five peaks identified by the number of F atoms bonded to the C atom: not bonded (**C**-Si, 284.3 eV), indirectly bonded (**C**-CF_x, 286.5 eV), one (**CF**, 288.9 eV), two (**CF**$_2$, 291.2 eV), and three (**CF**$_3$, 293.4 eV), respectively (**Figure 2.2**).[71-75] As the fluorine-containing species bonded to the PDMS, the **C**-Si component (corresponding to PDMS) decreased in the ratio during early stages while ratios of other components increased. After 40 s exposure, the **C**-Si were not detected and contents of other bonding became constant. The time evolution of the chemical bonding confirmed that the soft fluoropolymer skin layer had a uniform chemical composition except near the interface between the skin and PDMS.

Table 2.1. Elemental compositions of PDMS samples under different CHF$_3$ RIE times.

RIE time (s)	C (at%)	F (at%)	Si (at%)
0	64.2	0.0	35.8
5	40.1	49.5	10.4
20	42.9	55.9	1.1
40	43.5	56.5	0.0
60	43.6	56.4	0.0
240	43.1	56.9	0.0
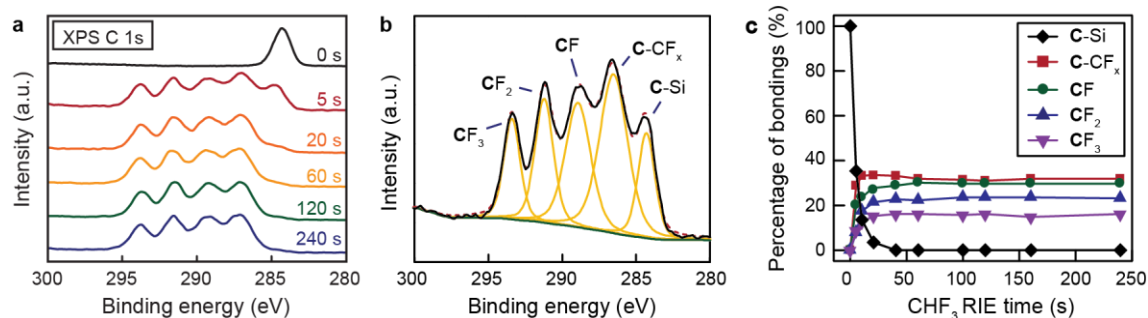
Figure 2.2. Chemical bonding in the soft skin revealed by XPS. (a) XPS C 1s spectra of PDMS samples treated with different CHF$_3$ RIE times. **(b)** Deconvolution of the spectra into peaks corresponding to different bonding components. **(c)** Ratio of chemical bonding as a function of treatment time.

The thicknesses of the soft skin layer (h_{soft}) were determined by fitting the measured ellipsometry constants (Ψ and Δ) to a bilayer (skin/PDMS) model (**Figure 2.3a**). A Cauchy equation ($n = A + B/\lambda^2 + C/\lambda^4$) was used to relate Ψ and Δ to the optical properties of the skin and substrate.[76] We first obtained the Cauchy parameters of the substrate ($A = 1.402$, $B = 3.7\text{x}10^{-3}$ µm^2, and $C = 6.9\text{x}10^{-5}$ µm^4) from the ellipsometry measurements on untreated PDMS, and then used these values to model CHF$_3$-treated samples. Because the Cauchy parameters did not change significantly with RIE time, those from the sample with the thickest skin layer ($t = 600$ s: $A = 1.37$, $B = 6.4\text{x}10^{-3}$ µm^2, and $C = -8.0\text{x}10^{-5}$ µm^4) were used to calculate h_{soft} of all the samples to increase
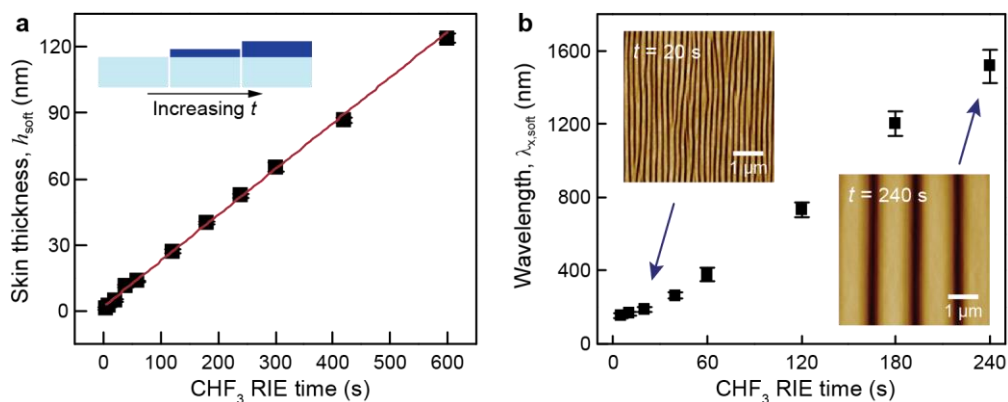
Figure 2.3. Soft skin system showed tunable skin thickness and wrinkle wavelength. (a) Soft skin thickness and **(b)** Wrinkle wavelength as a function of CHF$_3$ RIE time.

the accuracy of the measurement. We found that h_{soft} can be controlled from sub-10 nm to hundreds of nm with nanometer precision with a linear dependence on the CHF$_3$ plasma time (0.21 nm/s, R^2 = 0.995), which allows the wrinkle wavelength to be tailored from several micrometers down to sub-200 nm (**Figure 2.3b**).

2.3.2. Silica Skin Layer from Oxygen Plasma Treatment

We examined the surface oxidation process of PDMS resulting from O$_2$ plasma treatment using XPS C1s, Si 2p, and O 1s spectra with varying RIE times (t). During the O$_2$ RIE, the O increased in content at the expense of C, while Si content remained similar (~28.5 at%) (**Table 2.2**). The change in elemental composition verifies that O$_2$ RIE converted methyl groups bonded to silicon atoms into oxygen atoms near the surface of PDMS and created the hard silica-like skin layer.

Chemical structure of the skin layer was revealed by deconvoluting the Si 2p spectra (**Figure 2.4**) into three components based on the oxidation states of the silicon atoms in each siloxy unit: Si bonded two (D, -**Si**(CH$_3$)$_2$O-, 101.9 eV, PDMS), three (T, -**Si**(CH$_3$,O)O-, 102.9 eV), or four (Q, -**Si**O$_2$-, 103.7 eV, silicon dioxide) oxygen atoms, respectively.[77-80] As t increased, the percentages of T and Q components increased while D decreased. For longer treatment (t > 20 s), the ratio of

Table 2.2. Elemental compositions of PDMS samples under different O$_2$ RIE times.

RIE time (s)	C (at%)	Si (at%)	O (at%)
0	50.4	28.1	21.5
5	25.4	27.5	47.2
60	12.7	28.9	58.3
240	9.4	30.7	59.9
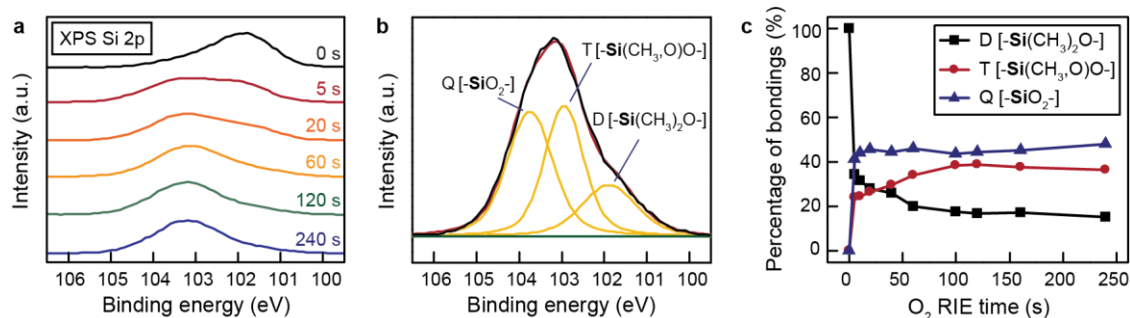
Figure 2.4. Chemical structure of the hard SiO$_x$ skin revealed by XPS. (a) XPS Si 2p spectra of PDMS samples treated with different O$_2$ RIE times. **(b)** Example peak deconvolution. **(c)** Percentage of bonding components as a function of time.

the Q remained nearly constant at 45% and that of T increased at the expense of the D. The percentages of the three components became unchanged (17% D, 38% T, and 45% Q) for t longer than 100 s. The time evolution of chemical bonding indicated that the O$_2$ plasma gradually converts PDMS into the SiO$_x$ skin layer from the surface with the maximum conversion of D:T:Q = 17:38:45.[81]

Because the interface between the hard skin layer and PDMS substrate was not sharp, measuring the skin thickness (h_{hard}) using ellipsometry was not possible. One alternate method to characterize h_{hard} was to examine the electron density (ρ_e) using the x-ray reflectivity (XRR).[81] First, we plotted XRR of O$_2$-RIE-treated PDMS samples with respect to the scattering vector (Q =
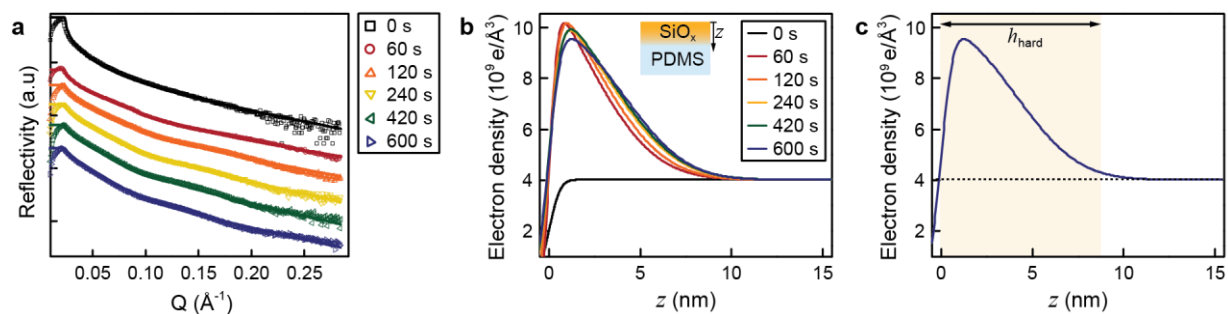
Figure 2.5. Characterization of thickness of hard skin layer using x-ray reflectivity. (a) Reflectivities of the PDMS treated with different times of O$_2$ plasma. **(b)** Calculated electron densities. **(c)** An example skin thickness characterization.

$4\pi/\lambda \sin\theta$) (**Figure 2.5a**). Then, the data were fitted to a bilayer model (skin/PDMS) using a software (Motofit) to obtain electron density profiles as a function of depth (z) below the surface.[82] ρ_e of PDMS was determined from XRR of an untreated sample and kept constant for subsequent analyses. **Figure 2.5b** shows the resulting electron density profiles of the samples treated with different times of O_2 plasma. Because the number of oxygen atoms bonded to the silicon atoms increased due to the plasma oxidation, ρ_e near the surface increased, which gradually decreased to that of the bulk PDMS with increasing z (Figure 2.5b). h_{hard} can be defined as the depth range in which the electron density is 5% above the PDMS baseline (**Figure 2.5c**):[81]

$$\rho_e > \rho_e\,(\text{PDMS}) + 0.05[\rho_e\,(\text{maximum}) - \rho_e\,(\text{PDMS})] \tag{2.1}$$

Estimated h_{hard} showed a logarithmic dependence on t and became nearly constant after 600 s of treatment (~ 9 nm) (**Figure 2.6**).
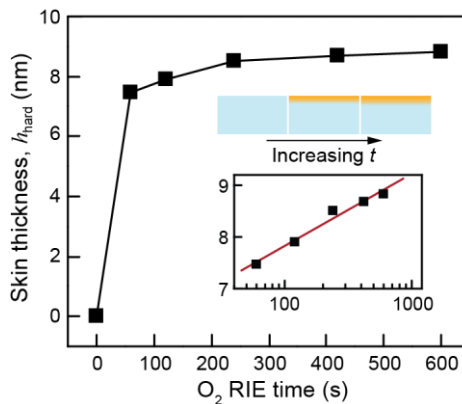
Figure 2.6. Hard skin layer thickness showed a logarithmic dependence on O_2 RIE time. Inset shows the log-scale plot.

2.4. **Mechanical Properties of Skin Layers**

We determined the Young's moduli of skin layers (E_S) from the wavelength of wrinkles at low strain ($\varepsilon_{pre} = 5\%$). The expression for the wrinkle wavelength in this linear regime (λ_{linear}) (Equation 1.1) can be rearranged for calculating E_S:[83]

$$E_S = 3E_B \frac{1-v_S^2}{1-v_B^2} \left(\frac{\lambda_{linear}}{2\pi h}\right)^3 \tag{2.2}$$

where E_B is Young's modulus of PDMS, v_S and v_B are the Poisson's ratios of the skin and substrate, and h is the skin thickness. **Table 2.3** summarizes the materials properties that were used for obtaining the Young's moduli. E_B was measured from tensile testing in accordance with the American Society for Testing Materials standards (ASTM D412).[84] We assumed that Poisson's ratios of soft and hard skin layers would be similar to those of fluoropolymers (0.5) and silicon dioxide (0.17), respectively.[19,85] From the wrinkles having similar wavelengths (~1 µm), we estimated that Young's moduli of the soft and hard skins were ~1 GPa and ~40 GPa, respectively.

Table 2.3. Calculated Young's moduli of soft and hard skin layers.

	λ (µm)	h (nm)	v_B	v_S	E_B (MPa)	E_S (GPa)
Soft	1.00 ± 0.06	27	0.5	0.5	1.65	1 ± 0.2
Hard	1.00 ± 0.03	8.8		0.17		38 ± 5.5

2.5. **Tunability of Starting Wrinkle Geometries by Pre-Strain**

Because PDMS slabs were compressed perpendicular to the pre-strain direction, releasing the substrate after RIE plasma treatments results in tensile strain (ε_y) in the skin layer. Because the resistance to crack formation is crucial for designing wrinkle topography, we quantified the amount of tensile strain that could be applied without crack formation by investigating wrinkled surfaces formed from different pre-strain values ($\varepsilon_{pre} = 2.5\text{-}50\%$) based on atomic force microscopy (AFM) height images (**Figure 2.7a-b**). We focused on specific thicknesses of soft ($h_{soft} \approx 27$ nm) and hard ($h_{hard} \approx 9$ nm) skins to compare the two materials systems having similar wavelengths. In *Section 2.4*, we found that the soft skin layer was 40 times softer than the hard skin ($E_{soft} \approx 1$ GPa and $E_{hard} \approx 40$ GPa). Because a skin layer/substrate system is typically more resistant to crack formation when the ratio of Young's moduli of the skin and substrate (E_S/E_B) is small,[60,61] we
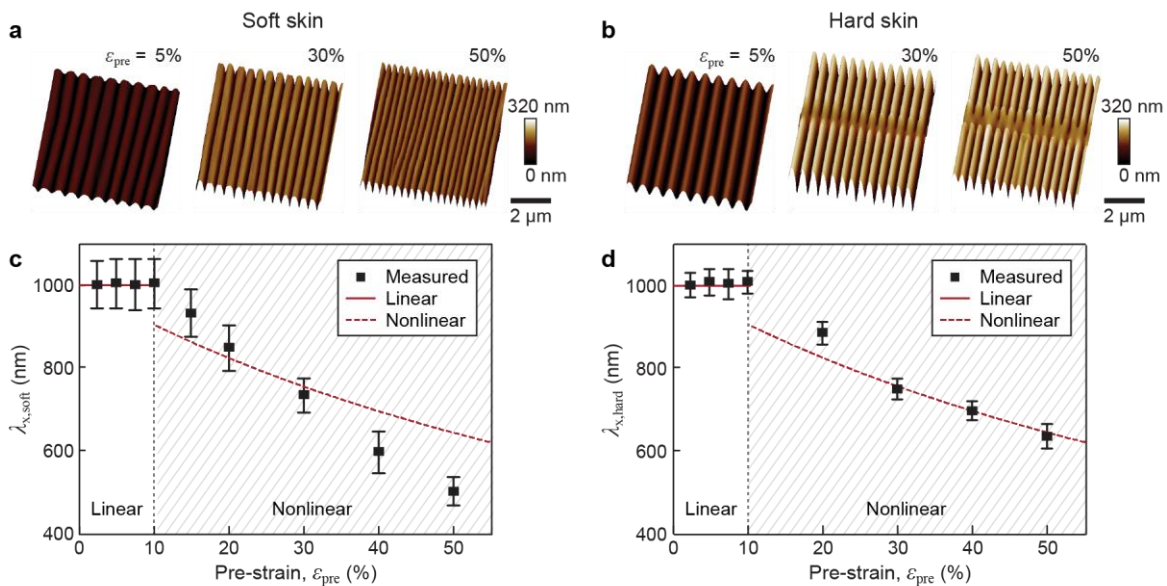
Figure 2.7. Soft skin enabled more tunability of wrinkle features than hard skin in the crack-free pre-strain regime. AFM images of **(a)** soft skin and **(b)** hard skin wrinkles under different ε_{pre}. Hard skin showed cracks when $\varepsilon_{pre} > 5\%$. Wrinkle wavelength as a function of ε_{pre} in the **(c)** soft skin and **(d)** hard skin systems. Lines on the plots are predictions based on the linear and non-linear models.

hypothesized that the soft fluoropolymer skin ($E_{soft}/E_{PDMS} \approx 610$) would accommodate larger strain without cracking compared to the silica ($E_{hard}/E_{PDMS} \approx 2.4 \times 10^4$). As expected, the soft skin did not show cracks for the entire strain range tested ($\varepsilon_y = 1\text{-}25\%$); however, cracks started to form on the hard skin when $\varepsilon_y > 2.5\%$ ($\varepsilon_{pre} > 5\%$). Notably, the width and density of cracks increased with ε_y. Although silica films with Young's moduli comparable to those of polymer skin layers can be prepared by adjusting oxygen-plasma processing conditions,[86] the skin/PDMS composite cannot be stretched >10% without crack formation because silica is brittle.[87] In contrast, The CF_x skin/PDMS system was mechanically robust even up to very high strain regimes ($\varepsilon_{pre} = 100\%$) because the CF_x layer is softer and more ductile than silica.[66] As a result, the soft-skin-based wrinkles can achieve more than a 10-fold increase in uniaxial pre-strain relief without cracking and provides a wider range of tunability over λ and A by changing pre-strain in a crack-free regime.

To investigate how the two systems responded to strain relief, we analyzed the wavelengths and amplitudes of the resulting wrinkles using established linear and nonlinear mechanics models (**Figures 2.7c-d** and **2.8**).[20] In the linear model, λ_x remains constant while A_x increases with pre-strain under increasing ε_{pre} (valid only for low strain, $\varepsilon_{pre} < 10\%$). In the higher strain regime, the non-linear model predicts that λ_x decreases while A_x increases with ε_{pre}. As expected, the wavelength and amplitude of the hard skin layers ($\lambda_{x,hard}$ and $A_{x,hard}$) were in good agreement with these two models under different strain regimes (Figures 2.7d and 2.8). In contrast, the trends observed in the soft skin layer showed deviation from the models. Although the wavelength ($\lambda_{x,soft}$) was in agreement up to $\varepsilon_{pre} = 30\%$, $\lambda_{x,soft}$ at higher pre-strain ($\varepsilon_{pre} > 30\%$) were smaller than expected by 15-20% (Figure 2.7c). Moreover, the amplitude ($A_{x,soft}$) was only 60-70% of that predicted from the two models (Figure 2.8). We attribute this disagreement to wrinkle shape in the soft skin layer, which exhibited peaks flatter than the sinusoidal structure found in conventional
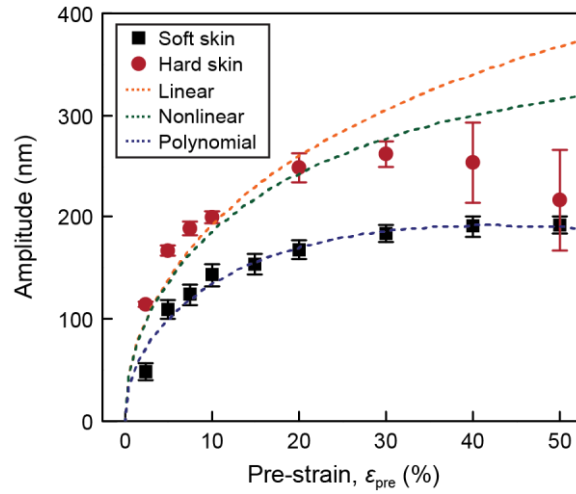
Figure 2.8. Comparison of wrinkle amplitudes with the linear and nonlinear models. Hard skin/PDMS wrinkles were in reasonable agreement, while soft skin/PDMS wrinkles showed smaller amplitudes than expected.

systems. Instead, $A_{x,soft}$ could be described by a polynomial function with fitting parameters (Figure 2.8, polynomial) similar to the observation in the fluoropolymer skin layer on viscoelastic substrates.[88] The soft skin could accommodate larger strain values without forming secondary structures, which leads to a wider tunability over wrinkle topographies.

2.6. **Robustness of Soft Skin Wrinkles under Stretch-Release Cycles**

To highlight the durability of the soft-skin-based system, we compared wrinkle topographies in the soft and hard skin layers under cycles of stretching ($\varepsilon_x = 40\%$) and releasing ($\varepsilon_x = 0\%$) (**Figure 2.9**). First, we fabricated wrinkles under the same pre-strain having similar wavelengths ($\varepsilon_{pre} = 30\%$; $\lambda_{x,soft}$, $\lambda_{x,hard} \approx 740$ nm). When the wrinkles in the soft skin ($\lambda_{x,soft} \approx 740$ nm; $A_{x,soft} \approx 180$ nm) were stretched, the orientation switched perpendicular to its original state with $\lambda_{y,soft} \approx 800$ nm and $A_{y,soft} = 140$ nm (**Figure 2.9a**). Upon release, the wrinkles returned to the initial orientation with the same $\lambda_{x,soft}$; however, the wrinkles showed a decreased $A_{x,soft}$ (~17%) because
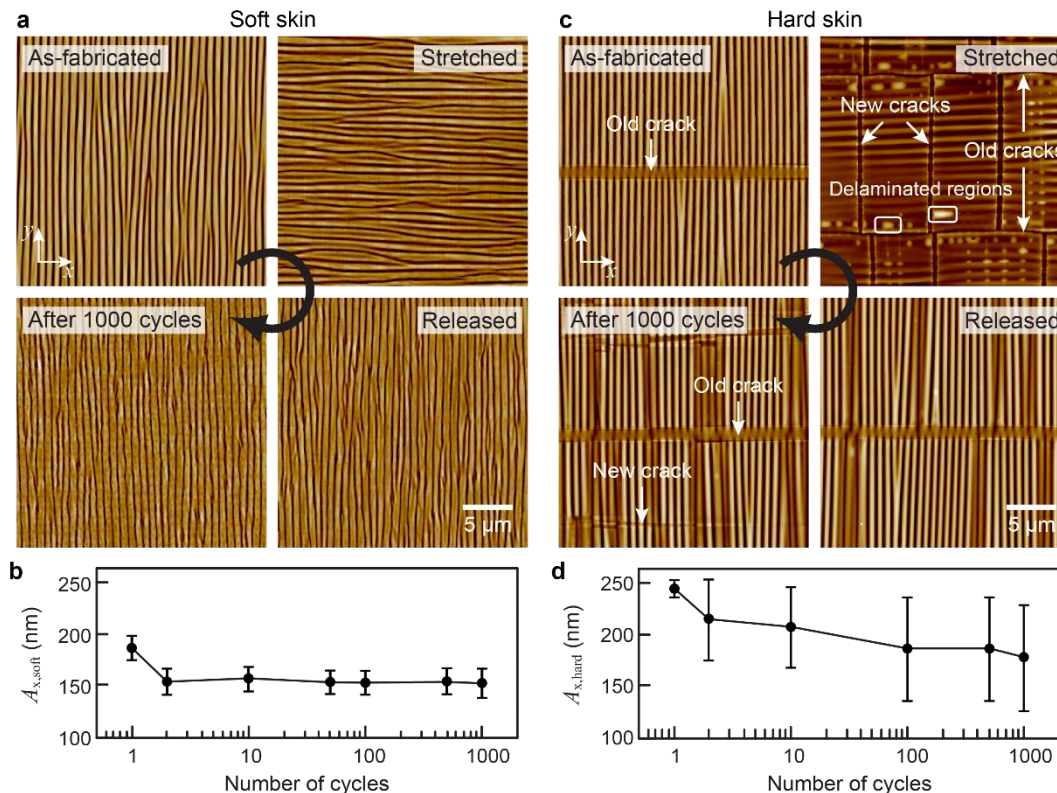
Figure 2.9. Comparison of the durability of the wrinkle patterns during cyclic switching of the wrinkle orientation. (a) Soft skin system was absent of cracks or delamination. **(b)** Amplitude of the soft skin/PDMS wrinkles at the released states was maintained. **(c)** Cracks and delamination were formed in hard skin. **(d)** Wrinkle amplitude in hard skin continually decreased. Images are 25 x 25 μm^2.

of plastic deformation induced during wrinkle orientation switching by stretching (**Figure 2.9b**).

Notably, after the first cycle, the ordering and amplitude of the wrinkles were similar for subsequent stretching-releasing cycles. Significantly, delamination of the skin from the substrate was not observed because the soft skins were conformal on the substrate based on their formation *via* plasma-mediated polymerization.[70]

In contrast, the hard-skin wrinkle system suffered from cracks and delamination during cyclic stretching and releasing (**Figure 2.9c**). Although the orientation could be switched ($\lambda_{y,hard} \approx 1$ μm), the wrinkles were not uniform in amplitude because the existing cracks reduced the compressive

strain applied to the skin layer. Furthermore, additional (new) cracks formed perpendicular to the stretching direction. Notably, we observed blisters on the surface, which suggests that the skin layer delaminated from the substrate in localized regions.[89,90] Upon releasing the substrate, the wrinkles switched back to the original orientation with the same initial wrinkle wavelength, $\lambda_{x,hard}$ ≈ 740 nm, but with decreased amplitude adjacent to the new cracks. As a result, the average $A_{x,hard}$ decreased from 250 nm to 215 nm after the first cycle (**Figure 2.9d**) and continuously reduced down to 175 nm as more cracks formed during repeated switching of wrinkle orientation. The spatial uniformity in wrinkle amplitude also decreased as more cracks form as a function of stretch-release cycle.

2.7. **Mechanism of Crack-Free Wrinkle Orientation Switching**

2.7.1. *Experimental Investigation*

The evolution of surface topologies of the wrinkled soft skin layer ($h_{soft} = 27$ nm, $\varepsilon_{pre} = 30\%$) was examined under tensile strain (ε_x) increasing from 0 to 60% with 5% incremental steps to reveal how the crack-free switching of wrinkle orientation was possible (**Figure 2.10**). Different from systems where the orientation switched abruptly when the amount of applied strain approached the pre-strain value,[18,23] trench-like, intermediate structures were formed perpendicular to the stretching direction starting at low strain (**Figure 2.10a**). These features gradually transformed into the wrinkles with the switched orientation, and the original wrinkles disappeared under increasing stretching.

Quantification of the structural parameters from the AFM images revealed the relation between the wrinkles and the intermediate features (**Figures 2.10b** and **2.11**). When the substrate was
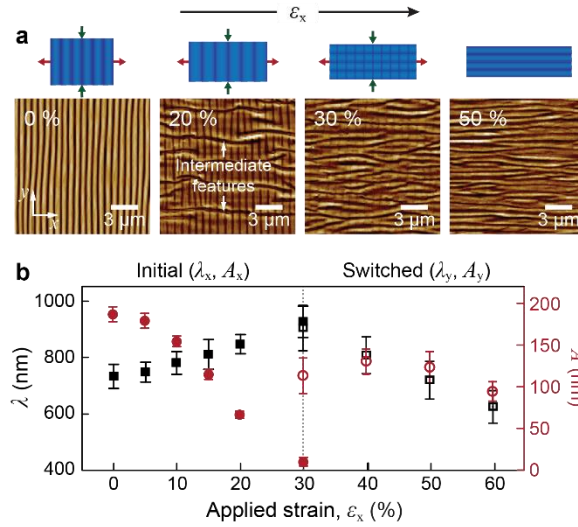
Figure 2.10. Evolution of structural parameters of the **soft skin/PDMS wrinkles during stretching. (a)** AFM images under different ε_x. **(b)** Wavelengths and amplitudes of the wrinkles. Closed and open data points correspond to wrinkles with initial and switched orientations, respectively.

stretched less than the pre-strain amount, wrinkles were flattened to accommodate the tensile strain: $\lambda_{x,soft}$ increased approximately linearly from 740 nm to 930 nm, while $A_{x,soft}$ decreased from 180 nm to 10 nm as ε_x increased from 0 to 30% (Figure 2.10b). At the same time, compressive strain perpendicular to the stretching direction was localized at random locations to form intermediate structures. The average spacing ($<l>$) was 3-6 times larger than the wrinkle wavelength observed when stretching a flat skin layer, which suggests that the wrinkles in the initial orientation served as an effective skin layer and increased the bending stiffness (Figure 2.11).[91,92] The intermediate structures showed a decrease in spacing under increasing ε_x and then gradually transformed to wrinkles. Interestingly, these new wrinkles with switched orientation ($\lambda_{y,soft}$ = 930 nm, $A_{y,soft}$ = 110 nm) coexisted with those with the starting orientation ($\lambda_{x,soft}$ = 900 nm, $A_{x,soft}$ = 10 nm) at ε_x = 30% (Figure 2.10b). The wrinkles completely transitioned to the switched orientation when ε_x > 30%; wavelength and amplitude ($\lambda_{y,soft}$ and $A_{y,soft}$) could be tuned by controlling the amount of ε_x.
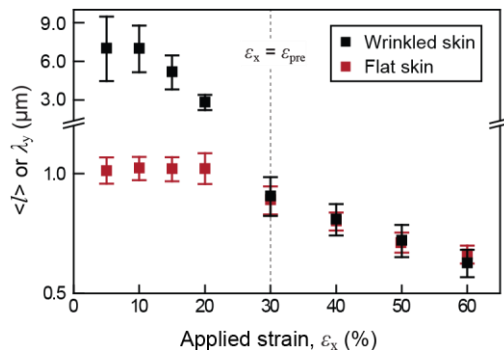
Figure 2.11. Comparison of structural parameters of features formed during stretching wrinkled and flat soft skin layers. Different from wrinkles observed in the flat skin, intermediate structures were generated with larger average spacing when $\varepsilon_x < 30\%$. At higher strain ($\varepsilon_x > 30\%$) the intermediate structures transformed into wrinkles and the wavelength were comparable to those in the flat skin layer.

Although the switched orientation wrinkles were less ordered compared to those formed from a flat skin layer, the wavelength was nearly the same (Figure 2.11), which indicates that the initial wrinkles had a minimal directing effect once the wrinkle orientation completely switched.

2.7.2. *Mechanical Modeling Based on Finite Element Method*

To understand why the wrinkle orientation switched *via* the trench-like intermediate features, we modeled the wrinkling process based on continuum mechanics using the finite element method (FEM). Because the full stress-strain response of the CF_x layer is unknown and bulk fluoropolymers typically undergo plastic deformation at low tensile strain,[67-69] we hypothesized that plasticity of the CF_x layer would important to determine how wrinkle topography changes in response to applied strain. For the CF_x, with the elastic modulus measured from AFM (~1.2 GPa), we developed a stress-strain relation assuming that the material would exhibit analogous yielding behavior to that of polytetrafluoroethylene (**Figure 2.12**).[67,68] The Poisson's ratio was assumed to be similar to those of typical fluoropolymers (0.499 or 0.5).[85] For the PDMS, we used an Ogden
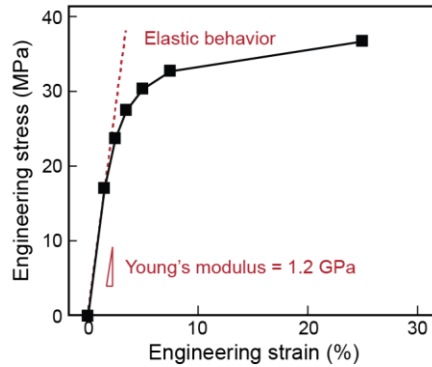
Figure 2.12. Proposed mechanical behavior of the fluoropolymer layer.

model, which accurately accounts for the stress-strain behavior we measured (*Section 2.4*) including the hyperelastic behavior observed at high strains.[93] To investigate plasticity effects, we compared the resulting wrinkle patterns with those predicted by a model based on a purely elastic CF_x layer.

The FEM model accounting for plasticity showed similar evolution of surface topography to that observed in the experiments (**Figure 2.13a**). When pre-strain ($\varepsilon_{pre} = 30\%$) in the PDMS substrate was relieved, the CF_x layer was stretched in the direction perpendicular to the strain relief (*y*-direction) beyond the elastic limit (1.5%). Because the plastic portion of the tensile strain was not recovered, compressive stress was generated along the *y*-direction in the CF_x layer when the PDMS substrate was stretched from the released state ($\varepsilon_x = 0\%$) to a strain equal to the pre-strain amount ($\varepsilon_x = 30\%$). As a result of the compression, intermediate structures were formed when ε_x > 15%. With increased ε_x, the average feature spacing decreased for two reasons: (1) the CF_x/PDMS slab was compressed perpendicular to the stretching direction; and (2) new trenches were formed between the existing ones. The lengths of the intermediate structures gradually increased and spanned the entire simulation sheet along the *x*-direction with increased ε_x. These features completely transformed to wrinkles with switched orientation when ε_x > 24%. When the
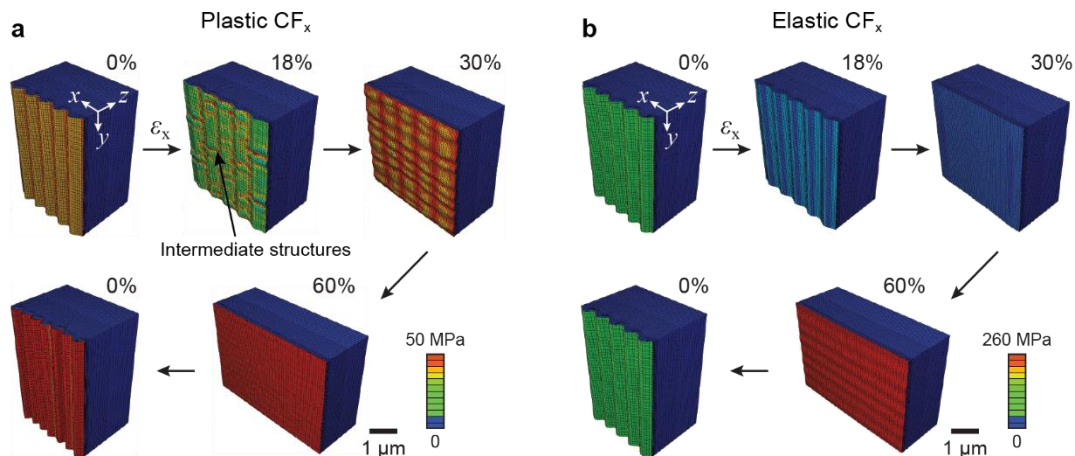
Figure 2.13. Plastic deformation in the CF$_x$ layer resulted in switching of wrinkle orientation *via* intermediate structures. CF$_x$/PDMS wrinkle patterns predicted from **(a)** plastic and **(b)** elastic CF$_x$ models ($\varepsilon_{pre} = 30\%$). Simulation slabs were 4 µm × 4 µm × 2 µm at $\varepsilon_x = 30\%$.

system was released after being stretched to $\varepsilon_x = 60\%$, the wrinkles switched back to the initial orientation with decreased λ_x and A_x. In contrast, simulations based on an elastic CF$_x$ layer model did not capture the experimental wrinkle pattern behavior (**Figure 2.13b**). Instead, the substrate became flat at $\varepsilon_x = 30\%$, and then new wrinkles formed at higher strain. Moreover, the system did not show changes in λ_x and A_x during the stretch-release cycle, which indicates that there was no structural hysteresis. Comparison of the two FEM models with AFM characterization suggests that plastic deformation of the CF$_x$ layer resulted in wrinkle orientation switching *via* intermediate structures and decreased wrinkle wavelength and amplitude after release of tensile strain.

2.8. **Switchable Anisotropic Wetting on Soft Skin Wrinkles**

One application of crack-free, mechano-responsive wrinkle patterns is switching the direction of liquid flow under controlled mechanical strain. This capability is critical for realizing stretchable microfluidics, microreactors, and directional water collection systems, where dynamic control over

fluids is needed. As a demonstration, we compared wetting on wrinkles in soft and hard skin layers under stretching ($\varepsilon_x = 40\%$) and releasing ($\varepsilon_x = 0\%$). The degree of wetting anisotropy was defined as the difference in static water contact angle measured perpendicular and parallel to the initial wrinkle orientation ($\Delta\theta = \theta_x - \theta_y$). Because water droplets typically spread along grooved patterns,[94-97] we expected $\Delta\theta$ to be positive at $\varepsilon_x = 0\%$ and negative at $\varepsilon_x = 40\%$. To deconvolute the effect of cracks on $\Delta\theta$, we chose wrinkles having similar wavelengths ($\lambda_{x,soft}$, $\lambda_{x,hard} = 740$ nm and $\varepsilon_{pre} = 30\%$) and similar surface chemistries by treating the silica skin layer with a fluorosilane (**Figure 2.14**).

As expected, the soft skin layer guided water spreading along the wrinkle orientation; $\Delta\theta$ was ~13° before stretching the substrate and became -6° under $\varepsilon_x = 40\%$ (**Figure 2.15a**). After release of the first stretched state, $\Delta\theta$ decreased to ~7° because of the reduced $A_{x,soft}$ (Figure 2.9b) since $\Delta\theta$ scales with the height of the features.[94-96] For subsequent stretch-and-release cycles, the surface alternated between positive and negative $\Delta\theta$ with nearly identical values because the wrinkle amplitude was maintained even after 500 cycles (Figure 2.9b). In contrast, wrinkles in the hard skin layer exhibited negative wetting anisotropy $\Delta\theta$ (-2°) before applying strain (**Figure 2.15b**). Although the initial contact angle perpendicular to the wrinkle orientation ($\theta_x = 138°$) was increased compared to that of the flat skin ($\theta_x = 110°$), droplet spreading along the wrinkles was
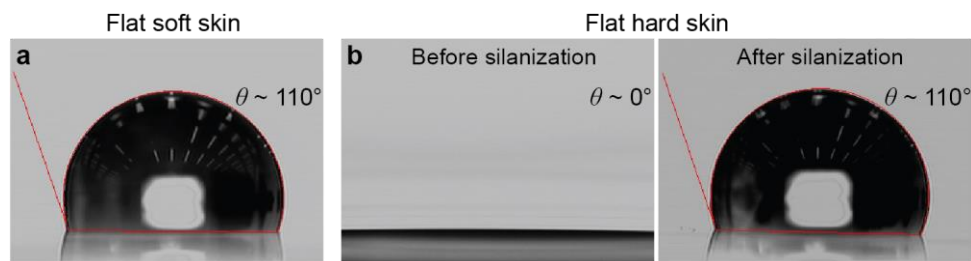
Figure 2.14. Static water contact angles on flat skin layers. Optical images of 3-µL water droplet on **(a)** soft and **(b)** hard skin layers. Hard skin showed nearly identical contact angle to that of soft skin after the fluorosilane treatment.
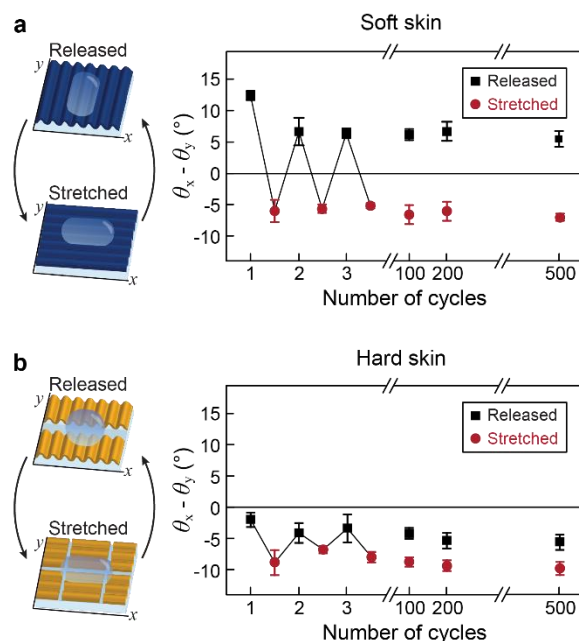
Figure 2.15. Switching anisotropic wetting by applying mechanical strain. Degree of anisotropic wetting on **(a)** soft skin and **(b)** hard skin wrinkles. The soft skin/PDMS system showed switching of anisotropic wetting because the surface was free of cracks.

hindered by the cracks ($\theta_y = 140°$). We attribute the increased θ_y to topography rather than surface chemistry of the PDMS in the cracks because the water contact angle of PDMS ($\theta \approx 110°$)[98] was similar to both the silica treated with fluorosilane and the fluoropolymer skin layer. Hard skin layers can only achieve negative $\Delta\theta$ under repeated stretching and releasing and cannot dynamically control the direction of water spreading. Comparison between the two systems confirmed that the defect-free nature of the soft skin layer and tolerance to stretch-release cycles were key factors that enabled switchable anisotropic wetting. Although $\Delta\theta$ values were smaller than those of silica/PDMS wrinkles,[63] our system offers advantages because dynamic switching between positive and negative $\Delta\theta$ is possible instead of only in a single (positive) direction. By optimizing structural parameters and surface chemistry based on sequential wrinkling,[70] we expect that $\Delta\theta$ values higher than reported in this work can be achieved.

2.9. **Methods**

2.9.1. *Preparation of PDMS Substrates*

Base polymer and crosslinking agent of a two-part elastomer kit (Sylgard 184, Dow Corning) were mixed at 10:1 mass ratio and degassed under vacuum for 90 minutes to remove bubbles. Then, the mixture was spin-coated (200 rpm, 60 s) on 3-inch silicon wafers and cured in an oven at 60 °C to produce PDMS sheets with ~0.5 mm thickness. After they were peeled from the wafer, the sheets were cut into rectangular slabs (60 mm × 15 mm) for wrinkle fabrication.

2.9.2. *Wrinkle Fabrication and Characterization*

PDMS substrates were first clamped in a custom-designed, uniaxial stretching apparatus (6061 aluminum alloy, McMaster-Carr) and stretched to achieve a targeted pre-strain value. The change in distance between two lines marked on the sample was used for determining the pre-strain: ε_{pre} = $(L - L_0)/L_0$, where L_0 and L are distances before and after stretching. The PDMS substrate was then treated with CHF_3 or O_2 plasma in a reactive ion etching (RIE) chamber (RIE-10NR, Samco Inc.) at a flow rate of 25 sccm and a power of 70 W under a pressure of 20 Pa. Typical CHF_3 and O_2 RIE times were 120 s and 600 s, respectively. After plasma treatment, the strain was slowly released from the PDMS (~0.2 mm/s). Surface topography of the resulting wrinkles were characterized using tapping-mode atomic force microscopy (AFM) (Dimension FastScan, Bruker). The reported wavelengths (peak-to-peak distance) and amplitudes (vertical displacement between troughs and valleys) represent an average of more than 100 measurements from different areas on each sample.

2.9.3. X-ray Photoelectron Spectroscopy of Skin Layers

Elemental composition and chemical bonding in the skin layers were investigated as a function of RIE time using x-ray photoelectron spectroscopy (XPS) (ESCALAB 250Xi, Thermo Scientific) equipped with a monochromatic Al K$_\alpha$ x-ray source (1486.7 eV). The beam was incident normal to the sample and the photoelectrons were analyzed with the pass energy of 50 eV and the dwell time of 50 ms. The resulting binding energy spectra were shifted with respect to the adventitious carbon contamination peak (284.8 eV) for charge correction and deconvoluted into peaks to quantify the atom content and bonding.

2.9.4. Ellipsometry Measurements of the Soft Skin Thickness

The thicknesses of the soft (CF$_x$) skin layers were measured using spectroscopic ellipsometry (M-2000, J. A. Woollam Co.) of CHF$_3$-plasma-treated PDMS slabs at different angles (from 45 to 65° in 5° increments) over wavelengths of 250-1000 nm. Scotch tape (3M) was attached to the backside of the samples to avoid reflection from the back surface. The measured ellipsometry constants (Ψ and Δ) were fitted to a skin-substrate Cauchy model to determine the skin thickness. The reported data were based on more than ten measurements.

2.9.5. X-ray Reflectivity Measurements of the Hard Skin Thickness

The thicknesses of the hard (SiO$_x$) skin layers were determined from x-ray reflectivity data (Smartlab, Rikagu) of O$_2$-plasma-treated PDMS slabs over scattering angles from 0° to 2° in 0.01° increments. The incident beam was generated from a Cu K$_\alpha$ source (λ = 1.542 Å) operated at 45 kV and 160 mA. Widths of the incident and receiving slits were 0.1 mm and 0.2 mm, respectively.

The reflectivity data were plotted as a function of the scattering vector ($Q = 4\pi/\lambda \sin\theta$) and fitted to a bilayer (skin/substrate) model to calculate the electron density profile and the skin thickness.

2.9.6. Scanning Electron Microscope Images of Cracks

Density and widths of the cracks in the hard skin were quantified using a scanning electron microscope (SEM) (LEO Gemini 1525, Carl Zeiss). Surfaces were coated with ~10 nm AuPd conductive layer (Desk III TSC sputter coater, Denton Vacuum) before SEM imaging.

2.9.7. Characterization of Anisotropic Wetting

Static water contact angles were measured (VCA Optima XE, AST Products, Inc.) perpendicular (θ_x) and parallel (θ_y) to the initial wrinkle orientation using 3 µL water droplets. The difference between θ_x and θ_y was defined as the degree of wetting anisotropy ($\Delta\theta = \theta_x - \theta_y$). Each data point represents at least five measurements.

2.9.8. Measurement of Young's Modulus of the Fluoropolymer Layer

Young's modulus of the fluoropolymer layer was measured using an atomic force microscope (Dimension ICON, Brucker) equipped with a PeakForce quantitative nanomechanical mapping (PeakForce QNM) module. A silicon tip with a spring constant of 42 N/m and a radius of 8 nm (TESPA, Brucker) was used to indent the fluoropolymer formed on PDMS substrates. We measured samples with CF_x thicknesses larger than 100 nm to avoid contributions from the substrate. Force curves from each approach-retract cycle were used to calculate the elastic modulus based on the Derjaguin−Muller−Toporov (DMT) model.[99] The reported value represents an

average of 512×512 measurements over a 5×5 µm^2 area.

2.9.9. Mechanical Modeling

Evolution of wrinkle topography was modeled based on continuum mechanics using the commercial finite element analysis software Abaqus/Explicit. The fluoropolymer layer ($h = 27$ nm) was modeled as either purely elastic or plastic with a Young's modulus measured from AFM (1.2 GPa). The Poisson's ratio was assumed to be similar to those of typical fluoropolymers (0.499 or 0.5).[85] The PDMS substrate was described with an Ogden model to account for hyperelastic behavior.[93] Stress-strain data from tensile testing (ASTM D412)[84] was used to determine the Ogden parameters. We set Poisson's ratio to 0.49 as PDMS is known to be nearly incompressible.[84]

We used cuboids with lengths and widths of 4 µm and thicknesses of 2 µm to simulate wrinkling at different strain states. The simulation slabs were discretized using C3D8R elements, which were 50 nm by 50 nm in lengths and widths with thicknesses of 13.5 nm for the top 100 nm, 25 nm for the next 200 nm, 50 nm for the next 200 nm, and 100 nm for the rest. To apply a target pre-strain ($\varepsilon_{pre} = 30\%$), we introduced the corresponding pre-stress in the PDMS substrate based on the stress-strain relation. The pre-stress was then released by moving simulation walls at quasistatic rates while fixing the base of the PDMS in the direction perpendicular to the initial surface normal. Abaqus was set to account for nonlinearity effects because displacements and deformations were large in some cases. To ensure that the systems assumed minimum energy states upon strain-relief, we ran tests with small load perturbations (3 % of the forces operating at a given pre-stress). From the resulting wrinkle patterns, we investigated the evolution of surface topography under increasing tensile strain.

2.10. **Summary and Outlook**

In summary, we demonstrated that a soft skin layer deposited on elastomeric substrate allows crack-free wrinkling up to high strain. A side-by-side comparison of wrinkle wavelength, amplitude, and orientation switching in soft and hard skin layers revealed fundamental differences between the crack-free and crack-based systems. Cyclic transformation of wrinkle topography under mechanical stimuli without delamination and defects enabled long-term stability of the soft-skin surfaces, which opens prospects in programmable mechano-responsive patterns. With exquisite control over external strain and starting wrinkle geometries, crack-free, soft materials systems can be used in directional water transport, dynamic self-assembly, and controlled capture-and-release surfaces.

Chapter 3

Reconfigurable Multiscale Wrinkles in Two-Dimensional Materials

This chapter reports a method to realize crack-free wrinkles in two-dimensional materials such as monolayer graphene and molybdenum disulfide with variable spatial wavelengths and switchable orientations. Graphene supported on a thin fluoropolymer and pre-strained elastomer substrate can exhibit conformal wrinkling after strain relief. The wrinkle orientation could be switched beyond the intrinsic fracture limit of graphene for hundreds of cycles of stretching and releasing without forming cracks. Mechanical modeling revealed that the fluoropolymer layer mediated the structural evolution of the graphene wrinkles without crack formation or delamination. Patterned fluoropolymer layers with different thicknesses produced wrinkles with controlled wavelengths and orientations while maintaining the mechanical integrity of graphene under high tensile strain.

Related publication:

3.1. **Introduction**

Two-dimensional (2D) materials are driving advances in next-generation electronics because of their unique electronic properties and mechanical flexibility compared to bulk counterparts.[100-104] Control of the electronic band gap or charge carrier type by nanopatterning is an effective means to tune the characteristics of 2D material-based devices.[105-108] Most efforts have focused on tailoring electronic properties by etching nanohole arrays in the 2D layers or chemically functionalizing the surface, but these processes typically damage the lattice.[109-113] In contrast, texturing of the 2D materials can engineer the properties and maintain structural integrity.[114-116] For example, nanoscale graphene crumples formed after strain relief of pre-strained elastomer sheets show controlled electrical conductivity and enhanced light absorption depending on feature size and orientation.[117-119] Because surface topography of textured graphene can be changed by stretching or bending the substrate, dynamic and reversible modification of properties is possible.[34,120] Delaminated crumpling, however, cannot be used to obtain area-specific properties because the process can only produce nanostructures with globally uniform wavelength and ordering.[34,120] Furthermore, the tunability range of crumpled graphene under stretching is limited since graphene cracks under tensile strain, especially in delaminated regions.[117,121,122]

Maintaining conformal contact between graphene and polymer substrates is advantageous for controlling the feature size and orientation of textured graphene in spatially defined regions. Using adhesive fluoropolymer layers patterned with different thicknesses, we created graphene wrinkles with locally distinct wavelengths and orientations on thermoplastic sheets.[123] One drawback of the thermoplastic system, however, is that changing surface topography *via* mechanical deformation is only possible at temperatures above the glass transition temperature of the substrate (typically

100 °C). In contrast, elastomeric substrates coated with a fluoropolymer layer could create reconfigurable graphene wrinkles at room temperature, but preserving the mechanical integrity of graphene may be challenging because thin films often delaminate from the surface, starting at the boundaries between regions of different heights.[124] Moreover, graphene cracks when the underlying substrate is stretched more than the pre-strained amount.[120,121]

In this chapter, we show that conformal wrinkling of graphene on elastomeric substrates can result in multiscale features that can simultaneously switch orientation under mechanical strain. Graphene was transferred onto pre-strained polydimethylsiloxane (PDMS) substrates coated with a soft fluoropolymer layer and then generated wrinkles following strain relief. The fluoropolymer layer suppressed cracks in graphene even up to tensile strains ~670% higher than the intrinsic fracture strain of graphene. Moreover, graphene nanowrinkles could switch orientation under repeated stretching and releasing without forming cracks and delaminating, which was not possible without the soft fluoropolymer layer. Through mechanical modeling, we revealed that crack-free topographical evolution was possible because of plastic deformation in the fluoropolymer layer supporting the graphene sheet. Because graphene did not crack or delaminate at the boundaries between fluoropolymer layers of different thicknesses, switchable graphene wrinkles with locally different wavelengths could be realized with mechanical stability under high tensile strain.

3.2. **Conformal Graphene Wrinkles on Fluoropolymer Layers**

Figure 3.1a describes the process used to fabricate graphene wrinkles on elastomer substrates. A uniaxially pre-strained (ε_{pre}) PDMS sheet was first treated with a CHF_3 plasma to create a soft fluoropolymer (CF_x) layer. Then, centimeter-scale, monolayer graphene synthesized by chemical

vapor deposition (CVD) was transferred to the CF_x layer using a poly(methyl methacrylate) (PMMA) support layer. After removing the PMMA from graphene using acetic acid and ethanol, we released the mechanically strained PDMS substrate to create wrinkles with wavelength (λ) and amplitude (A) perpendicular to the strain relief direction. To identify the role of the CF_x layer in producing textured graphene, we compared graphene nanostructures formed with and without CHF_3 treatment on the PDMS substrate (ε_{pre} = 30%) (**Figures 3.1b-c**). Graphene wrinkles exhibited topographies similar to those with only the CF_x layer on PDMS, which suggests that conformal contact between graphene and the substrate was maintained during pre-strain relief (Figure 3.1b). Significantly, no noticeable cracks were observed in graphene wrinkles based on scanning electron microscopy (SEM) images. Without the CF_x layer, graphene locally detached
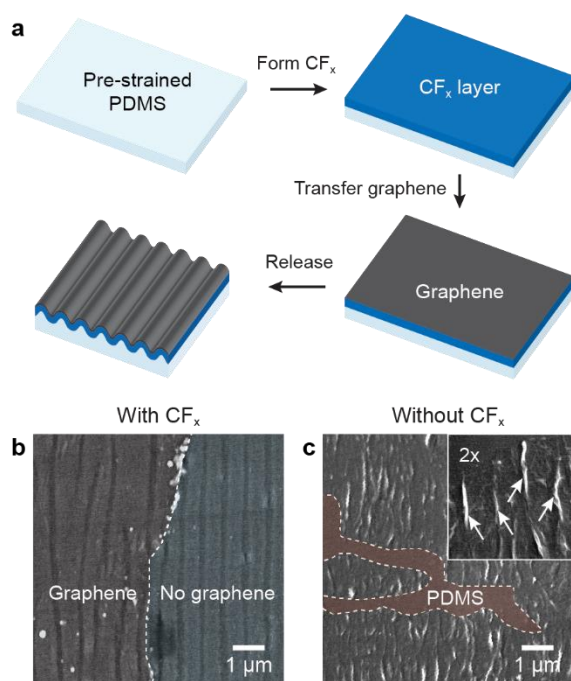
Figure 3.1. Soft CF_x layers for crack-free graphene nanowrinkles. **(a)** Scheme illustrating the fabrication process. Graphene was transferred to a pre-strained PDMS substrate coated with a CF_x layer, followed by strain relief to form wrinkles. False-colored SEM images of graphene upon releasing the substrate **(b)** with and **(c)** without the CF_x layer (30% pre-strain). Arrows in the inset indicate delaminated buckles in graphene.

from the surface and formed delaminated buckles with a width and an average spacing of ~30 nm and ~270 nm, respectively (Figure 3.1c). Consistent with previous work on graphene buckles,[121,125] cracks formed parallel to the strain relief direction.

We further confirmed that graphene was conformal to the underlying support from atomic force microscopy (AFM) force-distance curves measured on the peaks and valleys of wrinkles (**Figure 3.2**). Different from delaminated graphene that exhibits two distinct regimes with different slopes in the approach and retract curves,[123] wrinkled graphene showed a single slope because graphene was conformal to the fluoropolymer layer. In addition, the slope and adhesion force on peaks and valleys were similar (0.7 ± 0.1 N/m and 9 ± 1 nN, determined from 5 measurements). which further demonstrates conformal contact between graphene and the underlying support.

Although the thickness of graphene (0.34 nm)[126] was much smaller than that of the CF_x layer ($h = 27$ nm), the wavelength of the graphene wrinkles (980 nm) was ~32% larger than the CF_x/PDMS wrinkles (740 nm). To understand the observed increase in the wrinkle wavelength with the presence of graphene, we compared measured wavelengths with theoretical predictions based on composite beam theory (**Table 3.1**).[127] The effective Young's modulus of the
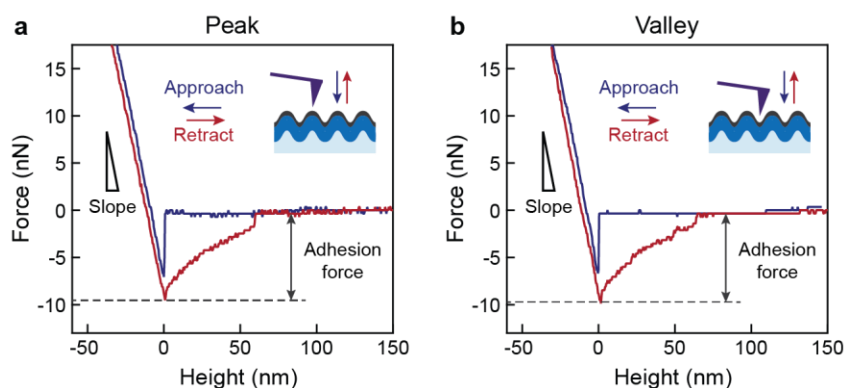
Figure 3.2. AFM force-distance curves measured on graphene wrinkles. Representative curves on **(a)** peaks and **(b)** valleys of the wrinkles. Spring constant of the AFM cantilever was 15.7 N/m.

graphene/fluoropolymer composite skin layer (E_{comp}) can be expressed as

$$E_{comp} = \frac{1 + m^2 n^4 + 2mn(2n^2+3n+2)}{(1+n)^3(1+mn)} E_{CF_x}$$ (3.1)

where m is the ratio of the Young's moduli of graphene (E_{gr}) and fluoropolymer (E_{CF_x}) ($m = E_{gr}/E_{CF_x}$ and n is the thickness ratio of graphene (h_{gr}) and fluoropolymer (h_{CF_x}) ($n = h_{gr}/h_{CF_x}$).[127] With the Young's moduli of the composite skin layer and the PDMS substrate (E_{PDMS}), we calculated the wrinkle wavelength (λ) based on finite-deformation buckling theory:[20]

$$\lambda = \frac{2\pi h_{comp}(\bar{E}_{comp}/3\bar{E}_{PDMS})^{1/3}}{(1 + \varepsilon_{pre})(1 + \xi)^{1/3}}$$ (3.2)

where $h_{comp} = h_{gr} + h_{CF_x}$ is the thickness of the composite skin layer, $\bar{E} = E/(1 - v^2)$ is the plane-strain modulus, v is the Poisson ratio, ε_{pre} is the amount of pre-strain applied to the substrate, and $\xi = 5\varepsilon_{pre}(1 + \varepsilon_{pre})/32$. From calculation based on the mechanical properties of graphene ($E_{gr} = 1$ TPa, $h_{gr} = 0.34$ nm, and $v_{gr} = 0.19$) and the fluoropolymer ($E_{CF_x} = 1.2$ GPa, $h_{CF_x} = 27$ nm, and $v_{CF_x} = 0.5$), we found that contribution of graphene in increasing the wrinkle wavelength (32%) observed in experiment was in agreement with the theoretical analysis, which predicts that

Table 3.1. Comparison of wrinkle wavelengths from experimental measurements and theoretical calculation.

	Young's modulus	λ from experiment	λ from calculation
Graphene/fluoropolymer	4.4 GPa	980 nm	1200 nm
Fluoropolymer only	1.2 GPa	740 nm	800 nm

graphene functions as an effective skin layer and will increase the λ of wrinkles by ~50%.

We compared the surface topographies of graphene wrinkles and delaminated buckles formed from different pre-strains to confirm the importance of conformal wrinkling in suppressing cracks (**Figures 3.3a-b**). During strain relief, the PDMS substrate expands perpendicular to the strain relief direction and applies tensile strain to graphene. Because metal thin films supported by polymer substrates can be stretched without significant cracking to strains more than five times higher than their free-standing counterparts,[37,128,129] we expected graphene to be more resistant to crack formation with the presence of the CF_x layer. To investigate strain regimes beyond the intrinsic fracture strain of CVD graphene (~9%),[130] we tested pre-strains up to 70%, which applies ~30% tensile strain to graphene perpendicular to the pre-strain direction during strain relief because the Poisson's ratio of PDMS ~ 0.5. As expected, conformal wrinkling suppressed cracking in graphene: for the entire range of pre-strains studied, graphene wrinkles only showed minor tears with widths less than 50 nm (Figure 3.3a). Notably, the maximum strain tested (~30% tensile) was more than 30 times higher than the experimentally reported fracture strain of free-stranding CVD graphene, which breaks under stretching less than 1% because of strain concentration at nanosized
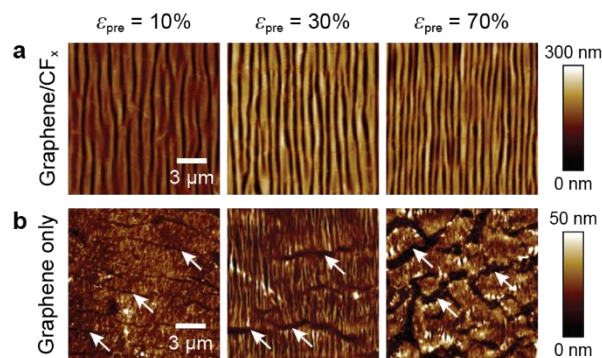
Figure 3.3. Conformal wrinkling suppressed cracking in graphene during strain relief of substrates. AFM images of graphene nanostructures formed (**a**) with and (**b**) without the CF_x layer at different pre-strains. Cracks are indicated with arrows. Images are 15×15 μm^2.

defects.[131] Without the fluoropolymer, cracks formed in graphene, and graphene delaminated from the substrate (Figure 3.3b). The crack widths increased from 160 nm to 820 nm when ε_{pre} increased from 10% to 70%. Besides conformal contact, the higher Young's modulus of CF_x (1.2 GPa) compared to PDMS (1.6 MPa) is also important for mechanical robustness of wrinkled graphene since a skin/polymer composite is more resistant to crack formation when the Young's modulus of the polymer support is large.[37]

3.3. Origin of Robust Adhesion Between Graphene and Fluoropolymer

To understand further how the CF_x layer mitigates crack formation, we analyzed Raman spectra of the graphene before and after forming nanostructures (**Figure 3.4**). Typically, graphene interacts with surfaces through either weak van der Waals forces with minimal changes in the electronic properties or stronger electrostatic attractions that cause charge doping.[132-134] The type of graphene-substrate interactions can be identified by investigating three characteristic features in the Raman spectra: (1) positions of G and 2D peaks; (2) the full width at half maximum of the G peak ($FWHM_G$); and (3) the ratio of 2D and G peak intensities (I_{2D}/I_G).[134-136] Flat graphene on the PDMS substrate showed G and 2D peaks located at 1583 cm^{-1} and 2670 cm^{-1} (**Figure 3.4a**) similar to a free-standing graphene that is nearly charge-neutral.[135,137] In addition, the $FWHM_G$ (13.8 ± 0.6 cm^{-1}) and I_{2D}/I_G (3.6 ± 0.8) values were close to undoped graphene, which suggests that graphene was bonded to PDMS through weak van der Waals forces with marginal charge doping ($< 2\times10^{11}$ cm^{-2}).[134-136] In contrast, the CF_x layer caused notable shifts in G and 2D bands toward higher wavenumbers (1594 cm^{-1} and 2680 cm^{-1}), resulting in decreased $FWHM_G$ (11.8 ± 1.0 cm^{-1}) and I_{2D}/I_G (1.9 ± 0.5) (**Figure 3.4b**). These spectral changes can be attributed to hole
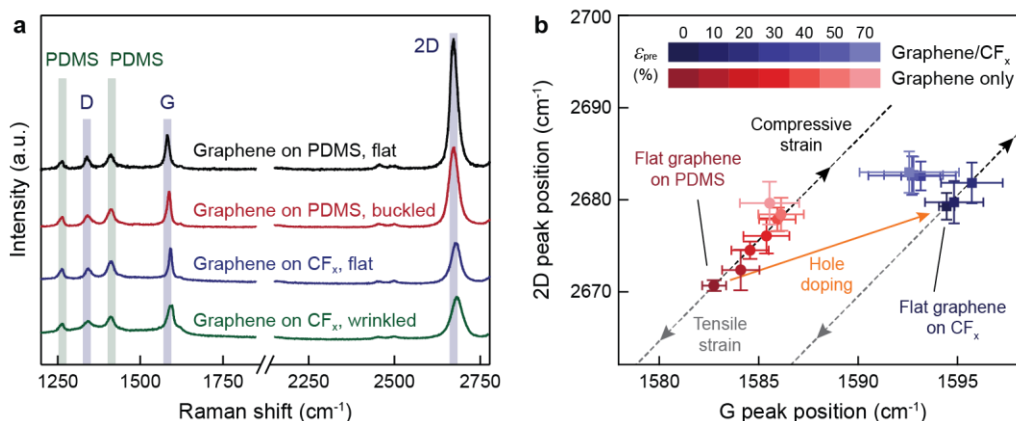
Figure 3.4. Deconvolution of interfacial forces and lattice strain during graphene texturing by Raman spectroscopy. (a) Representative Raman spectra measured on flat and textured graphene ($\varepsilon_{pre} = 30\%$). **(b)** Plot showing correlation between Raman G and 2D peak positions. Pre-strain levels are described with different shades of colors.

doping (4×10^{12} cm^{-2}) rather than electron injection or mechanical strain because the G and 2D peak positions followed a trend line expected for graphene doped with holes at a constant strain (solid orange line with a slope of 0.74, Figure 3.4b).[135,136] The electrostatic forces involved with hole doping may account for the robust adhesion between graphene and the CF$_x$ layer during the conformal wrinkling process.

Because the amount of shift in the 2D peak position in nanostructured graphene relative to flat graphene scales with strain level,[138] we compared the strain generated by textured graphene with and without the CF$_x$ layer. Raman 2D peaks for both graphene wrinkles and delaminated buckles shifted toward higher wavenumbers with increasing ε_{pre} because more strain was applied to graphene upon strain relief of the PDMS substrate (**Figure 3.5**). Notably, conformal graphene wrinkles showed smaller shifts compared to delaminated buckles for all tested pre-strains, which indicates that the CF$_x$ layer reduced strain in graphene during texturing. To verify that the changes in Raman spectra did not result from additional charge doping, we analyzed the relation between G and 2D band positions (Figure 3.4b). Wavenumbers of the peaks for delaminated buckles closely
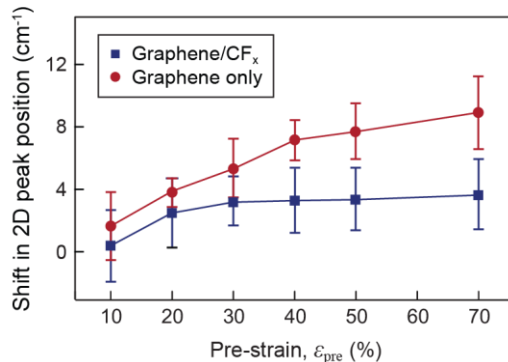
Figure 3.5. Shift in Raman 2D peak of textured graphene relative to the flat state as a function of substrate pre-strain. Blue and red data sets correspond to conformal wrinkles and delaminated buckles, respectively.

followed a line with a slope of 2.2 (black dashed line), which suggests that relief of pre-strain applied compressive strain to the uncracked regions in graphene without charge doping.[135] Similarly, conformal graphene wrinkles exhibited the expected correlation between G and 2D peak positions for graphene under compressive strain at a fixed hole concentration (black dashed line with slope of 2.2)[135] as ε_{pre} increased from 0% to 20%. Under higher ε_{pre} ($> 20\%$), the data deviated from the expected trend most likely because of tensile strain perpendicular to the strain relief direction and non-uniform strain distribution near the grain boundaries in CVD graphene.[138]

3.4. **Reconfigurability of Conformal Graphene Wrinkles**

By applying tensile strain to the PDMS substrate, we tuned the surface topography of the graphene nanowrinkles ($h = 27$ nm and $\varepsilon_{pre} = 30\%$) (**Figure 3.6a**). When the system was stretched in the direction perpendicular to the wrinkle orientation (x-direction), the wavelength (λ_x) gradually increased from 980 nm to 1.4 µm when ε_x was increased from 0 to 30%; the amplitude (A_x) decreased from 190 nm to 20 nm. Simultaneously, trench-like intermediate structures formed at random locations to accommodate compressive strain perpendicular to the stretching direction (y-
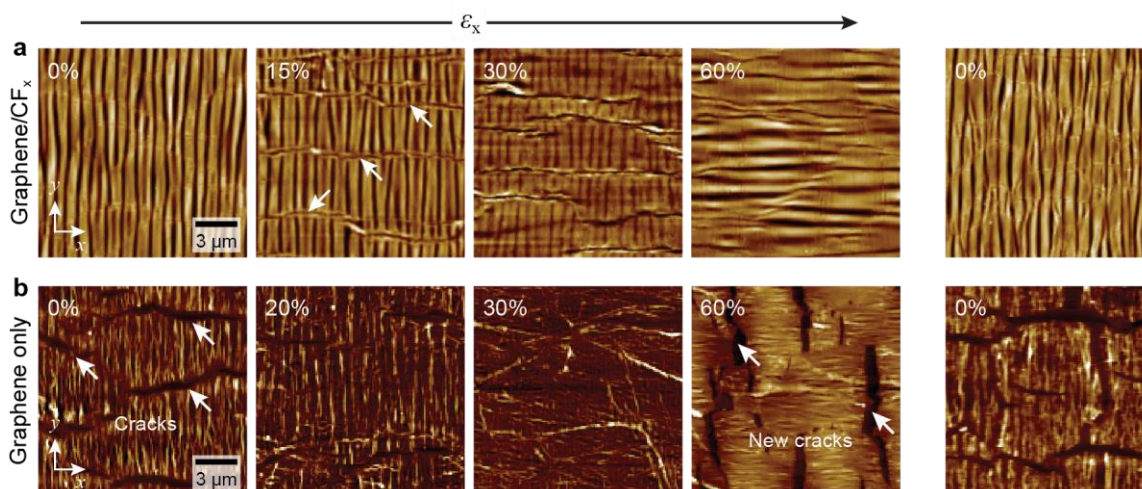
Figure 3.6. Dynamic tuning of graphene nanotextures by applying strain. AFM images of **(a)** conformal wrinkles and **(b)** delaminated buckles under tensile strain ($\varepsilon_{pre} = 30\%$). Both nanotextures showed complete switching of orientation when the substrate was stretched more than 30%. Images are 15×15 μm^2.

direction). The average spacing between these features decreased with increased strain. When the tensile strain equaled the pre-strain ($\varepsilon_x = 30\%$), the graphene/CF_x composite layer showed wrinkles and intermediate structures. This behavior is different from elastic skin materials that recover flat geometries when the substrate is stretched to the pre-strain amount.[20,139,140] As we applied even higher tensile strain to the system ($\varepsilon_x > 30\%$), the intermediate structures evolved into wrinkles with an orientation parallel to the tensile strain direction, and the initial wrinkle features disappeared. The spatial uniformity of the new wrinkle wavelength (λ_y) and amplitude (A_y) gradually increased under increasing strain. λ_y decreased from 1.3 μm to 1.1 μm, and A_y increased from 85 nm to 150 nm as ε_x increased from 40% to 60%. Notably, only minor tears were observed even when the system was stretched to 100% (70% more than ε_{pre} and ~670% more than the intrinsic fracture strain of CVD graphene). Accessing this high strain regime without graphene cracking was not possible without the CF_x layer (**Figure 3.6b**), which highlights the advantage of our conformal wrinkling approach. Once the substrate was released from 60% stretching, the

wrinkles recovered their initial orientation with slightly smaller wavelength and amplitude ($\lambda_x \approx$ 950 nm, $A_x \approx 180$ nm). The wrinkle orientation could be switched multiple times while maintaining λ and A both at the stretched ($\varepsilon_x = 60\%$) and released ($\varepsilon_x = 0\%$) states without delamination of graphene or crack formation (**Figure 3.7a-b**). Futuremore, ratios of Raman D and G peak intensities (I_D/I_G) were nearly constant during 1000 stretch-release cycles (~0.20 and ~0.25 for stretched and released states), which suggests that repeated switching of wrinkle orientation did not cause atomic-scale damage in graphene (**Figure 3.7c**).
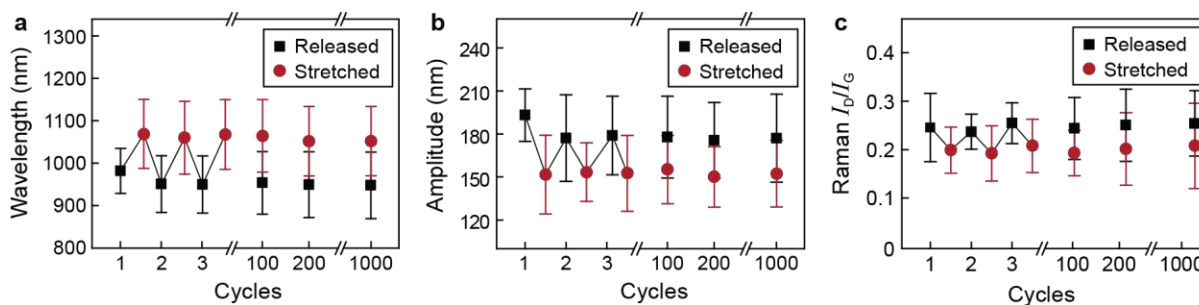
Figure 3.7. Durability of conformal graphene wrinkles. Plots showing **(a)** wavelength and **(b)** amplitude of graphene wrinkles during 1000 stretch-release cycles up to 60% tensile strain. **(c)** Intensity ratios of Raman D and G peaks at different cycle numbers.

3.5. **Role of Fluoropolymer in Mediating Wrinkle Orientation Switching**

We compared graphene/CF_x/PDMS (Figures 3.6a) and CF_x/PDMS wrinkles (Figure 2.10a) at different tensile strains side-by-side to identify the role of the CF_x layer in mediating structural transformation in the graphene-containing system. The response of λ and A of CF_x/PDMS wrinkles showed trends similar to graphene/CF_x/PDMS wrinkles. Under tensile strain lower than the pre-strain amount ($\varepsilon_x < 30\%$), λ_x increased while A_x decreased with increasing ε_x. When the substrate was stretched further ($\varepsilon_x > 30\%$), λ_y decreased while A_y increased. Wrinkles returned to their initial orientation upon release, with slightly smaller λ_x and A_x. Wrinkles in the CF_x layer also switched

orientations *via* intermediate structures that formed parallel to the stretching direction. Because graphene supported on bare PDMS did not exhibit these features (Figure 3.6b), we conclude that the CF_x layer plays a dominant role in the structural evolution of conformal graphene wrinkles. Interestingly, complete switching of the wrinkle orientation in the CF_x/PDMS system occurred at lower strain compared to the case with graphene; even at $\varepsilon_x = 30\%$, wrinkles with the switched orientation were distinct.

Based on the plastic CF_x layer model we developed in *Section 2.7.2*, we further examined interactions between graphene and the CF_x during crack-free wrinkle orientation switching (**Figure 3.8a**). Graphene can be described as an elastic sheet with a thickness of 0.34 nm, a Young's modulus of 1 TPa, and a Poisson's ratio of 0.19.[126] In contrast to the wrinkles without graphene (Figure 2.10a), intermediate structures did not form when the simulation slab was stretched. Resistance to these nanostructures can be attributed to an increased bending stiffness caused by the presence of graphene. Moreover, compressive strain in graphene perpendicular to the stretching direction was smaller than that in the CF_x layer because graphene has a smaller Poisson's ratio. As a result, the threshold strain for complete switching of graphene wrinkle orientation was larger (~30%) than that for the CF_x/PDMS wrinkles (~24%). After being released from the stretched state (up to 60%), graphene wrinkles returned to the initial orientation, but the switched (perpendicular) wrinkles did not completely disappear. We found that this structural hysteresis resulted from additional plastic deformation in the CF_x layer because of the graphene layer. Notably, strain in graphene throughout the stretch-release cycles was much lower than the intrinsic fracture strain (~9%) of CVD graphene.[130] After release of the 30% pre-strain, graphene was under ~1% tensile strain in the direction perpendicular to the strain relief. Even when the substrate was stretched to 60%, the maximum strain in graphene was only ~2% strain. In contrast,
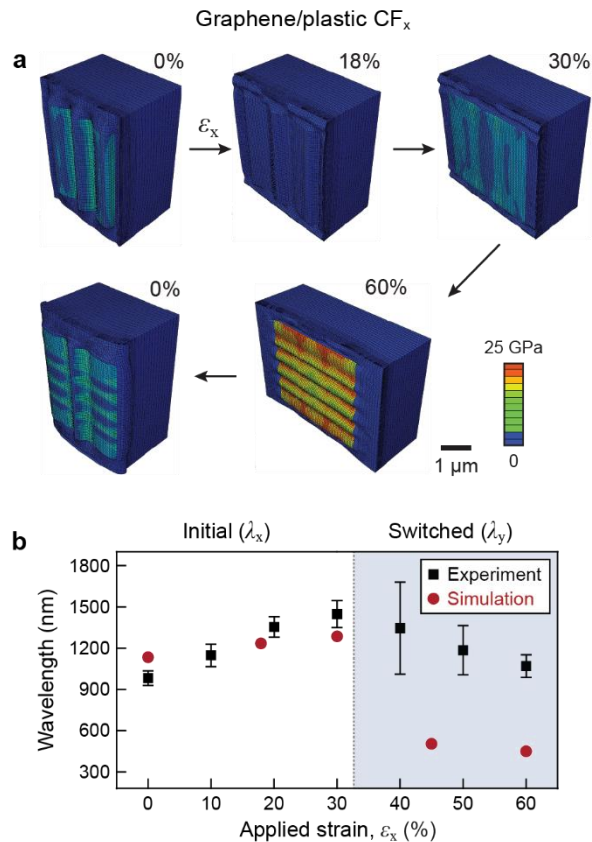
Figure 3.8. Simulated topographical transformation of conformal graphene wrinkles. (a) Predicted wrinkle structures based on the plastic CF_x model. **(b)** Comparison of simulation and experiment for graphene wrinkle wavelengths ($\varepsilon_{pre} = 30\%$). Dimensions of the simulation slab were 4 µm × 4 µm × 2 µm at $\varepsilon_x = 30\%$.

FEM simulations of delaminated graphene showed that stress concentrated at the detached areas, resulting in cracking.

The trends in structural parameters from FEM simulations were in good agreement with experimentally characterized wrinkle topography (**Figure 3.8b**). Wrinkles with the initial orientation gradually flattened in response to applied strain: λ_x increased while A_x decreased as ε_x increased up to 30%. New wrinkles with the switched orientation showed decreased λ_y with ε_x even though values at each strain were smaller than experimentally measured wavelengths. We attribute this disagreement to possible deviation of the proposed stress-strain relation describing

the CF_x layer from the actual plastic deformation behavior (Figure 2.12).

3.6. **Multiscale Graphene Wrinkles with Variable Spatial Wavelengths**

The advantage of conformal wrinkling compared to delaminated buckling is that feature sizes can be precisely tailored *via* design of the CF_x layer. By patterning CF_x layers with different thicknesses on the same PDMS substrate, we fabricated wrinkles with various spatial wavelengths side-by-side on a single graphene sheet (**Figure 3.9**). First, the surface of the pre-strained PDMS sheet was covered with polyvinylpyrrolidone (PVP) line patterns (15 µm width; 15 µm spacing) using inverse solvent-assisted nanoscale embossing.[141] After a CHF_3 plasma exposure and lift-off of PVP with ethanol, only the areas that were not covered by PVP lines were coated with the CF_x layer. Treating the surface with another CHF_3 plasma created two distinct regions with different layer thicknesses ($h_1 \sim 14$ nm; $h_2 \sim 27$ nm). After graphene transfer and strain relief of the substrate, microdomains with two distinct wrinkle wavelengths were formed ($\lambda_{1,x} \approx 500$ nm; $\lambda_{2,x} \approx 980$ nm) (**Figure 3.10a**). Graphene wrinkles in the two regions could switch orientation ($\lambda_{1,y} \approx 570$ nm; $\lambda_{2,y}$
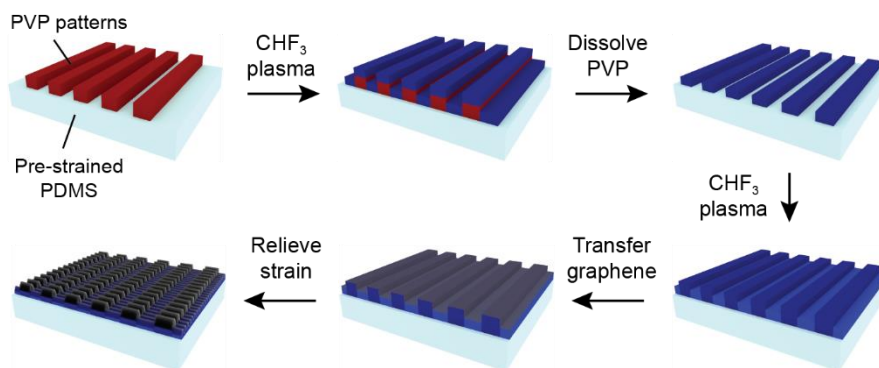
Figure 3.9. Process for creating area-specific, multiscale graphene wrinkles with switchable orientations. Graphene was first transferred on CF_x skin layers patterned with different thicknesses, followed by strain relief. After wrinkle formation, surface topography could be tuned in response to mechanical strain.
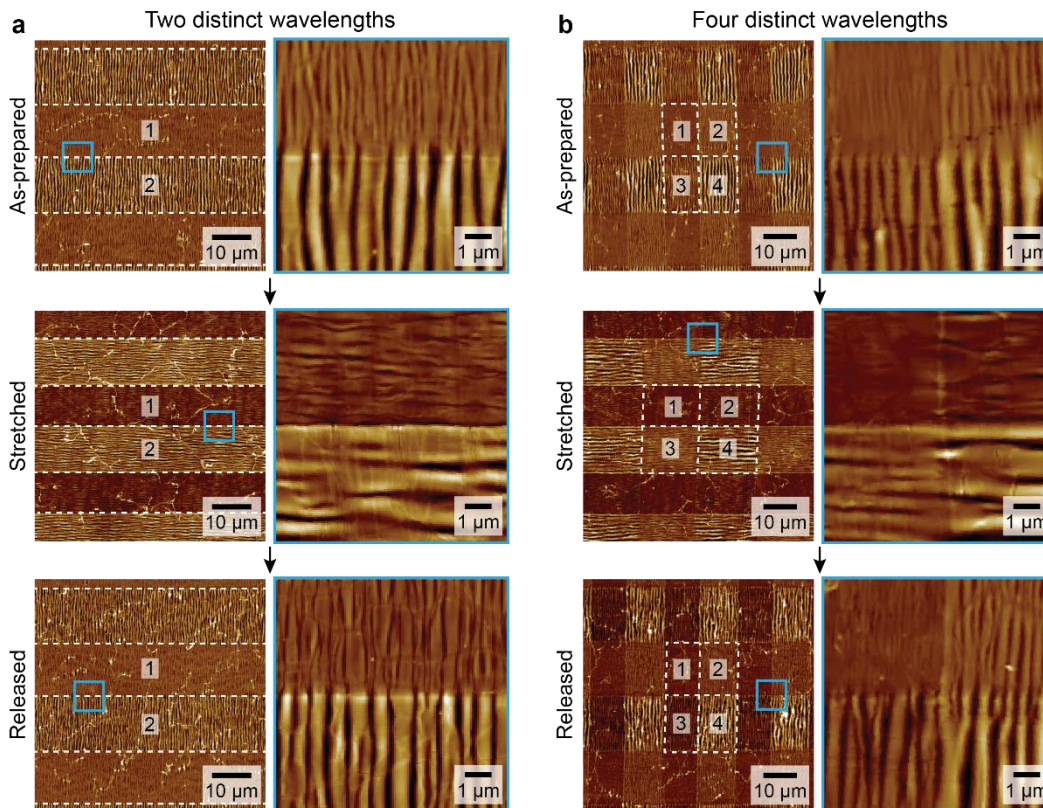
Figure 3.10. Switchable graphene wrinkles with locally different wavelengths. AFM images of graphene wrinkles formed on **(a)** two ($h_1 \sim 14$ nm; $h_2 \sim 27$ nm) and **(b)** four ($h_1 \sim 8$ nm; $h_2 \sim 14$ nm; $h_3 \sim 20$ nm; $h_4 \sim 27$ nm) domains with distinct fluoropolymer thicknesses (ε_{pre} = 30%). Stretched and released states correspond to $\varepsilon_x = 60\%$ and $\varepsilon_x = 0\%$.

≈ 1.1 μm) under stretching ($\varepsilon_x = 60\%$) and return to the initial orientation upon releasing. Further increase in the number of different wrinkle wavelengths was possible by additional cycles of area-selective CF_x layer deposition. For example, two patterned growth processes with lines perpendicular to each other followed by an unmasked CHF_3 plasma treatment created four regions with different CF_x thicknesses ($h_1 \sim 8$ nm; $h_2 \sim 14$ nm; $h_3 \sim 20$ nm; $h_4 \sim 27$ nm) on a pre-strained PDMS substrate. Upon strain relief, graphene wrinkles with four distinct wavelengths were generated ($\lambda_{1,x} \approx 330$ nm; $\lambda_{2,x} \approx 490$ nm; $\lambda_{3,x} \approx 670$ nm; $\lambda_{4,x} \approx 1000$ nm). Interestingly, the multiscale wrinkles individually switched orientations when the PDMS substrate was stretched to 60% tensile

strain ($\lambda_{1,y} \approx 370$ nm; $\lambda_{2,y} \approx 570$ nm; $\lambda_{3,y} \approx 710$ nm; $\lambda_{4,y} \approx 1.1$ μm) (**Figure 3.10b**). We found that

wrinkles in each domain exhibited wavelengths similar to those in graphene on an unpatterned CF_x

layer of the same thickness (**Figure 3.11**), which indicates that local structural features can be

precisely engineered through CF_x thickness. Crack formation and delamination were suppressed

during the stretch-release cycle because conformal contact between graphene and the patterned

CF_x layer was robust, even at edges between regions with different thicknesses.
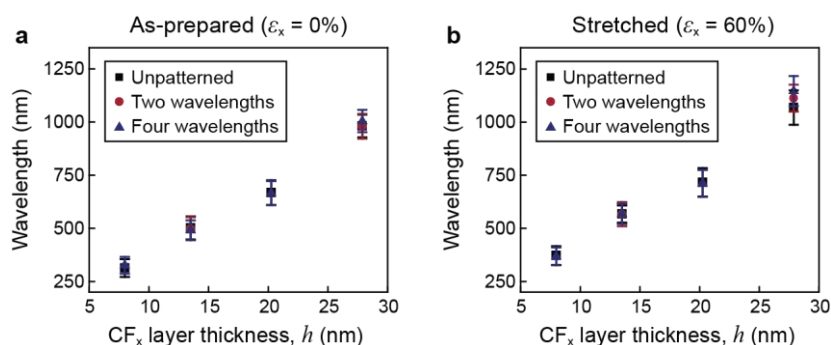
Figure 3.11. Graphene wrinkle wavelengths were similar on patterned and unpatterned CF_x layers. Plots showing wavelengths of **(a)** as-prepared ($\varepsilon_x = 0\%$) and **(b)** stretched ($\varepsilon_x = 60\%$) wrinkles.

3.7. **Wrinkled Monolayer Semiconductors with Tunable Photoluminescence**

Applying strain in the 2D materials can change overlap and hybridization of orbitals in the

lattice, which can result in tuning of electronic band structure.[142-144] Because atomically thin

nanomaterials can accommodate larger tensile strain than their bulk counterpart,[104,145] such strain

engineering has emerged as a beneficial strategy to tune the electronic and optical properties of the

2D materials. Wrinkling of 2D materials can introduce in-plane strain and out-of-plane bending to

the atomic lattice and change their physical properties such as mechanical stiffness, chemical

reactivity, and photoluminescence depending on the feature sizes.[115,123,146] Expanding our work on

graphene nanotextures, we applied our conformal wrinkle strategy to pattern other 2D nanomaterials and engineer their properties.

We focused on monolayer molybdenum disulfide (MoS_2) as a representative post-graphene 2D nanomaterial, which is a direct bandgap semiconductor with an optical bandgap of $1.8 - 1.9$ eV.[147] Centimeter-scale, monolayer MoS_2 was grown on a silicon dioxide (SiO_2) substrate by CVD using MoO_3 and sulfur precursors (provided by Professor Vinayak Dravid group at Northwestern University). We then transferred MoS_2 onto a CHF_3-treated polystyrene (PS) substrate using the PMMA-assisted wet transfer method outlined in *Section 3.2* (**Figure 3.12a**). First, a PMMA support layer was coated on MoS_2 samples by spin-coating, followed by etching of SiO_2 using KOH solution. The PMMA/MoS_2 was then rinsed with deionized water three times, transferred on water/ethanol mixture (1:1 volume ratio) and scooped with the PS sheet. After removing PMMA from MoS_2 with acetic acid and ethanol, we heated the sample at 135 °C to relieve pre-strain in
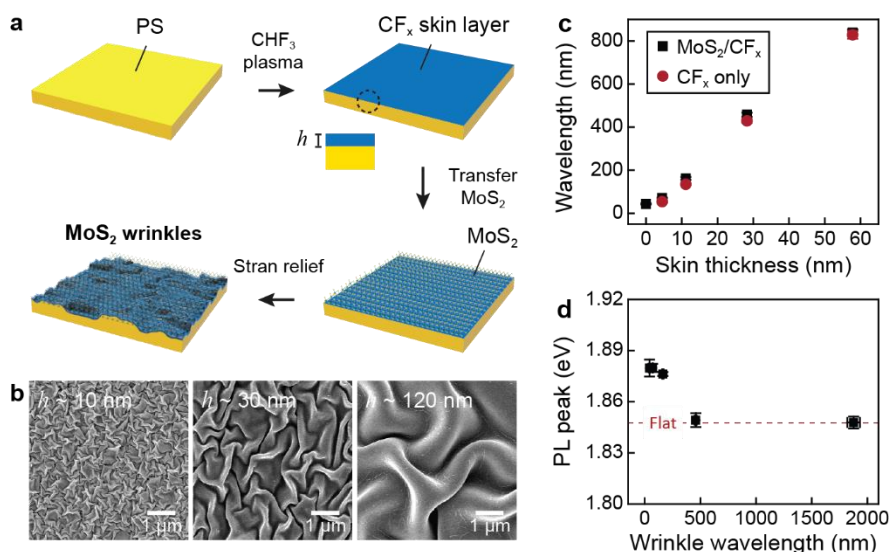
Figure 3.12. Conformal MoS₂ wrinkles with tunable photoluminescence. (a) Scheme describing the conformal wrinkling process on polystyrene substrates. **(b)** SEM images of MoS₂ wrinkles. **(c)** Wavelengths of MoS₂ and CF_x wrinkles for different CF_x thicknesses. **(d)** Peak photoluminescence energies as a function of wrinkle wavelength.

the PS substrate.

Figure 3.12b shows SEM images of the textured MoS_2 formed with different CF_x layer thicknesses at a fixed strain (biaxial, $\varepsilon_{2D} \approx 0.5$). Similar to graphene, MoS_2 exhibited conformal wrinkles with a wavelength that can be tuned by the CF_x thickness. For example, wavelength λ can be increased linearly from 160 nm to 1.9 μm by increasing the skin thickness h from 10 nm to 120 nm. By comparing wrinkle wavelengths of the MoS_2/CF_x composite and the CF_x film, we found that MoS_2 functioned as an effective skin layer and increased λ of the wrinkles (**Figure 3.12c**). When h was ~5 nm, the presence of MoS_2 increased λ by ~33%. The effect of MoS_2 in increasing λ was less significant for thicker CF_x layers (larger than 60 nm), where MoS_2 and CF_x wrinkles exhibited nearly identical wavelengths. Because out-of-plane nanostructures can introduce strain in the MoS_2 lattice that scales with the local curvature,[115] we hypothesized that the photoluminescence (PL) energy of MoS_2 can be engineered by tuning the wrinkle topography. Wrinkled MoS_2 exhibited PL peaks that were shifted toward higher energies, which suggests that conformal wrinkling process effectively applied compressive strain on MoS_2 (**Figure 3.12d**). As expected, the amount of shift was larger for smaller wrinkles because the peak curvature is inversely proportional to the wavelength ($\kappa \propto 1/\lambda$).[146,148]

Integrating textured MoS_2 on PDMS substrates enables dynamic control over structural parameters by mechanical stretching (**Figure 3.13a**). Similar to the method we used for creating conformal graphene wrinkles, we first formed a CF_x layer ($h = 27$ nm) on a uniaxially pre-strained PDMS sheet ($\varepsilon_{pre} = 30\%$), transferred MoS_2, and then relieved the strain to form 1D wrinkles. **Figure 3.13b** shows optical microscope images of MoS_2 wrinkles at different substrate strain parallel to the pre-strain. As expected from structural evolution of CF_x and graphene wrinkles, the

wrinkled MoS_2 flattened to accommodate tensile strain when ε_x was increased from 0 to 30%. At higher tensile strain ($\varepsilon_x > 30\%$), the MoS_2 exhibited wrinkles with a switched orientation that was perpendicular to the initial state. To investigate whether the optical properties can be dynamically modulated, we characterized photoluminescence of the textured MoS_2 during wrinkle orientation switching by external strain (**Figure 3.13c-d**). Upon relief of pre-strain ($\varepsilon_x = 0\%$), MoS_2 wrinkles exhibited PL peaked at ~1.87 eV resulting from effective compressive strain. As λ increased and A decreased (thus decreased local curvature) at $\varepsilon_x = 15\%$, shift in the PL peak relative to the flat state decreased. When tensile strain equaled the pre-strain amount ($\varepsilon_x = 30\%$), the peak PL energy was similar to that of the flat MoS_2. Notably, the switched-orientation MoS_2 wrinkles ($\varepsilon_x = 50\%$) were characterized by a PL peak shifted toward the higher energy, which indicates that compressive strain resulting from wrinkle topography rather than tensile strain from substrate
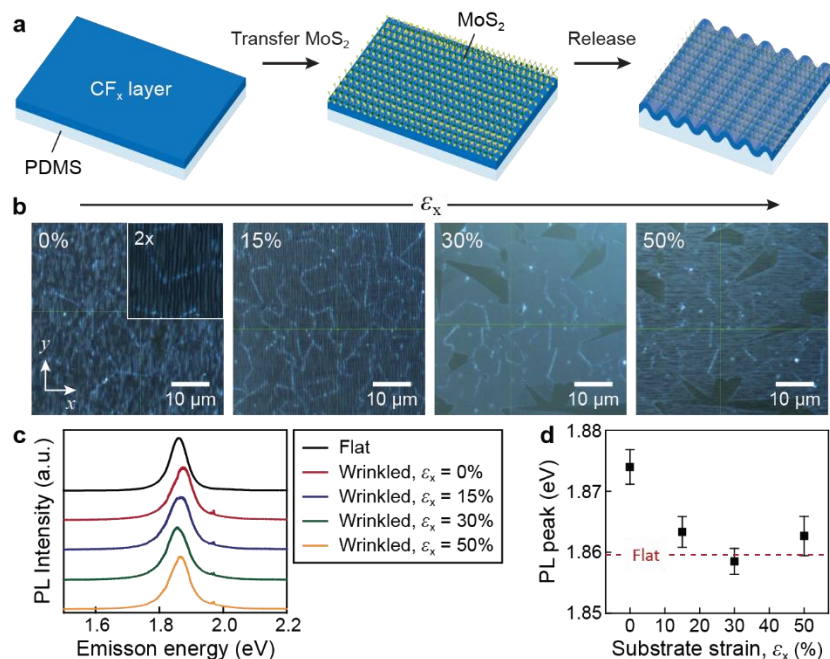
Figure 3.13. Mechano-responsive MoS_2 wrinkles with tunable photoluminescence. (a) Schematic illustration of the conformal wrinkling on PDMS substrates. **(b)** Optical images of MoS_2 wrinkles during wrinkle orientation switching by strain. **(c)** Photoluminescence spectra and **(d)** peak photoluminescence energies of MoS_2 wrinkles.

stretching dominates changes in PL properties of textured MoS_2.

3.8. **Methods**

3.8.1. *Preparation of PDMS Substrates*

PDMS substrates were prepared by the procedure described in *Section 2.9.1*. Base polymer and crosslinking agent of a two-part elastomer kit (Sylgard 184, Dow Corning) were mixed at 10:1 mass ratio and degassed under vacuum for 90 minutes to remove bubbles. Then, the mixture was spin-casted (200 rpm, 60 s) on 3-inch silicon wafers and cured in a convection oven at 60 °C to produce PDMS slabs with ~0.5 mm thicknesses. After being peeled off from the wafer, the sheets were cut into rectangular substrates (60 mm × 15 mm) for wrinkle fabrication.

3.8.2. *Application of Pre-Strain and Fluoropolymer Layer Formation*

As depicted in *Section 2.9.2*, PDMS substrates were clamped into a custom-designed, uniaxial stretching apparatus (6061 aluminum alloy, McMaster-Carr) and stretched to apply targeted pre-strains. Changes in the distance between two lines marked on the sample were used to determine the pre-strain: $\varepsilon_{pre} = (L - L_0)/L_0$, where L_0 and L are distances before and after stretching. The PDMS substrate was then treated with CHF_3 plasma in a reactive ion etching (RIE) chamber (RIE-10NR, Samco Inc.) at a flow rate of 25 sccm and a power of 70 W under a pressure of 20 Pa for 120 s to form fluoropolymer layers with $h = 27$ nm. Samples without the plasma treatment was used to form delaminated graphene buckles for comparison.

3.8.3. Graphene Transfer

Monolayer graphene synthesized *via* chemical vapor deposition on a copper foil (Sigma Aldrich) was transferred onto pre-strained PDMS substrates using the PMMA-assisted wet transfer process.[149] First, graphene was coated with a poly(methyl methacrylate) (PMMA) (495 PMMA A2, MicroChem Corp.) support layer. After etching graphene from the back side of the foil with O_2 RIE (15 sccm, 1.3 Pa, 10 W, 1 minute), we dissolved the copper by floating the PMMA/graphene/Cu stack on 0.1 M ammonium persulfate solution (Sigma-Aldrich) for 4 hours. The PMMA/graphene was then rinsed with deionized water three times, transferred on water/ethanol mixture (1:1 volume ratio), and scooped with the pre-strained PDMS substrate. Adding ethanol to water reduced the surface tension of the liquid media and promoted conformal coating of graphene on samples during the transfer process.[150] After evaporating the solvent in an oven at 40 °C for 6 hours, PMMA was removed from graphene with acetic acid and ethanol.

3.8.4. Atomic Force Microscopy

Surface topography of graphene wrinkles and delaminated buckles was characterized by tapping-mode atomic force microscopy (AFM) (Dimension ICON, Bruker). The reported wavelengths (peak-to-peak distance) and amplitudes (vertical displacement between peaks and valleys) represent an average of more than 30 measurements from different areas on each sample. Widths of minor tears in graphene wrinkles were determined from AFM images of three samples for $\varepsilon_{pre} = 30\%$. The average and standard deviation of 90 measurements (30 measurements per sample) are presented. A single sample was characterized for the other pre-strains because the tear width was consistent for different samples. To describe the widths of cracks in delaminated

graphene buckles, we fabricated three sets of samples and quantified the average and standard deviation of crack widths from 180 measurements for each pre-strain case (60 measurements per sample).

3.8.5. *Scanning Electron Microscopy*

Based on the method described in *Section 2.9.6*, Scanning electron microscope (SEM) images were obtained with field emission SEM (LEO Gemini 1525, Carl Zeiss). Samples were coated with a ~10 nm AuPd conductive layer (Desk III TSC sputter coater, Denton Vacuum) to prevent electron charging.

3.8.6. *Raman Spectroscopy*

Raman spectra were measured with a 532-nm excitation laser using a confocal Raman microscopy (LabRAM HR Evolution, Horiba). The excitation power was kept below 1mW to avoid damage to graphene. Raman scattering from samples was collected with an Olympus 100x objective and dispersed by a diffraction grating (1800 lines/mm). Focal spot size and depth resolution were approximately 1 µm. Each data point and error bar in Figures 3.4b, 3.5, and 3.7c represent the average and standard deviation from more than 10 measurements.

3.8.7. *Mechanical Modeling*

CF_x/PDMS bilayer composite was described by the plastic CF_x layer model we developed in *Section 2.7.2*. Monolayer graphene was approximated as a purely elastic sheet with a thickness of 0.34 nm, a Young's modulus of 1 TPa, and a Poisson's ratio of 0.19, and were discretized using

50 nm × 50 nm × 0.34 nm C3D8R elements.[126,151] We used the same discretization strategy and simulation procedure depicted in *Section 2.9.9* to simulate the evolution of graphene wrinkles in response to strain.

3.8.8. *MoS$_2$ Transfer*

Using the PMMA-assisted wet transfer method, monolayer CVD MoS$_2$ was transferred from the silicon dioxide substrate to the pre-strained polymer substrate. First, MoS$_2$ was coated with a PMMA (495 PMMA A2, MicroChem Corp.) support layer. We etched SiO$_2$ by floating the PMMA-coated sample on 2M KOH solution (Sigma-Aldrich) for 24 hours. The PMMA/MoS$_2$ was then rinsed with deionized water bath for three times, transferred on water/ethanol mixture (1:1: volume ratio), and scooped with the polystyrene or PDMS substrate. After evaporating the solvent in an oven at 40 °C for 6 hours, PMMA was removed from MoS$_2$ with acetic acid and ethanol.

3.8.9. *Photoluminescence Measurement*

Photoluminescence (PL) spectra were measured using a confocal Raman microscopy (LabRAM HR Evolution, Horiba) under a 532-nm laser excitation. The excitation power was kept below 1mW to avoid damage to MoS$_2$. PL from samples was collected with an Olympus 100x objective and dispersed by a diffraction grating (600 lines/mm). Focal spot size and depth resolution were approximately 1 µm. Each data point and error bar in Figures 3.12d and 3.13d represent the average and standard deviation from 3 measurements.

3.9. **Summary and Outlook**

In summary, we realized multiscale graphene nanowrinkles that can change wavelength and orientation at adjacent, spatially selective regions under tensile strain. Reversible structural transformations are possible during stretch-release cycles because cracks are suppressed when graphene is supported on the soft fluoropolymer layer. With rational design of the width and thickness of the patterned fluoropolymer layer, our conformal wrinkling strategy can produce customizable surface textures beneficial for applications in graphene-based electronic devices, plasmonics, nano-bio interfaces. We further demonstrated that the process can be applied to molybdenum disulfide for engineering photoluminescence. We expect that this lithography-free, scalable technique will offer a general means to engineer the local properties of graphene and other 2D materials.

Chapter 4

Multiscale Wrinkling of Two-Dimensional Materials Using Sacrificial Skin

This chapter depicts a facile process to create multiscale, hierarchical wrinkles on various two-dimensional materials. Wrinkles were formed by strain relief of a pre-strained thermoplastic sheet coated with a two-dimensional material and a solution-processible polymer overlayer, which could be removed from the surface by rinsing. The resulting wrinkle wavelength could be controlled by changing the thickness of the sacrificial polymer. The process could generate both out-of-plane hierarchical structures upon sequential cycles of sacrificial skin growth, strain relief, and rinsing, and in-plane hierarchical textures that resulted from wrinkling with skin layers patterned with locally different thicknesses. With control over feature sizes and structural hierarchy at different length scales, this work would serve a general approach for tuning properties of two-dimensional materials.

$4.1.$ **Introduction**

Patterning hierarchical structures into two-dimensional (2D) nanomaterials is beneficial for applications in electronics,[120,152] photonics,[153,154] and energy devices.[155-157] For example, graphene oxide films with three-generation hierarchical crumples showed 20-fold increase in current densities under cyclic voltammetry measurement compared to the planar counterpart because of increased area density.[155] To create this out-of-plane hierarchical textures, graphene oxide films were first formed on a pre-strained polystyrene (PS) sheet by drop casting, followed by strain relief to generate the first generation (G1) of crumples. The second generation (G2) crumples with a larger wavelength were then produced by transferring the textured film to another PS substrate and relieving the pre-strain. This process could be repeated to build the third generation (G3) or higher generation (G) features while maintaining previous-generation textures. Although the G1 crumple wavelength (λ_1) can be tuned by changing the thickness of graphene oxide film, λ of higher generation textures are determined by λ_1 and cannot be tuned independently. Our group previously demonstrated that sequential cycles of fluoropolymer (CF_x) skin growth followed by strain relief of the PS sheet can realize out-of-plane hierarchical wrinkles with λ of each G features precisely tuned *via* the skin thickness.[70] This process, however, has limitations for general skin materials because progressively thicker layers are needed to access higher G features. This thickness requirement may compromise the functionality of 2D electronic materials with thickness-dependent properties.[158]

Besides out-of-plane structural hierarchy, introducing in-plane hierarchical textures with spatially different wavelengths is also important for tuning properties of 2D materials.[123,146,152,154] Such patterning enables engineering of the local properties within a single sheet of 2D material,

which is difficult with the out-of-plane hierarchical nanostructures. Recently, graphene wrinkles with variable spatial wavelengths have been recently realized by transferring graphene on a pre-strained PS substrate patterned with CF_x layers of different thicknesses and relieving the strain.[123,146] Although this method can produce textured graphene with spatially defined feature sizes, there are some drawbacks for using this technique as a means to pattern general 2D materials: (1) creating CF_x layers with locally different thicknesses requires multistep masking and skin growth processes, (2) the method is only compatible with functional materials that are free-standing for wet transfer, and (3) films stiffer than graphene would delaminate from the surface during strain relief because of height differences at boundaries between patterned CF_x layers.

In this chapter, we present a wrinkling process based on sacrificial skin layers that can pattern arbitrary 2D materials with both out-of-plane and in-plane hierarchical wrinkles. Functional skin was first introduced on a pre-strained PS sheet either *via* transfer from a growth substrate or direct growth on the PS surface. Sequential cycles of polyvinylpyrrolidone (PVP) deposition, strain relief of the substrate, and PVP rinsing created multigenerational hierarchical textures with independent control over wavelength for each G features. Also, by molding PVP against a stamp patterned with different local heights, in-plane hierarchical wrinkles could form in the functional skin after relieving strain. Because the thickness of the sacrificial skin layer can be controlled by PVP concentration or stamp designs, our strategy can generate hierarchical structures with customizable feature sizes and orientations over multiple length scales within 2D materials.

4.2. Out-of-Plane Hierarchical Wrinkles with Multigenerational Features

4.2.1. Overview of the Process

Figure 4.1 depicts the method to transform flat functional materials into three-dimensional hierarchical architectures. First, we transferred a functional skin onto a pre-strained PS sheet. G1 wrinkles were formed after relieving strain (ε_1) by heating the substrate above the glass transition temperature of PS ($T_g = 100\ °C$). Next, G2 wrinkles with a larger wavelength were generated by spin-coating a PVP solution with thickness h_2 on the nanopatterned surface, followed by a second strain relief (ε_2). The surface of textured functional skin material was revealed after dissolving the sacrificial PVP layer with ethanol. Interestingly, the G1-G2 wrinkles were not deformed during removal of the PVP skin. By repeating cycles of PVP casting, strain relief, and PVP dissolution, we could build multigenerational architectures with programmable structural hierarchy: for
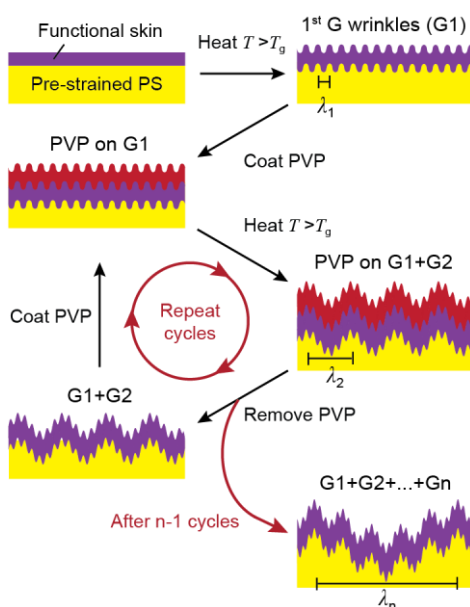
Figure 4.1. Hierarchical wrinkling of functional skin layers using sacrificial polymer films. G1 wrinkles were first formed by strain relief of the PS substrate coated with the functional skin layer. Higher generation wrinkles were introduced by sequential cycles of PVP deposition, strain relief, and PVP removal.

example, hierarchical surfaces with *n* characteristic wrinkle wavelengths were formed after *n-1* cycles.

4.2.2. Design Principles of Wrinkle Topography Using Sacrificial Skin Layers

We first investigated single-generation wrinkles formed on PS substrates without functional skin materials to identify the design rule to tune the wrinkle wavelength using PVP layers (**Figure 4.2**). We changed the concentration of spin coating solution to control the thickness of the PVP layer while keeping the spinning speed the same (4000 rpm). **Figure 4.2a** shows SEM images of wrinkles formed by spin casting PVP solutions at different concentrations, relieving strain in PS ($\varepsilon_{2D} \approx 0.4$), and then rinsing the surface with ethanol to remove PVP. By increasing the PVP concentration, we could produce wrinkles with larger wavelengths. To confirm whether the increase in λ resulted from increased PVP thickness for higher PVP concentrations, we performed
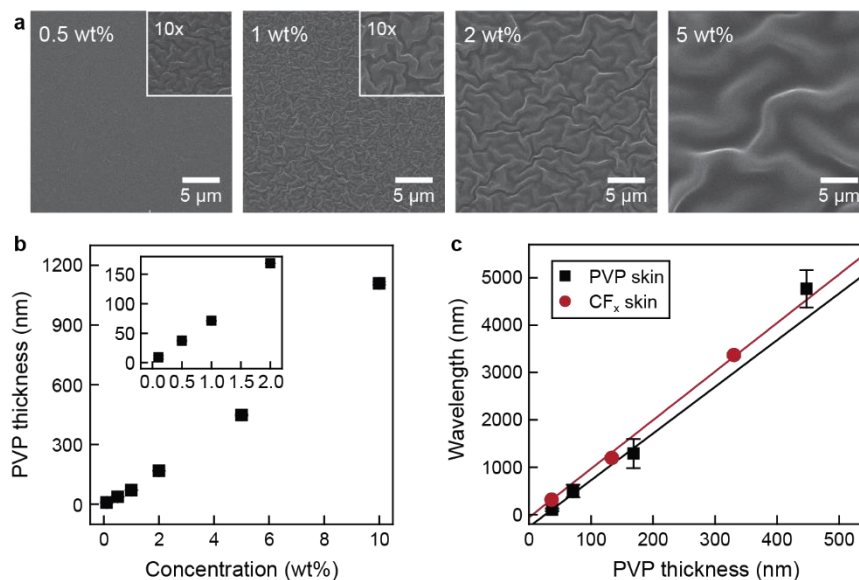
Figure 4.2. Tunability in wrinkle wavelength of the PVP/PS bilayer system. (a) SEM images of wrinkles formed with different concentrations of PVP solution. **(b)** Thickness of sacrificial skin layers resulting from spin coating PVP solution at different concentrations. **(c)** Relation between PVP thickness and the resulting wrinkle wavelength.

ellipsometry measurements on PVP-coated polystyrene samples before strain relief (**Figure 4.2b**). As expected from the trend found in previous studies on spin coated polymer films,[159,160] the skin thickness increased approximately linearly with the PVP concentration. We found a linear relationship between the PVP thickness and the resulting wrinkle wavelength, which indicates that increasing the PVP concentration only increased the film thickness while the Young's modulus was nearly constant (**Figure 4.2c**). Based on the slope of the line-of-best-fit, the moduli ratio of the PVP/PS composite (E_{PVP}/E_{PS}) could be determined by rearranging Equation 1.1:

$$E_{\mathrm{PVP}}/E_{\mathrm{PS}} \approx 3 \times \left[\frac{slope}{2\pi}\right]^3 \times \frac{1-v_{\mathrm{PVP}}^2}{1-v_{\mathrm{PS}}^2} \tag{4.1}$$

where v_{PVP} and v_{PS} are Poisson's ratios of PVP and PS. Because polystyrene is above its glass transition temperature during strain relief, v_{PS} is ~0.5.[161,162] By assuming that the Poisson's ratio of the PVP skin would be similar to those of PVP-based hydrogels (~0.5),[163,164] we estimated that $E_{PVP}/E_{PS} \approx 12$, which is similar to the CF_x/PS system ($E_{CFx}/E_{PS} \approx 13$).

4.2.3. Patterning Multigenerational Wrinkles

Using monolayer CVD graphene as a representative functional skin material, we could fabricate four-generation hierarchical wrinkles by sequential wrinkling with the sacrificial PVP skin (**Figure 4.3**). We first transferred graphene on a PS substrate coated with a fluoropolymer layer (~5 nm thickness) and relieved strain ($\varepsilon_1 \approx 0.3$) to create G1 wrinkles with wavelength $\lambda_1 \approx$ 50 nm. Then, three cycles of PVP-assisted patterning were performed. We progressively increased the concentration of PVP solution, and hence the skin thickness ($h_2 < h_3 < h_4$), to add larger-wavelength wrinkles on previous-generation features. For example, using 0.5 wt%, 2 wt%, and 10
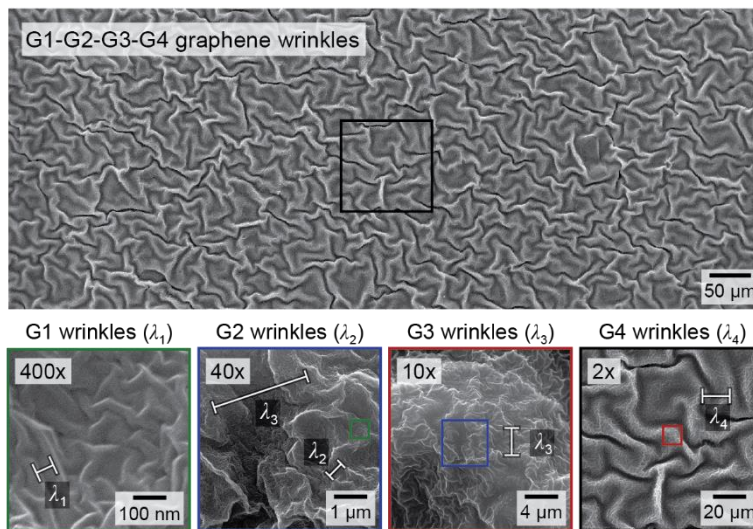
Figure 4.3. Out-of-plane hierarchical graphene wrinkles with four generational features. Characteristic wavelengths were $\lambda_1 \approx 50$ nm, $\lambda_2 \approx 700$ nm, $\lambda_3 \approx 3.5$ μm, and $\lambda_4 \approx 34$ μm.

wt% solutions for 2nd, 3rd, and 4th cycles, we produced generational features with $\lambda_2 \approx 700$ nm, $\lambda_3 \approx 3.5$ μm, and $\lambda_4 \approx 34$ μm in graphene (for $\varepsilon_2 \approx 0.3$; $\varepsilon_3 \approx 0.3$; $\varepsilon_4 \approx 0.3$). By comparing the wavelength of each G to the value expected for a single-generation wrinkles formed with the same PVP concentration (λ of 100 nm, 450 nm, and 1100 nm for PVP concentrations of 0.5 wt%, 2 wt%, and 10 wt%, respectively), we found that the wrinkle patterns functioned as an effective skin layer increased λ by 600, 680, and 2990% for 2nd, 3rd, and 4th cycles, respectively.

4.3. In-Plane Hierarchical Wrinkles with Variable Spatial Wavelengths

4.3.1. Overview of the Process

In *Section 3.6*, we demonstrated in-plane hierarchical graphene wrinkles by transferring graphene on CF_x layers patterned with different thicknesses. To introduce four distinct wrinkle wavelengths, two cycles of area-selective CF_x layer deposition and then unmasked CHF_3 plasma exposure were performed prior to graphene transfer and strain relief. Each spatially defined CF_x

growth involves formation of PVP patterns by embossing with a mold, CHF$_3$ plasma treatment, and lift-off of PVP, which would limit throughput of this wrinkling process. By solidifying PVP solution within a stamp patterned with different spatial heights and using the resulting PVP as a skin layer, we developed a facile strategy to produce in-plane hierarchical wrinkles.

Figure 4.4 depicts the fabrication process to create multiscale wrinkles with variable spatial wavelengths by patterning PVP skin layers based on molding. First, a functional skin material was transferred on a pre-strained PS sheet. PVP solution (PVP dissolved in ethanol) was then drop casted on the surface and pressed (~27.5 kPa) by a polymer stamp featuring locally different heights. After evaporating the solvent at an elevated temperature (65 °C for 30 minutes) and detaching the stamp, PVP skin layers with spatially defined thicknesses were formed. Because the wrinkle wavelength scales with the skin thickness, in-plane hierarchical wrinkles could result from strain relief with PVP patterns. Dissolving PVP with ethanol exposed the surface of functional material while the wrinkle topography was preserved.
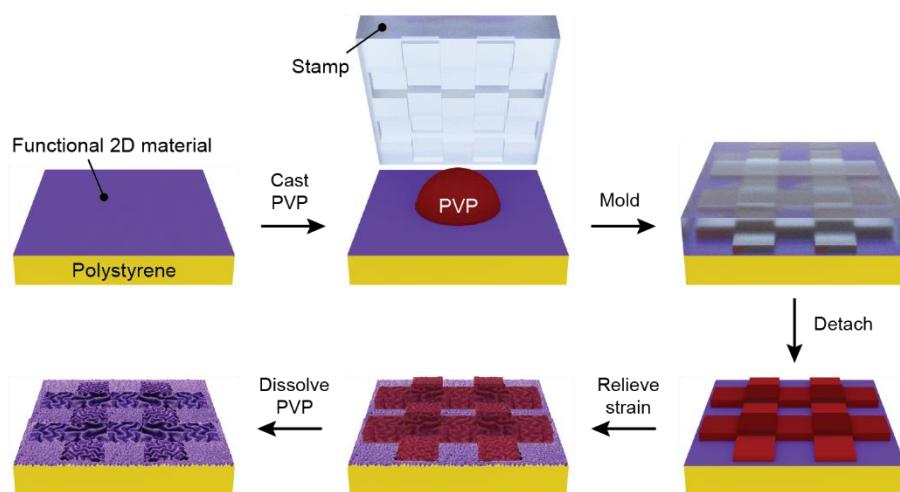
Figure 4.4. PVP-assisted wrinkling process for in-plane hierarchical texturing of functional skin materials.

4.3.2. Fabrication of Polymer Stamps for Patterning Sacrificial Skin Layers

We could design shape and dimensions of microdomains of the polymer stamp *via* the silicon master. For example, periodic line-shaped domains with two different heights could be formed by first patterning photoresist (PR) lines on a silicon substrate, depositing chromium (Cr) and lifting off the resist, and etching silicon (Si) with nm-scale tunable depth by reactive ion etching (RIE) in the areas not covered by the chromium mask (**Figure 4.5a**). After chromium etching, silicon masters with two distinct domains were formed. This process could then be repeated (PR patterning, Cr deposition and PR lift-off, RIE, and Cr etching) with the lines perpendicular to the initial patterns to produce four regions with different domain heights. **Figure 4.5b** shows a silicon
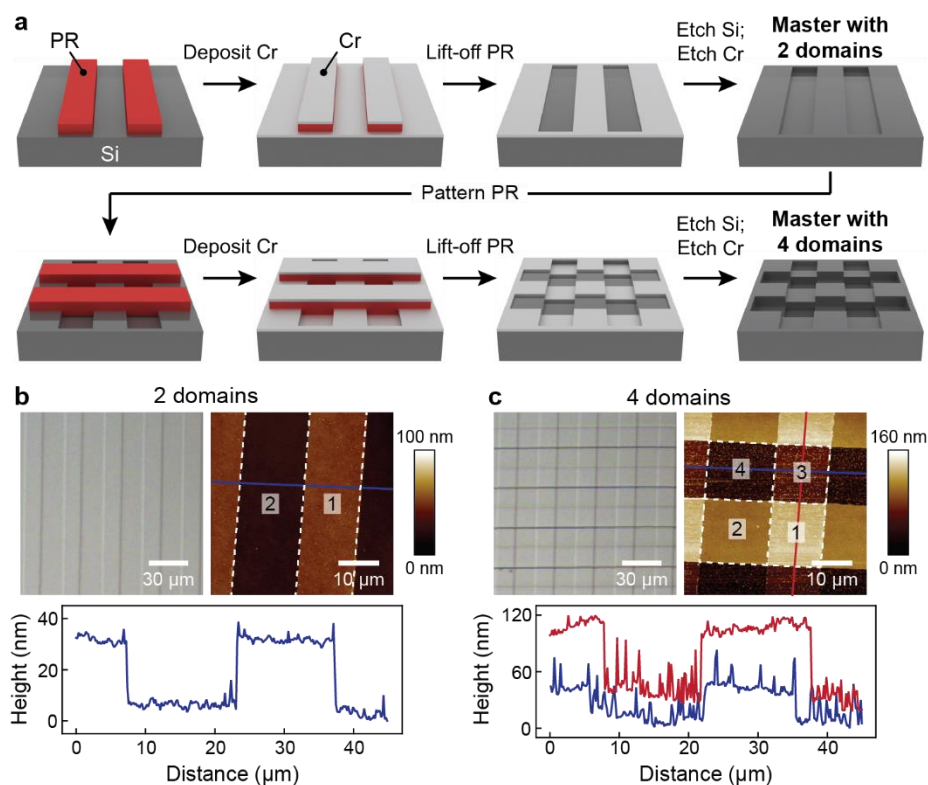
Figure 4.5. Silicon master for creating polymer stamps. (a) Scheme describing the fabrication process. Optical microscope and AFM images of silicon masters with **(b)** two and **(c)** four microdomains of different heights.

master with two distinct heights ($H_1 - H_2 \approx 30$ nm). Periodicity and width of the lines were $p = 30$ µm and $w = 15$ µm. By applying another cycle of area-selective Si etching (etch depth: ~80 nm) with lines perpendicular to each other, the surface can be patterned with four different local heights ($H_1 - H_2 \approx 30$ nm; $H_1 - H_3 \approx 80$ nm; $H_1 - H_4 \approx 110$ nm) (**Figure 4.5c**).

Stamps for patterning PVP skin layers were then produced by casting polymer against the master (**Figure 4.6a**). First, silicon patterns were replicated by a composite PDMS consisting of a thin, top layer (30-40 µm) of siloxane polymers with a relatively high modulus (~8.6 MPa) and a backing layer (~3 mm) of softer PDMS formulation (Sylgard 184, ~1.6 MPa). After curing at an elevated temperature (60 °C), the PDMS stamp was released from the master and used for fabricating a stamp made of an ultraviolet (UV)-curable fluoropolymer (UV-CF$_x$) with a higher modulus (~810 MPa). Because the UV-CF$_x$ was brittle, a poly(ethylene terephthalate) (PET) film
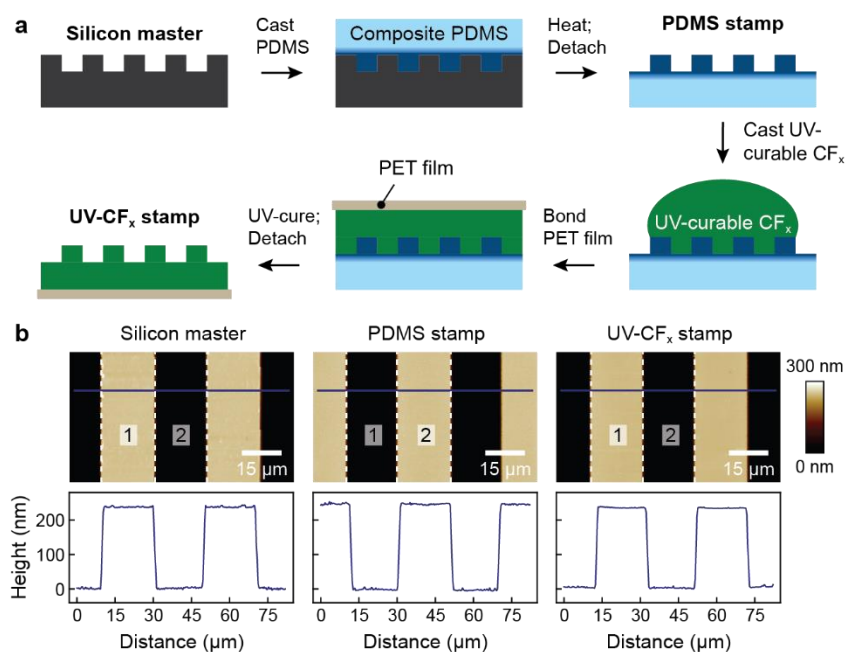
Figure 4.6. Polymer stamps replicating the master. **(a)** Schematic illustration of the molding process. **(b)** AFM images and heigh profiles of the line-patterned master ($p = 40$ µm, $w = 20$ µm, $\Delta H = 240$ nm) and polymer stamps.

(thickness of 175 µm) was used as a supporting layer for handling the stamp. **Figure 4.6b** compares heights of the line patterns on the master ($p = 40$ µm, $w = 20$ µm, $\Delta H = H_1 - H_2 = 240$ nm) and polymer replicas. Notably, the periodicity, width, and height of the lines for both PDMS and UV-CF_x stamps were nearly identical to those of the original features, which confirmed that replica molding could transfer patterns with a high fidelity. In the following sections, we examined the fidelity of PVP patterns created with line-patterned stamps made of composite PDMS and UV-CF_x.

4.3.3. *In-Plane Hierarchical Wrinkling by Solvent-Assisted Embossing*

We first tested solvent-assisted embossing with a PDMS stamp, which is widely used as one of the cost-effective, high-throughput soft lithography techniques to create nano- and microstructures.[165,166] First, the stamp was wetted with isopropyl alcohol (IPA) and placed on the PVP skin layer spin coated on the PS substrate. The solvent dissolved the PVP film and the resulting fluid conformed to the patterns. The stamp was in contact with the substrate until the PVP solidified after solvent evaporation and then detached. To investigate effects of the starting film thickness on the fidelity of patterns, we characterized surface topography of the features resulting from embossing PVP layers with different thicknesses (h_{PVP}).

Figure 4.7 shows PVP patterns formed by using a PDMS stamp with line trenches that are 5-µm in width and 500-nm in height ($p = 10$ µm, $w = 5$ µm, $\Delta H = 500$ nm). For a very thin PVP film ($h_{PVP} = 30$ nm), the embossed surface exhibited thin, line-shaped PVP residues (1-2 µm in width, < 200 nm in height) with a periodicity of 5 µm and isolated half cylinders with heights (400-440 nm) comparable to that of the stamp pattern, which suggests that the amount of PVP was not
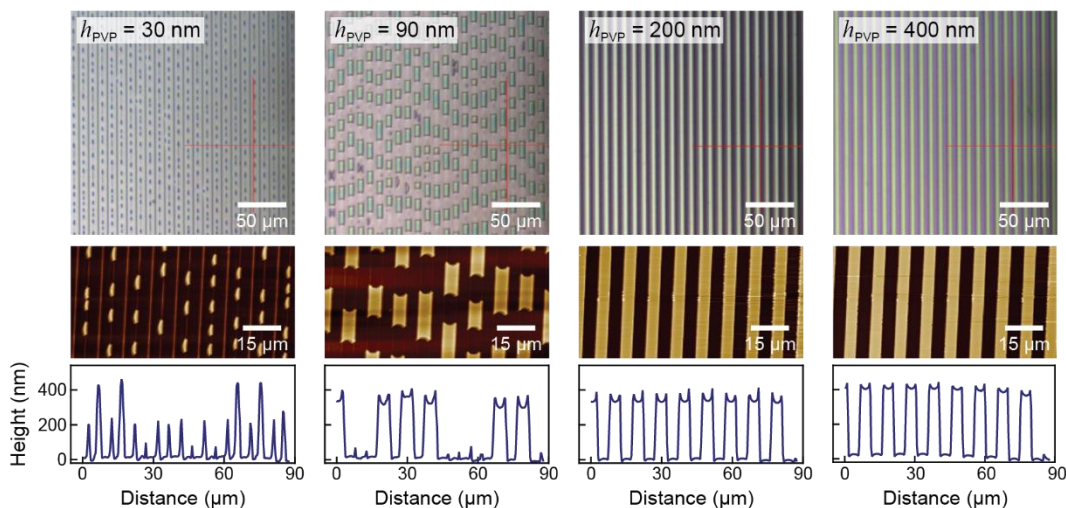
Figure 4.7. PVP patterns resulting from solvent-assisted embossing with a line-patterned PDMS stamp. Dimensions of the lines were $p = 10$ µm, $w = 5$ µm, $\Delta H = 500$ nm.

sufficient to fill the lines. As the starting PVP film became thicker ($h_{PVP} = 90$ nm), discontinuous lines formed after embossing. Complete filling of trenches was possible by further increasing the PVP skin thickness ($h_{PVP} > 200$ nm), but the resulting features exhibited recessed regions near the center might be because the top of the PDMS trenches deformed downward during solvent-assisted embossing. Moreover, residual PVP was observed in between lines. Transferring patterns into PVP
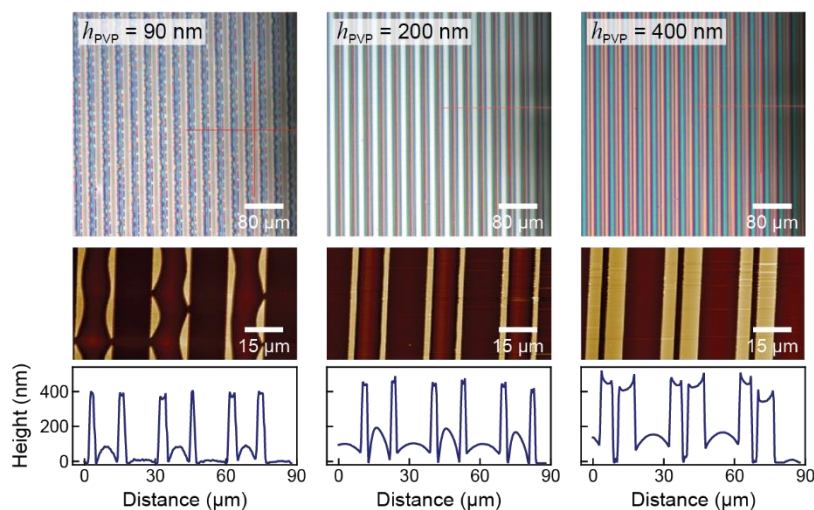
Figure 4.8. PVP patterns formed by embossing with a PDMS stamp with wider lines. Dimensions of the lines were $p = 30$ µm, $w = 15$ µm, $\Delta H = 500$ nm.

films was more challenging when the trenches became wider ($p = 30$ µm, $w = 15$ µm, $\Delta H = 500$ nm) (**Figure 4.8**). For all tested film thicknesses ($h_{PVP} = 90\text{-}400$ nm), PVP could not fill in the trenches to form continuous lines and residues were more pronounced compared to the case with the PDMS stamp with narrower trenches (Figure 4.7).

4.3.4. In-Plane Hierarchical Wrinkling by Molding

Molding is another commonly adopted fabrication strategy to produce nano- and microscale polymer features.[165-167] Based on the method described in *Section 4.3.1*, we compared PVP patterns formed with UV-CF$_x$ and PDMS stamps to investigate the effect of stamp material on the molding process. Because the surface energy is an important parameter related to the fidelity of soft lithography,[165] we first tested whether tuning of surface chemistry can result in improvements in molding. **Figure 4.9a** describes processes used to modify the surface of UV-CF$_x$. We focused on
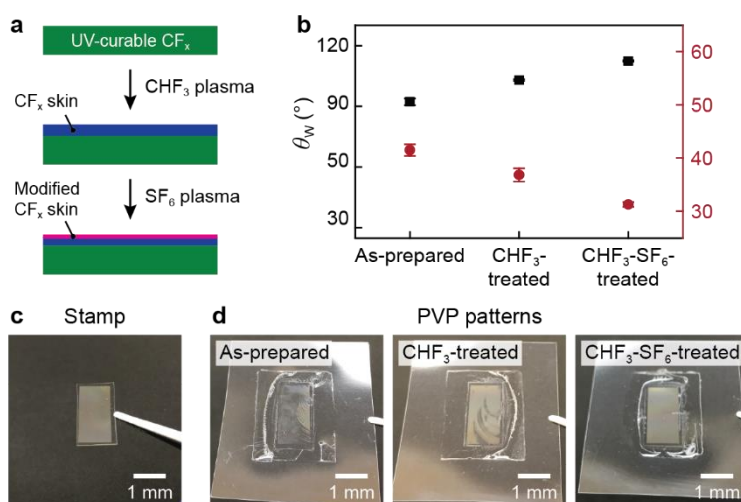
Figure 4.9. Effect of surface chemistry on molding process. (a) Scheme illustrating plasma treatments and the resulting surfaces. **(b)** Wetting characteristics of flat, functionalized UV-CF$_x$ surfaces. Optical images of **(c)** line-patterned UV-CF$_x$ stamp and **(d)** PVP patterns formed after molding. Dimensions of the lines were $p = 40$ µm, $w = 20$ µm, $\Delta H = 240$ nm.

fluorine-containing plasma treatments because they can reduce the surface energy and promote release of a stamp during peeling-off.[98,165] The as-prepared, flat UV-CF$_x$ showed contact angle (θ_W) and contact angle hysteresis (θ_H) of ~92° and ~42° (**Figure 4.9b**). After CHF$_3$ plasma treatment, the surface became more hydrophobic with θ_W ~ 103° and θ_H ~ 37° because of deposition of the plasma-mediated CF$_x$ layer. Further increase in hydrophobicity and hence reduction in surface energy was possible by applying SF$_6$ plasma (θ_W ~ 112° and θ_H ~ 31°), which partially etched the CF$_x$ layer and increased the fluorine content on the surface.[168] We then applied the same plasma processes to the line-patterned UV-CF$_x$ stamp ($p = 40$ µm, $w = 20$ µm, $\Delta H = 240$ nm) and compared PVP patterns resulting from molding the solution on PS substrates (**Figure 4.9c-d**). As we increased the hydrophobicity, we could increase the areas where the features are preserved after the stamp was detached; notably, PVP lines were intact over the entire area for the case of sequential CHF$_3$ and SF$_6$ plasma treatment, which highlights the importance of engineering surface chemistry for improving the fidelity of molding process.

We then compared the PVP patterns and the resulting hierarchical wrinkles formed with UV-CF$_x$ and PDMS stamps (lines with $p = 40$ µm, $w = 20$ µm, $\Delta H = 240$ nm) (**Figure 4.10a**). To deconvolute the effect of materials properties such as modulus on the fidelity of molding, we modified the surface of both stamps with the sequential CHF$_3$ and SF$_6$ plasma treatment. **Figure 4.10b** shows patterned PVP skin layers after molding the solution (~10 wt%) with the PDMS stamp. AFM topography images revealed that continuous lines could form with a height (ΔH ~200 nm) comparable to the original pattern. Similar to the case of thick PVP films ($h_{PVP} > 200$ nm) embossed with 5-µm wide trenches (Figure 4.7), PVP were recessed near the center regions of each line. We found that residual PVP layers were formed between line features (protrusions in
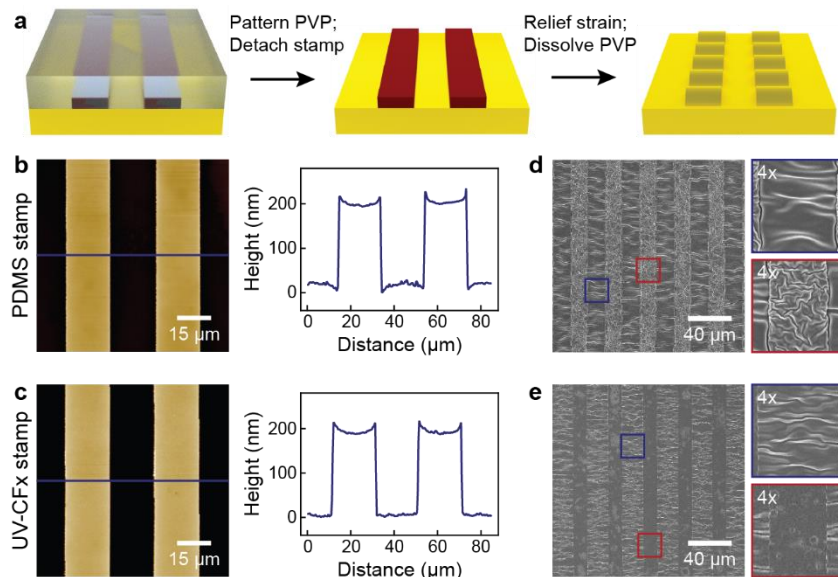
Figure 4.10. Side-by-side comparison patterns formed with UV-CF$_x$ and PDMS stamps.
(a) Process for creating PVP lines and wrinkles on polystyrene substrates. AFM topography images and height profiles of PVP lines molded with **(b)** PDMS and **(c)** UV-CF$_x$ stamps. SEM images of wrinkles resulting from patterned PVP skin layers for **(d)** PDMS and **(e)** UV-CF$_x$ stamps. Dimensions of the lines were $p = 40$ µm, $w = 20$ µm, $\Delta H = 240$ nm.

the AFM height profile) might be because PDMS deformed during molding.[169] In contrast, regions between lines were nearly flat when the solution was molded by the UV-CF$_x$ stamp although lines still exhibited a decreased height near the center (**Figure 4.10c**). Comparison between the PVP patterns suggests that preventing deformation of the stamp by using a material with a higher modulus was advantageous in creating microdomains of sacrificial skin layers. After molding, PS substrates were heated above its glass transition temperature to relief strain ($\varepsilon_{2D} \approx 0.4$), followed by rinsing of PVP to expose the wrinkled PS surface (**Figure 4.10d-e**). Wrinkles in the microdomains were uniaxially aligned because strain perpendicular to the lines were relieved by the domain boundaries. The PDMS stamp resulted in wrinkles between the domains because of the residual PVP layers (Figure 4.10d). Notably, wrinkles fabricated with the UV-CF$_x$ stamp exhibited significantly reduced residual features between the microdomains (Figure 4.10e).

4.3.5. Multiscale Wrinkling of Functional Skin Materials

To investigate the versatility of our approach, we tested multiscale structuring of monolayer graphene and 20-nm thick gold films (**Figure 4.11**). PVP solution was patterned with a stamp exhibiting square domains (p = 30 µm, w = 15 µm) with four different local heights ($H_1 - H_2 \approx 30$ nm; $H_1 - H_3 \approx 80$ nm; $H_1 - H_4 \approx 110$ nm). Notably, we could create wrinkles with four distinct wavelengths for graphene ($\lambda_1 \approx 570$ nm, $\lambda_2 \approx 1$ µm, $\lambda_3 \approx 1.4$ µm, and $\lambda_4 \approx 3$ µm) and gold ($\lambda_1 \approx 650$ nm, $\lambda_2 \approx 1.5$ µm, $\lambda_3 \approx 1.9$ µm, and $\lambda_4 \approx 4$ µm) skin layers, which highlights the generality of our method. The observed wavelengths, however, were much larger than the expected values, which suggests that the fidelity of PVP patterning process still needs to be improved. We expect that further optimization of PVP concentration and surface tension of the solution would transfer patterns without loss in height from the stamp while preventing residues.
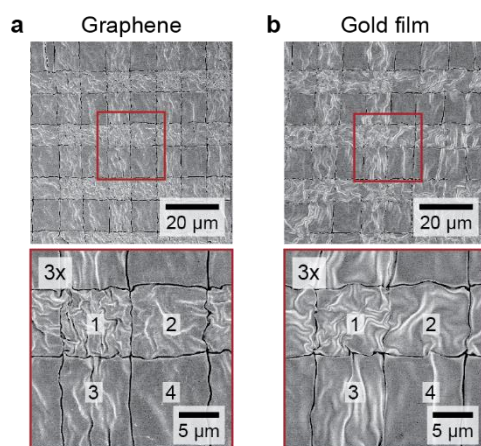
Figure 4.11. In-plane hierarchical wrinkles with variable wavelengths patterned on functional skin materials. (a) Graphene and **(c)** gold film with four distinct wrinkle wavelengths side-by-side.

4.4. **Methods**

4.4.1. *Preparation of Polyvinylpyrrolidone (PVP) Solution and Skin Layers*

Polyvinylpyrrolidone (PVP) solution was prepared by dissolving PVP powders (Sigma Aldrich, average molecular weight = 40,000 g/mol) in ethanol. Solution was bath sonicated for 1 hour to fully dissolve the polymer. PVP films with a globally uniform thickness were created by spin coating the solution at 4000 rpm on polystyrene (PS) sheets, followed by heating at 80 °C for 5 minutes to remove residual ethanol. For patterned PVP skin layers, solution was applied on the substrate and molded with the polymer stamp until the solvent evaporates.

4.4.2. *Wrinkle Fabrication and Characterization*

PVP-coated PS substrates were shrunk to a desired size by heating the samples at 135 °C in a convection oven. Biaxially strain (ε_{2D}) was determined based on the change in the area before and after shrinking: $\varepsilon_{2D} = (A_0 - A)/A_0$, where A_0 and A are initial and final areas. After strain relief, PVP skin layers were removed from the substrate by rinsing the surface with ethanol. Samples were then coated with a ~10 nm AuPd conductive film (Desk III TSC sputter coater, Denton Vacuum) and characterized with a scanning electron microscope (SEM) (S-4800 Type II, Hitachi). The reported wrinkle wavelength corresponds to the main wavevector in 2D fast Fourier transform of the SEM image.[65] Surface topography information was obtained by tapping-mode atomic force microscopy (AFM) (Dimension ICON, Bruker).

4.4.3. *Ellipsometry Measurements of the Polyvinylpyrrolidone Skin Thickness*

The thicknesses of the PVP skin layers were determined by spectroscopic ellipsometry (M-

2000, J. A. Woollam Co.) of PVP-coated polystyrene sheets at different angles (from 45 to 65° in 5° increments) over wavelengths of 250-1000 nm. Scotch tape (3M) was attached to the backside of the samples to avoid reflection from the back surface. The measured ellipsometry constants (Ψ and Δ) were fitted to a skin-substrate Cauchy model to determine the skin thickness. Each data point and error bar represent the average and standard deviation from three measurements.

4.4.4. Silicon Master Fabrication

Masters were fabricated by photolithography. First, silicon wafers were coated with MCC Primer 80/20 (MicroChem Corp.) to improve adhesion between the substrate and photoresist. A positive-tone photoresist (Shipley S1805, MicroChem Corp.) diluted with propylene glycol monomethyl ether acetate (1:2 volume ratio) was then spin coated at 4000 rpm for 40 s to produce films with a thickness of 130 nm, followed by baking at 115°C for 2 min. After patterning the photoresist with a maskless photolithography instrument (µPG 501 Maskless Aligner, Heidelberg Instruments), samples were immersed in a potassium-based buffered developer (AZ400K, AZ Electronic Materials) diluted with deionized water (1:4 volume ratio). To form an etch mask for dry etching of silicon, a thin chromium film (~10 nm) was deposited by thermal evaporation, followed by lift-off of photoresist using Microposit Remover 1165 (MicroChem Corp.). Samples were then treated with a reactive ion etching (RIE) process with a mixture of gases (SF_6, CF_4, and O_2 at flow rates of 10, 40, and 10 sccm, respectively, with a power and a pressure of 2 Pa and 30 W) to etch silicon in the areas not protected by the chromium mask. Chromium was removed from the surface after RIE using a chromium etchant (Chromium etchant 1020, Transene Co.). The silicon patterning process was repeated to increase the number of distinct domains with different

local heights.

4.4.5. Fabrication of Composite Polydimethylsiloxane Stamp

Composite polydimethylsiloxane (PDMS) stamps were created by mixing degassed vinyl PDMS prepolymer (3.4 g, (7.0–8.0% vinylmethylsiloxane)-dimethylsiloxane copolymer, VDT-731, Gelest, Inc.), 10 mL of a Pt catalyst (platinum-divinyltetramethyldisiloxane, SIP6831.2, Gelest, Inc.), one drop of a modulator (2,4,6,8- tetramethyl-2,4,6,8-tetravinylcyclotetrasiloxane, 396281, Sigma-Aldrich, delivered from a 19 G, 1.5 inch, thin-wall needle), and 1 g of a hydrosilane prepolymer ((25–30% methylhydrosiloxane)-dimethylsiloxane copolymer, HMS-301, Gelest, Inc.). The vinyl and hydrosilane end-linked PDMS was spin-coated onto the silicon master (1000 rpm, 40 s) to produce a thin film (thickness of 30–40 μm) and cured for 30 min at 60 °C. Afterwards, an uncured layer of Sylgard 184 PDMS (mixture of base polymer and curing agent at 10:1 mass ratio, Dow Corning) was poured onto the thin, patterned PDMS layer to a height of 3 mm and then cured for 2 hours at 60 °C. After cooling to room temperature, the composite PDMS stamp was carefully peeled off from the master.

4.4.6. Fabrication of Ultraviolet-Curable Fluoropolymer Stamp

Ultraviolet-curable fluoropolymer (UV-CF$_x$) stamps were prepared by drop casting a liquid prepolymer (FluroAcryl 3298, Cytonix) on a 175-μm thick poly(ethylene terephthalate) (PET) sheet (Sigma Aldrich), followed by molding with the composite PDMS stamp. The PET surface was treated with an oxygen plasma before molding to improve adhesion with the UV-CF$_x$. After exposing the prepolymer to ultraviolet light for 10 minutes, the stamp was released from the PDMS

patterns.

4.4.7. Solvent-Assisted Embossing of Polyvinylpyrrolidone Films

The composite PDMS was first immersed in isopropyl alcohol (IPA) for 90 s to wet the surface with solvent. Patterned side of the stamp was then brought into contact with the PVP film spin coated on the PS sheet. After embossing the PVP with IPA and evaporating the solvent at room temperature for 45 minutes, the stamp was detached from the surface.

4.4.8. Patterning of Polyvinylpyrrolidone Skin Layers by Molding

PVP solution was drop casted on the PS film and molded with either PDMS or UV-CFx stamp. Pressure (~27.5 kPa) was applied to improve conformal contact between the stamp and the substrate. The stamp was peeled off after evaporating the solvent at 65 °C for 30 minutes and then cooling the sample to room temperature to minimize deformation of the PVP patterns.

4.5. **Summary and Outlook**

In summary, we developed a scalable, high throughput manufacturing tool to create in-plane and out-of-plane hierarchical wrinkles using solution processible polymer skin layers. With control over the sacrificial skin thickness both in global and local areas of the substrate, we could design surface textures with programmable structural hierarchy and feature sizes at multiple length scales. As the process is general across different skin materials, we expect that our strategy will be beneficial in engineering properties of various 2D materials.

Chapter 5

Functional Surfaces from Hierarchical Wrinkles

Hierarchical structures consisting of nano- and microscale topographic features exhibit physical and chemical properties that are challenging to realize with single-scale patterns. This chapter demonstrates that characteristic feature sizes and orientations of multigenerational soft wrinkles can be designed to engineer various properties without using conventional multistep lithography techniques. By comparing functional responses of wrinkles with different numbers of generational features side-by-side, we revealed that multiscale hierarchical wrinkles are advantageous for potential applications in water harvesting surfaces and antibacterial fouling coatings. The patterns can be transferred into other functional materials *via* embossing or molding to enhance their properties such as photoluminescence.

Related publication:

D. Rhee, C. Machado, M.-K. Kim, Y.-S. Kim, N. Miljkovic, K.-C. Park, T.W. Odom, "Superhydrophobic Hierarchical Wrinkles Supporting Spatially Defined Water Condensation," In preparation

5.1. **Introduction**

Creating topographic patterns on the surface of materials enables tuning of physical and chemical properties of the system.[170-172] Design of these structures at multiple length scales is important because micro- and nanostructures tailor different functional responses. Microscale patterns commonly introduce mechanical flexibility and stretchability,[57,173] while nanoscale features can result in antifogging and light trapping properties.[174,175] Hierarchical architectures that combine these two can realize additional functions that are difficult to achieve by single-scale textures. For example, a lotus leaf is superhydrophobic with water-repelling properties because micropapillae (bump-like features, ~10 μm in size) covered by nanoscale tubules (200-300 nm in diameter) support air pockets between water and the surface.[176] Also, Gecko foot exhibits lamellae (400–600 μm in size) decorated with arrays of setae (~4 μm in diameter, ~120 μm in length) that branches into 100-1000 spatulae (~100 nm in diameter, ~800 nm in length) at the tip, which offers strong adhesion of Gecko on various surfaces.[177] Bio-inspired 3D hierarchical structures have been fabricated to mimic properties of natural systems or even realize unprecedented functions, but complex lithographic processes with multiple steps of masking and etching were needed.[178-181]

In this chapter, we focused on creating functional surfaces based on hierarchical wrinkles that spontaneously form upon sequential cycles of skin layer formation and strain relief of the substrate. Characteristic feature sizes and orientations could be tuned at both nano- and microscale by controlling the skin thickness and strain relief direction for each cycle. The resulting hierarchical structures exhibited properties that cannot be achieved by single-generation textures such as enhanced water condensation by coalescence-induced jumping and reduced bacterial attachment and biofilm formation. Moreover, the patterns could be transferred into other materials to enhance

properties; for example, quantum dots films embossed with nanowrinkles showed an increase in photoluminescence intensity compared to the flat counterpart.

5.2. **Superhydrophobic Surfaces with Enhanced Water condensation**

Controlling modes of water condensation is critical for applications such as condensers and water harvesting platform, and self-cleaning surfaces.[174,182-184] For example, superhydrophobic surfaces enable jumping of condensates upon their coalescence and support subsequent condensate nucleation, which lead to enhancement in heat transfer coefficient and self-cleaning efficiency. [182,184] To achieve jumping-droplet condensation, surface patterns need to be designed to preserve air pockets between the substrate and micron-size droplets and minimize adhesion forces.[174,182,185] Meeting this criterion, however, is challenging because condensates tend to nucleate within the grooves of nanostructures and remain pinned during growth. Sub-300 nm features with high aspect ratio (>5) are typically needed, which is difficult to achieve by wrinkling-based patterning strategy (aspect ratio is less than 1). In this Section, we demonstrate that hierarchical wrinkles on fluorinated polystyrene substrates can promote droplet jumping during condensation with careful design of wavelength at each generation.

5.2.1. *Design of Hierarchical Wrinkles for Jumping Droplet Condensation*

To identify the effect of structural hierarchy on water condensation, we fabricated wrinkles with different numbers of generational features based on sequential cycles of fluoropolymer (CF_x) skin growth followed by strain relief of a thermoplastic polystyrene (PS) sheet (**Figure 5.1a**).[70] First, a pre-strained PS substrate was treated with the CHF_3 plasma to form the first skin layer (h_1).
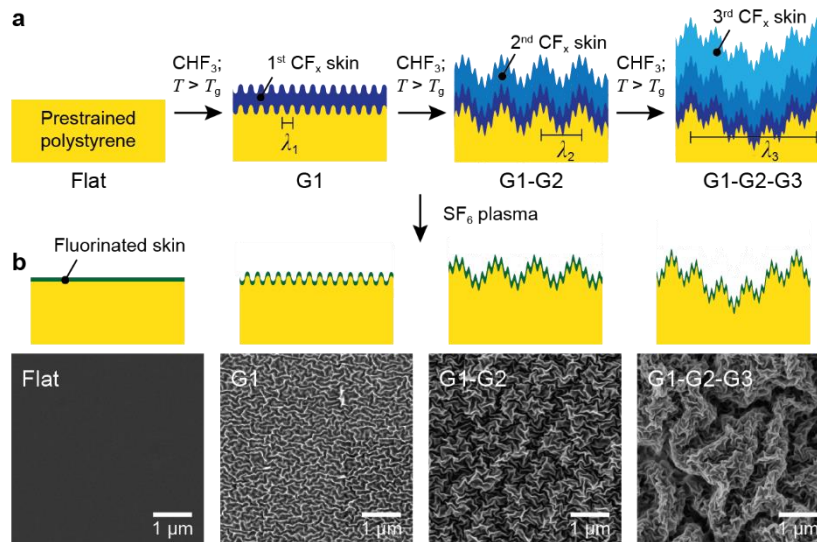
Figure 5.1. Multiscale hierarchical wrinkles for water condensation. (a) Scheme describing fabrication process. **(b)** SEM images of wrinkles with different structural hierarchy.

After relieving the strain (ε_1) by heating the system above the glass transition temperature of PS ($T_g = 100$ °C), G1 wrinkles with the smallest wavelength (λ_1) were created. G2 wrinkles with a larger wavelength (λ_2) were formed by depositing the second CHF$_3$ plasma followed by a second strain relief (ε_2) upon subsequent heating at a temperature higher than T_g. The process was repeated to achieve wrinkles up to three generations. After wrinkle formation, the surface was treated with SF$_6$ plasma to enhance hydrophobicity.[98,168] Because sub-300 nm nanostructures are critical for supporting jumping-droplet-enhanced condensation, we started from creating nanowrinkles with a comparable wavelength. We kept h_1, h_2, and h_3 fixed at 10, 20, and 60 nm, and ε_1, ε_2, and ε_3 at ca. 0.4, 0.4, and 0.5, which generated G1-G2-G3 wrinkles with $\lambda_1 \approx 150$ nm, $\lambda_2 \approx 750$ nm, and $\lambda_3 \approx 3.5$ μm on the PS surface (**Figure 5.1b**). Aspect ratio of the features were ~0.5.

Figure 5.2 shows *in-situ* optical microscope images of condensing droplets on wrinkles with different hierarchical architectures at different times. The wavelengths for the first (G1), second (G2), and third (G3) generation wrinkles of each sample were fixed to be $\lambda_1 \approx 150$ nm, $\lambda_2 \approx 750$

nm, and $\lambda_3 \approx 3.5$ μm. Under a supersaturated condition (supersaturation of $S = 1.4$ at a surface temperature of 7 °C), condensates initially nucleated on the surface and grew to micron-sized, spherical droplets. At later stages of condensation, droplets became larger in size and started to merge. The coalesced droplets on flat substrates and G1 wrinkles showed deviation from the spherical geometry (**Figure 5.2a-b**) because condensates were strongly pinned on the surface. In contrast, G1-G2 patterns exhibited spherical droplets even after multiple times of coalescence, which suggests that droplets could be de-pinned from the valleys of G1 features with the presence of the larger-scale topography (**Figure 5.2c**). Adding a third generation of wrinkles further reduced adhesion forces and achieved droplet removal *via* coalescence-induced jumping (**Figure 5.2d**).
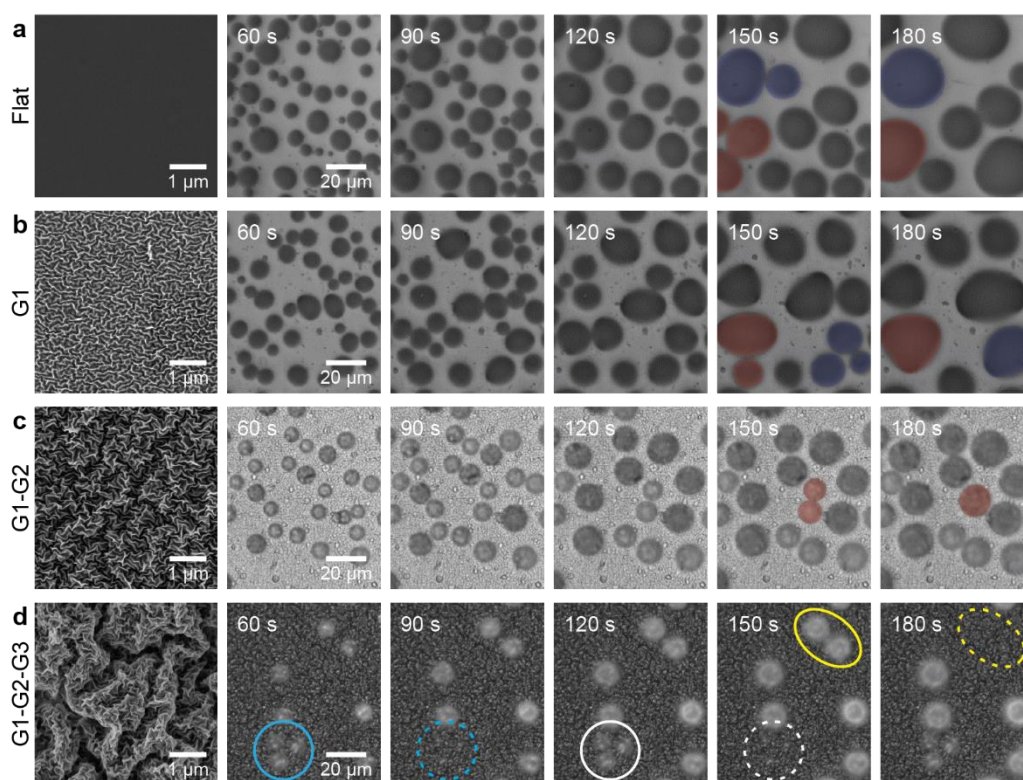
Figure 5.2. Role of structural hierarchy on water condensation. SEM images (column 1) and time-lapse optical images during water condensation (columns 2-6) for **(a)** flat surface, **(b)** G1 wrinkles ($\lambda_1 \approx 150$ nm), **(c)** G1-G2 wrinkles ($\lambda_1 \approx 150$ nm, $\lambda_2 \approx 750$ nm), and **(d)** G1-G2-G3 wrinkles ($\lambda_1 \approx 150$ nm, $\lambda_2 \approx 750$ nm, $\lambda_3 \approx 3.5$ μm). Droplets before and after coalescence events are highlighted.

We then examined whether feature sizes are important for droplet jumping besides the generational hierarchy by comparing condensation on G1-G2-G3 hierarchical wrinkles with different wavelengths (**Figure 5.3**). All the tested surfaces were superhydrophobic with contact angles > 160° and contact angle hysteresis < 5° based on the static contact angle measurement with 100 nL droplets (~580 µm in diameter). When the wavelengths of the first two generations were smaller than a micrometer and the third-generation wavelength was less than 50% of the droplet diameter before coalescence ($\lambda_1 \approx 150$ nm, $\lambda_2 \approx 750$ nm, $\lambda_3 \approx 3.5$ µm), the patterned substrate supported the jumping-droplet condensation mode (**Figure 5.3a**). On hierarchical wrinkles with a roughly two times larger wavelength for each generation ($\lambda_1 \approx 300$ nm, $\lambda_2 \approx 1.5$ µm, $\lambda_3 \approx 6.5$ µm), droplets could not jump from the surface upon coalescence although no noticeable pinning was observed (**Figure 5.3b**). When we increased the wrinkle wavelengths further ($\lambda_1 \approx 300$ nm, $\lambda_2 \approx$
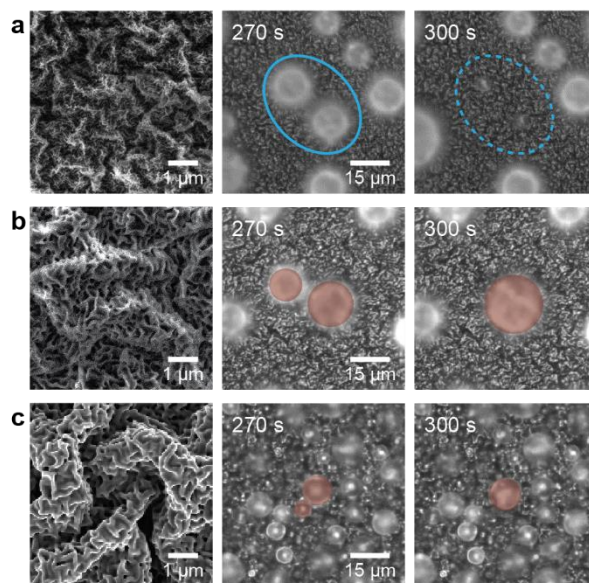
Figure 5.3. Importance of length scale to achieve self-propelled droplet jumping. SEM images (column 1) and time-lapse optical images during water condensation (columns 2-3) for G1-G2-G3 wrinkles with **(a)** $\lambda_1 \approx 150$ nm, $\lambda_2 \approx 750$ nm, $\lambda_3 \approx 3.5$ µm; **(b)** $\lambda_1 \approx 300$ nm, $\lambda_2 \approx 1.5$ µm, $\lambda_3 \approx 6.5$ µm; and **(c)** $\lambda_1 \approx 300$ nm, $\lambda_2 \approx 2.5$ µm, $\lambda_3 \approx 12$ µm. Droplets before and after coalescence events are highlighted.

2.5 µm, $\lambda_3 \approx 12$ µm), droplets were mostly trapped within the valleys of third-generation wrinkles during condensation and hence coalescence was greatly suppressed (**Figure 5.3c**). This side-by-side comparison indicates that both the structural hierarchy and the feature sizes are critical for controlling water condensation mechanisms.

5.2.2. *Metasurfaces of Hydrophilic Microposts and Hierarchical Wrinkles*

Nano- and micro-patterns with significant contrast in surface chemistry and topography are useful for applications in water harvesting surfaces and condensers.[186] For example, the introduction of hydrophilic patches on superhydrophobic surfaces allows for enhanced water condensate nucleation while preserving water shedding properties of superhydrophobic regions. [186,187] A scalable fabrication tool with controlled feature sizes and spacing is important for creating an optimal pattern for a target functionality. Based on the sequential wrinkling processes, we developed a method to create metasurfaces composed of periodic posts embedded in 3D hierarchical wrinkles over centimeter-scale areas.

Figure 5.4a describes how the metasurfaces can be achieved. First, we fabricated post arrays by depositing metals through a hole array film on a pre-strained PS sheet followed by lift-off of the mask. Multigenerational, hierarchical wrinkles were then generated by applying sequential cycles of CF_x skin layer formation and strain relief depicted in *Section 5.2.1*. After the wrinkle formation, CF_x layers were selectively etched by SF_6 plasma treatment to expose the metal surface. **Figure 5.4b** shows a representative metasurface, which were fabricated by depositing chromium (30 nm in thickness) through a square array of micro-holes with a periodicity p_0 and applying three cycles of sequential wrinkling. Because the PS substrate isotopically shrank during strain relief,
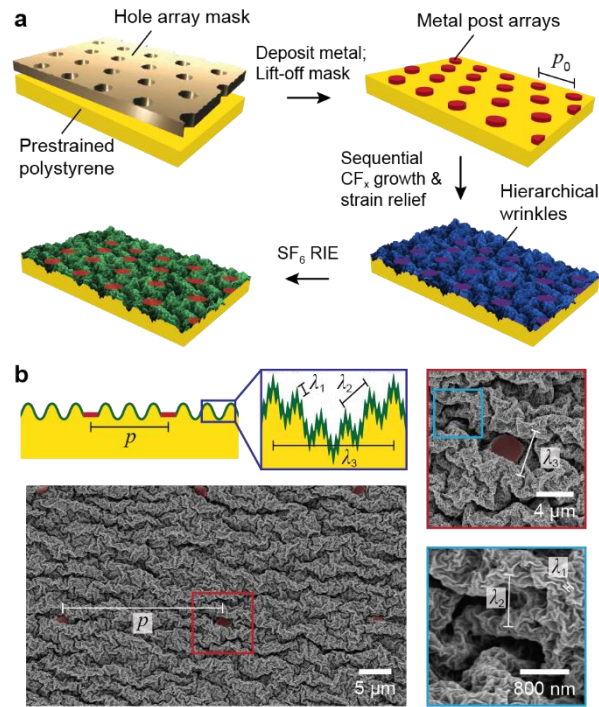
Figure 5.4. Metasurfaces consisting of micropost arrays and hierarchical wrinkles. (a) Scheme describing the fabrication process. **(b)** SEM images of the metasurfaces.

the metasurface was characterized by a square array of chromium posts with a spacing (p) smaller than p_0. The chromium microdomains were surrounded by G1-G2-G3 hierarchical wrinkles with characteristic wavelengths λ_1, λ_2, and λ_3.

To identify the design rules to program structural features of the metasurfaces, we investigated relations between starting post dimensions and the resulting patterns. For sequential wrinkling, we focused on the same processing parameters (h_1, h_2, and h_3 fixed at 10, 20, and 60 nm, and ε_1, ε_2, and ε_3 at ca. 0.4, 0.4, and 0.5) that resulted in G1-G2-G3 wrinkles supporting coalescence-induced droplet jumping in *Section 5.2.1*. **Figure 5.5** highlights how our method can independently control the structural parameters of chromium post arrays and hierarchical wrinkles. First, the spacing between posts were tuned by the periodicity of hole arrays in the mask used for chromium deposition (**Figure 5.5a**). For example, we obtained metasurfaces with inter-post spacings of ca.

25 and 12 μm from hole array masks with $p_0 = 50$ μm and $p_0 = 25$ μm, respectively. The observed periodicities were only slightly larger than the expected values based on the assumption that the entire surface of the substrate uniformly shrank on both chromium and PS regions (ca. 24 μm and 11 μm for $p_0 = 50$ μm and $p_0 = 25$ μm, respectively). In addition, we found that wrinkled domains exhibited characteristic wavelengths ($\lambda_1 \approx 150$ nm, $\lambda_2 \approx 750$ nm, and $\lambda_3 \approx 3.5$ μm) similar to those of G1-G2-G3 hierarchical wrinkles without chromium posts (Figure 5.5a, left SEM image), which indicates that our process enables precise design of both post arrays and wrinkle topography. Besides the inter-post spacing, the post diameter could also be engineered through the deposition mask. **Figure 5.5b** shows SEM images of metasurfaces formed with hole arrays with different diameters at a fixed periodicity ($p_0 \approx 50$ μm). We discovered that patterns with programmable post geometries were possible because of two key characteristics of our approach: (1) the chromium posts showed nearly identical diameters to those of holes since compressive strain was mostly accommodated by the PS domains, and (2) the inter-post spacing ($p \approx 25$ μm) did not depend on the post diameter.
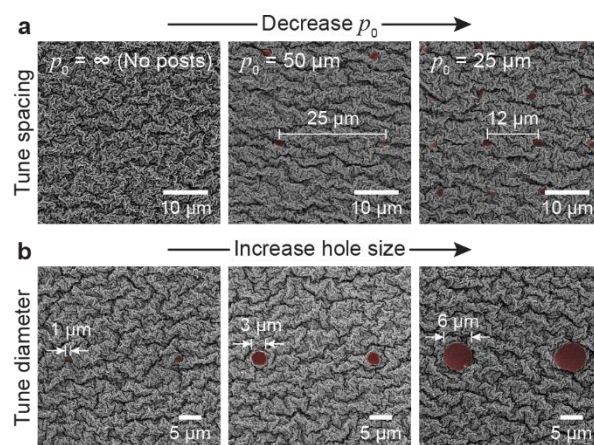
Figure 5.5. Independent tuning of post dimensions and wrinkle topography. SEM images of surfaces with different **(a)** post spacings and **(b)** diameters.

5.2.3. *Jumping-Droplet-Enhanced Condensation on Biphilic Hierarchical Wrinkles*

Biphilic surfaces consisting of hydrophilic microarrays surrounded by superhydrophobic nanotextures show enhanced performance in water harvesting and dehumidification applications when compared to purely hydrophilic or superhydrophobic platforms.[186,187] In humid air, hydrophilic domains promote nucleation of condensates while superhydrophobic areas shed grown droplets and allow for subsequent nucleation events. Most efforts have focused on creating hydrophilic micropatterns protruding on top of nanostructured substrates.[187-189] These systems, however, show limitations because condensed droplets are pinned on the hydrophilic domains during the droplet shedding, thus blocking the areas available for nucleating new condensates. Moreover, repelling water from the surface is also difficult when mm-droplets are externally deposited from the top, such as in rainfall.

To address these challenges, we developed biphilic surfaces with hydrophilic chromium microposts embedded in out-of-plane three-generational wrinkles (G1-G2-G3 wrinkles exhibiting $\lambda_1 \approx 150$ nm, $\lambda_2 \approx 750$ nm, and $\lambda_3 \approx 3.5$ μm with post arrays of $p \approx 20$ μm and d ≈ 2 μm) (**Figure 5.6a**). For contact angle measurements with 3-μL water droplets (~1.8 mm in diameter), the biphilic surfaces exhibited superhydrophobicity with a contact angle larger than 160° and a contact angle hysteresis less than 1° (**Figure 5.6b**). We validated the importance of the three-tier
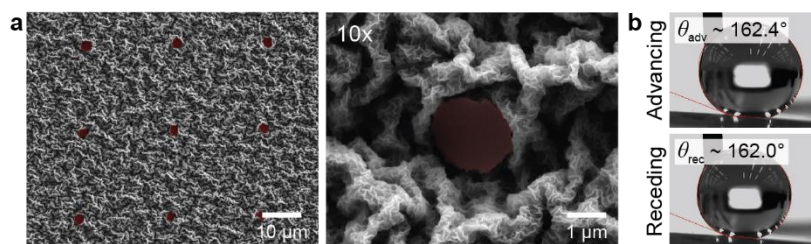
Figure 5.6. Superhydrophobic metasurfaces consisting of hydrophilic post arrays and hierarchical wrinkles. (a) SEM images of the surfaces. (b) Water contact angles.

hierarchical wrinkles by examining static wetting characteristics of metasurfaces with different number of structural hierarchies (**Figure 5.7**). For comparison, we fabricated G1 ($\lambda_1 \approx 150$ nm), G1-G2 ($\lambda_1 \approx 150$ nm and $\lambda_2 \approx 750$ nm), and G1-G2-G3 ($\lambda_1 \approx 150$ nm, $\lambda_2 \approx 750$ nm, and $\lambda_3 \approx 3.5$ μm) wrinkles with a fixed post dimension ($p \approx 20$ μm and d ≈ 2 μm) (**Figure 5.7a-c**) The presence of hydrophilic micropost arrays decreased hydrophobicity of the G1 and G1-G2 wrinkles (**Figure 5.7d-e**), which were characterized by decreased θ_W and increased θ_H compared to surfaces patterned only with wrinkles, while G1-G2-G3 wrinkles exhibited nearly identical wetting properties regardless of the posts. Although θ_W and θ_H values were similar for G1-G2 and G1-G2-
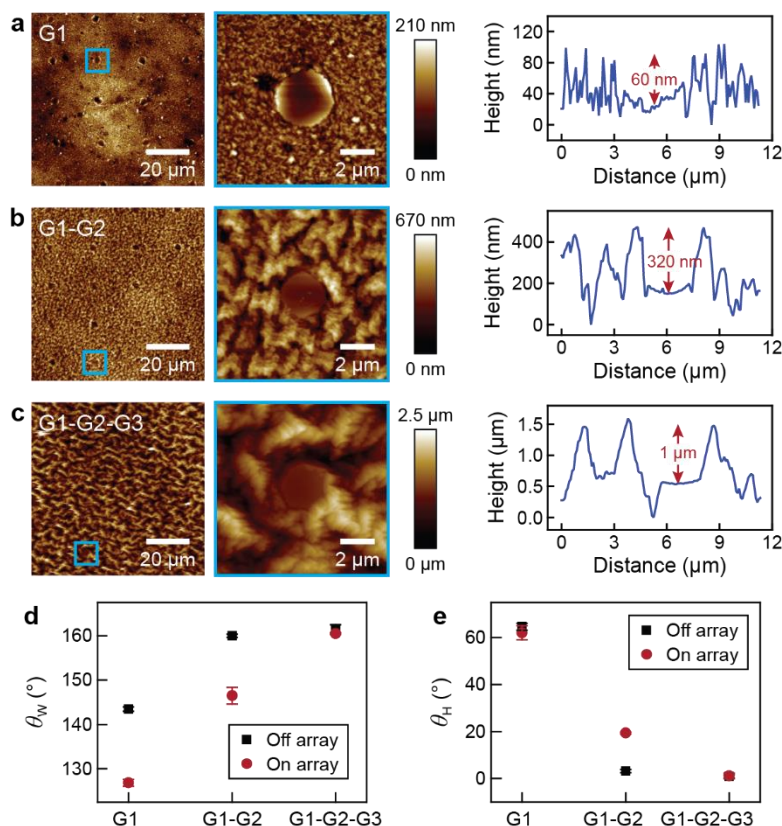
Figure 5.7. Role of structural hierarchy in wetting properties of metasurfaces. AFM topography images and height profiles of **(a)** G1, **(b)** G1-G2, and **(c)** G1-G2-G3 wrinkles integrated with microposts (p ≈ 20 μm, d ≈ 2 μm). **(d)** Static water contact angle and **(e)** contact angle hysteresis measured on metasurfaces with different hierarchical wrinkles.

G3 wrinkles without posts, only the metasurface based on G1-G2-G3 structures maintained superhydrophobicity, which highlights that G3 features with a microscale amplitude were necessary to prevent mm-sized droplets from accessing the hydrophilic domains.

We then characterized water condensation process on the biphilic hierarchical wrinkles using *in-situ* optical imaging in a humidity chamber setup (**Figure 5.8**). Significantly, water vapor selectively condensed on the hydrophilic posts where the thermodynamic energy barrier for nucleation is smaller compared to superhydrophobic regions. As condensates grew to the size comparable to the inter-post spacing, coalescence events started to occur. Because of the low adhesion forces between water droplets and G1-G2-G3 wrinkles, merged droplets could be depinned from the posts and roll off (1 → 1') or removed from the surface via coalescence-induced jumping (2 → 2' and 3 → 3'). After the droplet shedding, microposts supported subsequent nucleation and growth of condensates to collect more water. In future works, we plan to investigate optimal post spacing and diameter to increase the area density of nucleation sites while preserving water repelling properties of G1-G2-G3 wrinkles.
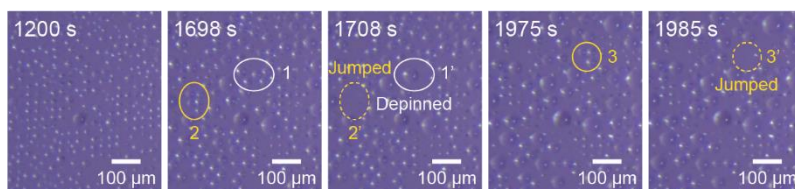
Figure 5.8. Biphilic hierarchical wrinkles for enhanced condensation. Time-lapse optical images during water condensation.

5.3. **Antibacterial Fouling Surfaces**

Fouling of surfaces by bacteria are detrimental to industrial and medical settings.[190-192] In the early stage of bacterial fouling, bacterial cells attach to a surface.[193] As the attached bacteria grow in number by division and more cells accumulate from the environment, microcolonies (aggregates of < 50 cells) are formed.[194] Further growth of cell population result in maturation of microcolonies into biofilms, where bacterial cells are surrounded by an extracellular polysaccharide matrix and become resistant to antimicrobial treatments and host immune responses.[193,195,196] Most efforts to reduce bacterial fouling have relied on the antimicrobials and chemical coatings to prevent the initial attachment of bacterial cells.[197-199] However, bacteria can mask the underlying chemical functionalities by secreting surfactants onto the surface and eventually form biofilms. Nano- and micropatterned surfaces can thus provide an alternative approach to hinder microbial colonization;[200-203] however, effects of topographical features are not yet fully understood. By designing PS wrinkles of different wavelengths and structural hierarchies, we investigated systematically the effects of surface topography in deterring initial colonization and subsequent biofilm formation.

We examined antibacterial fouling properties of wrinkled surfaces against a pathogenic bacterial strain, *Staphylococcus aureus* (*S. aureus*; Gram-positive, sphere-shaped bacteria that are 0.5-1.2 μm in diameter),[192] dispersed in liquid growth media. Three types of 1D wrinkles were fabricated using CF_x layers on PS substrates: (1) wrinkles with a wavelength smaller than the cell diameter ($\lambda \approx 300$ nm), (2) wrinkles larger than the cell ($\lambda \approx 3$ μm), and (3) hierarchical wrinkles consisting of the two characteristic features ($\lambda_1 \approx 300$ nm; $\lambda_2 \approx 3$ μm) (**Figure 5.9**). We also tested a flat CF_x surface as a control.
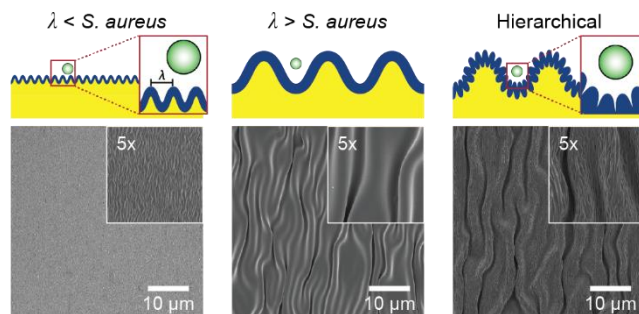
Figure 5.9. Design of hierarchical wrinkles for antibacterial fouling surface.

Figure 5.10a shows the attachment of *S. aureus* on the surfaces at an early stage of fouling (2 hours). We observed reduction in bacterial adhesion on wrinkles compared to the flat surface for all the structural parameters tested. When the wrinkle wavelength was smaller than the cell diameter ($\lambda \approx 300$ nm), only the peaks could be accessed by *S. aureus*. Such reduction in available surface area led to a decreased bacterial attachment. On surfaces with a larger wrinkle wavelength ($\lambda \approx 3$ μm), cells adhered preferentially to the valleys of the wrinkles. We found that the smaller wrinkles were more beneficial in hindering initial colonization. Interestingly, hierarchical wrinkles that combine both features ($\lambda_1 \approx 300$ nm; $\lambda_2 \approx 3$ μm) exhibited a similar degree of anti-biofouling
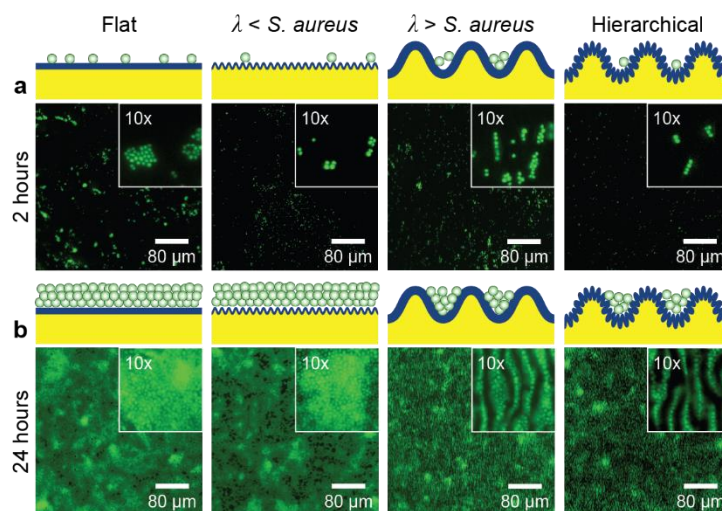
Figure 5.10. Anti-biofouling properties of multi-scale, hierarchical wrinkles. Fluorescence microscope images of the attached *S. aureus* after **(a)** 2 hours and **(b)** 24 hours of incubation.

properties to the smaller features. After 24 hours of growth, the flat surface was fully covered with biofilms (**Figure 5.10b**). At this time point, nanowrinkles with $\lambda \approx 300$ nm could not effectively prevent bacterial fouling. Notably, wrinkles with a wavelength larger than the cell diameter (both for single- and two-generation wrinkles) could serve as a physical barrier to impede expansion of bacterial colonies and hence prevent massive fouling.

To clarify the role of wrinkles in reducing bacterial fouling, we quantified the number of bacteria by dispersing the attached cells using sonication, incubating the dispersion on agar plates, and counting the number of colonies after incubation (**Figure 5.11**). The trend in the direct quantification was consistent with the image analysis (Figure 5.10): at 2 hours, nanowrinkles (1.6×10^6 cells/cm^2; 50% reduction) exhibited higher reduction in the number of attached cells than microscale wrinkles (2.2×10^6 cells/cm^2; 33% reduction) compared to the flat surface (3.3×10^6 cells/cm^2) (**Figure 5.11a**), while the microscale wrinkles (2.0×10^7 cells/cm^2; 47% reduction) were beneficial than both nanowrinkles (3.8×10^7 cells/cm^2; no reduction) and flat CF$_x$ (3.8×10^7 cells/cm^2) after 24 hours of incubation (**Figure 5.11b**). Hierarchical wrinkles showed the least
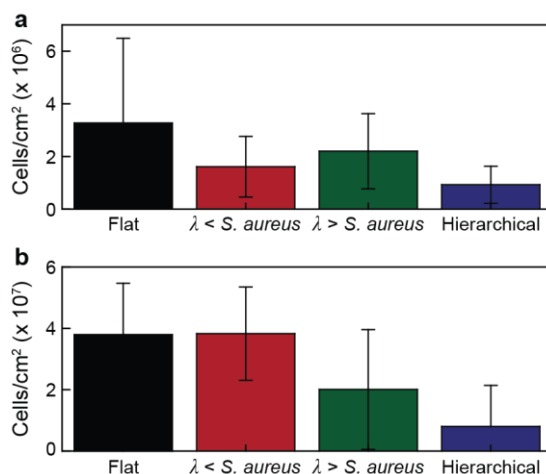
Figure 5.11. Quantification of bacterial fouling on multi-scale, hierarchical wrinkles.
Densities of the attached *S. aureus* after **(a)** 2 hours and **(b)** 24 hours of incubation.

cells at both 2 hours (9.2×10^5 cells/cm^2; 72% reduction) and 24 hours (8.0×10^6 cells/cm^2; 79% reduction). In future works, we will investigate the time course of bacterial colonization to identify more clearly the effect of wrinkle topography in preventing bacterial fouling at different stages.

5.4. **Quasi-Random Nanostructures for Controlling Light-Matter Interactions**

Quasi-random nanostructures that are neither perfectly periodic nor fully disordered have received interest in photonic applications such as such as solar cells and light-emitting diodes, and structural color coatings.[204-206] These patterns support rich Fourier spectra and thus can manipulate light over a broad range of wavelengths and over wide collection angles.[204] To design optical response of patterns, independent control over the relative degree of order and disorder, materials filling ratio, and feature size is crucial.[175] Although serial processes such as electron-beam lithography enable precise control over the nanoscale structures, the tools are not scalable and are cost-prohibitive for large-area fabrication (>1 cm^2).[204,207,208] To address this challenge, we developed a facile method to create soft lithography stamps that can be used to pattern luminescent films with programmable quasi-random structures.

5.4.1. *Soft Lithography Stamps with Tunable Quasi-Periodicity*

Figure 5.12a depicts the process for producing soft lithography stamp patterned with quasi-random nanostructures. First, we created a wrinkle-patterned master by depositing chromium films on PDMS substrates. A PDMS slab attached to a glass slide was loaded into a thermal evaporator, followed by chromium deposition. Because heat from the metal source expanded the PDMS substrate, compressive strain was generated upon cooling the system to room temperature and thus
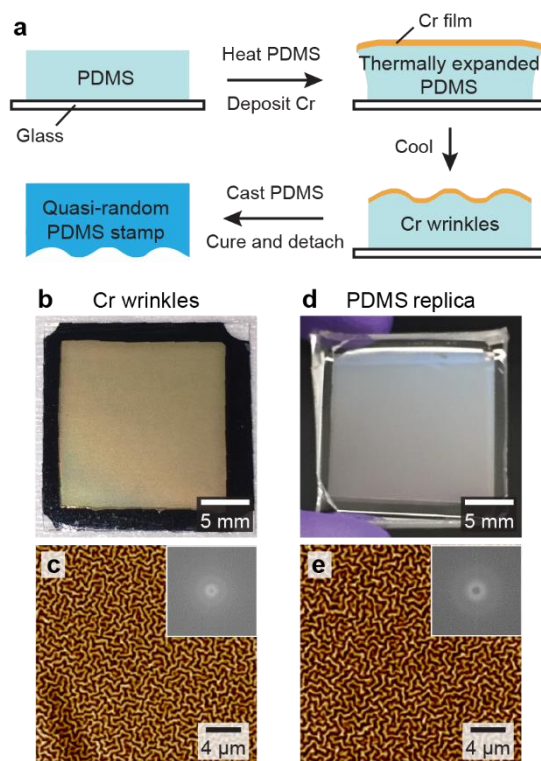
Figure 5.12. Quasi-random nanostructures from heat-induced wrinkling of chromium films on PDMS. (a) Schematic illustration of the fabrication process. Chromium wrinkles under **(b)** optical and **(c)** AFM topography images. PDMS replica under **(d)** optical and **(e)** AFM topography images. Insets in panels c and e shows 2D FFT of the AFM images.

wrinkles were formed in the chromium film.[28] The resulting surface exhibited a uniform patterns over centi-meter scale areas (~4 cm^2) (**Figure 5.12b**) and the wrinkles were characterized by a quasi-periodicity (wrinkle wavelength, $\lambda \approx 530$ nm) without a preferred orientation (**Figure 5.12c**)., which was confirmed by a radially symmetric ring feature in the 2D fast Fourier transform (FFT) image (Figure 5.12c, inset). We then replicated the textures into composite PDMS that could be used as a stamp to pattern luminescent materials. The patterns were transferred uniformly over the whole centimeter scale area (**Figure 5.12d**) with the same quasi-periodicity with the master (**Figure 5.12e**). The amplitude of the wrinkles in the PDMS replica ($A = 68$ nm) was only ~28% smaller than that of the original pattern ($A = 94$ nm).
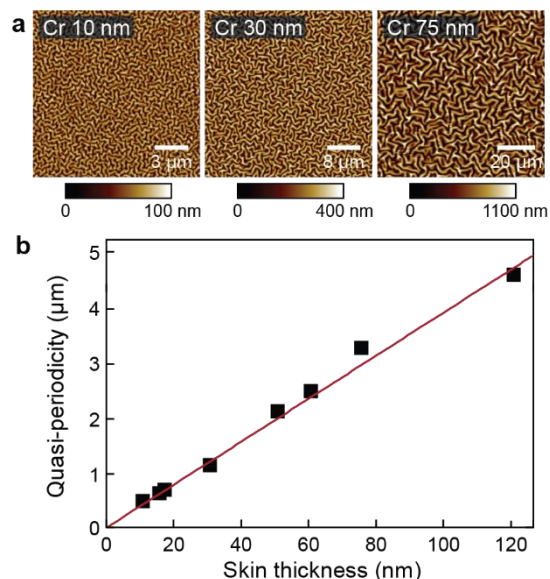
Figure 5.13. Tunability in quasi-periodicity. (a) AFM image of wrinkles formed with different chromium thicknesses. **(b)** The relation between the chromium thickness and quasi-periodicity.

To test the tunability of our wrinkle system, we characterized the quasi-periodicity of wrinkles (wrinkle wavelength, λ) for different chromium thicknesses (**Figure 5.13a**). By simply changing the thickness of the chromium film from 10 nm to 120 nm, we obtained wrinkles with quasi-periodicities from 420 nm to 4.5 µm, which covers the visible spectrum and near infrared range (**Figure 5.13b**).

5.4.2. Enhanced Photoluminescence from Patterned Perovskite and Quantum Dot

Thin films of luminescent materials are useful for optoelectronic applications such as displays and light emitting diodes.[209-211] One drawback for high-efficiency luminescence is that the emitted light is partially trapped within the film *via* total internal reflection.[212,213] To address this issue, previous work has introduced surface textures to increase the fraction of light that can be extracted from the film.[213,214] In particular, quasi-random nanostructures can enable light outcoupling over

broadband from visible to near infrared ranges, which are not possible with fully periodic or disordered geometries.[205] Based on the quasi-random soft lithography stamp, we present a simple and scalable method to pattern customizable quasi-random structures into photoluminescent films for enhanced light emission. As a demonstration, we tested photoluminescence (PL) enhancement of CdSe-CdS quantum dot (QD) films that exhibit an emission peak at 633 nm and a refractive index of $n \sim 1.92$. To increase light outcoupling, we focused on textures with quasi-periodicity of 570 nm that is similar to the PL maximum of QD films. After spin coating a QD film on a glass substrate, we transferred wrinkle patterns into the film *via* solvent-assisted nanoscale embossing using dimethylformamide (**Figure 5.14a**). Significantly, wrinkles in QD films exhibited the same quasi-periodicity with the PDMS mold ($\lambda = 570$ nm), although the wrinkle amplitude ($A = 30$ nm) was smaller compared to the original pattern ($A = 70$ nm). The patterned QD film showed ca. 3.5-fold increase in PL intensity compared to the flat counterpart (**Figure 5.14b**). As a next step, we plan to investigate how we can design the quasi-periodicity and amplitude of QD wrinkles for
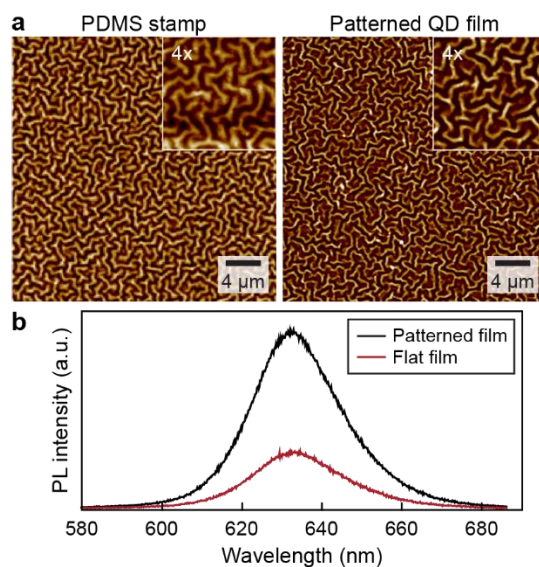
Figure 5.14. Quasi-random nanostructures for enhancing photoluminescence of quantum dot films. (a) AFM images of quasi-random features on the PDMS stamp and QD film. **(b)** PL spectra from flat and patterned QD films.

optimal light extraction and PL enhancement. Then, we will expand our strategy to engineer light-emitting properties of other luminescent materials, such as organic-inorganic hybrid perovskites and organic semiconductors.

5.5. **Methods**

5.5.1. *Polystyrene Wrinkle Fabrication and Characterization*

Pre-strained PS substrates were first exposed to CHF_3 plasma to form fluoropolymer skin layers in a reactive ion etching (RIE) chamber (RIE-10NR, Samco Inc.) at a flow rate of 25 sccm and a power of 70 W under a pressure of 20 Pa. After plasma treatment, samples were heated at 135 °C in a convection oven until a desired size was achieved. For 2D wrinkles, the substrate was allowed to shrink isotopically, while 1D wrinkles were produced by clamping two opposite sides of the substrate. We determined biaxially strain (ε_{2D}) from the change in the area before and after shrinking: $\varepsilon_{2D} = (A_0 - A)/A_0$, where A_0 and A are initial and final areas. Uniaxial strain (ε_{1D}) was calculated based on the change in length of the sample before and after strain relief: $\varepsilon_{1D} = (L_0 - L)/L_0$, where L_0 and L are initial and final lengths. Skin growth and strain relief processes were repeated until the desired structural hierarchy was achieved. The wavelength of wrinkles was determined from scanning electron microscope (SEM) (S-4800 Type II, Hitachi) images of samples coated with a ~10 nm AuPd conductive film (Desk III TSC sputter coater, Denton Vacuum). The reported values correspond to the main wavevectors in 2D fast Fourier transform of the SEM images.[65] Topography information was obtained by tapping-mode atomic force microscopy (AFM) (Dimension ICON, Bruker).

5.5.2. *Fabrication of Micropost Arrays*

The array fabrication started by producing hole-array masks using photolithography, gold deposition, and lift-off. Similar to the procedure used for creating silicon masters in *Section 4.4.4*, a photoresist film on a silicon wafer was first patterned with a maskless photolithography instrument (μPG 501 Maskless Aligner, Heidelberg Instruments), followed by development in a potassium-based buffered developer (AZ400K, AZ Electronic Materials) diluted with deionized water (1:4 volume ratio). After depositing a thin chromium film (~10 nm) and lifting off the photoresist, silicon was etched by a RIE treatment (a mixture of SF_6, CF_4, and O_2 gases at flow rates of 10, 40, and 10 sccm, respectively, with a power and a pressure of 2 Pa and 30 W) to create pits. The mask with hole arrays were then produced by depositing gold using a thermal evaporator (~200 nm). Wet etching of the chromium layer (Chromium etchant 1020, Transene Co.) released the hole-array mask from the silicon, which was transferred onto a PS substrate. After chromium deposition (~30 nm) and peeling-off of the mask using an adhesive tape, micropost arrays were created on the surface.

5.5.3. *Condensation Experiment*

Wrinkled polystyrene substrates were mounted on a cold stage (Instec, TP104SC-mK2000A) and cooled to a target temperature of 7 °C at a cooling rate of 10 K/min. Temperature and relative humidity of the ambient air were 24 °C and 48.5%. Images were recorded using a high-speed camera (Phantom, V711, Vision Research) attached to an optical microscope (Eclipse LV100, Nikon) with a 50x objective lens.

5.5.4. *Bacterial Culture*

A frozen stock of *Staphylococcus aureus* (*S. aureus*, ATCC 6538) was added to liquid growth media (tryptic soy broth, TSB) and incubated for 18-24 hours on an orbital shaker rotating at 200 rpm. To obtain bacterial cells in the growth phase, the overnight culture was diluted with a fresh TSB solution (1:100). After 4 hours of incubation at 200 rpm, the subculture was diluted to a starting cell concentration of ~4×10^7 cells/mL. The bacterial suspension was applied to the samples mounted on the bottom of six well plates and incubated statically at 37 °C for 2-24 hours. After the culture, surfaces were rinsed by dipping samples into sterile 1x phosphate buffered saline (PBS) three times to remove cells not attached on the surface.

5.5.5. *Characterization of Bacterial Fouling*

To visualize bacterial fouling, the adherent bacteria were fixed by immersing samples in 4% paraformaldehyde for 20 minutes, followed by rinsing with PBS 2 times to remove residual paraformaldehyde from the surface. Cells were then labeled with SYTO 9 green nucleic acid stain (Invitrogen) and mounted on a cover glass slide for fluorescence optical microscope imaging (Leica DM6B Fluorescent Microscope). For quantification, samples were bath sonicated to disperse attached cells in PBS. The bacterial dispersion was then serially diluted and incubated on agar plates. After incubation at 37 °C for 24 hours, colonies were counted. The reported cell densities were calculated based on the number of colonies, volume of the original dispersion, dilution factor, and area of the fouled sample.

5.5.6. *Fabrication of PDMS Stamp Patterned with Quasi-Random Nanostructures*

A PDMS slab (2×2 cm^2) was attached to a glass slide and then loaded into a thermal evaporator for chromium deposition. During the deposition process, heat from the metal source caused expansion of the PDMS substrate. When the sample cooled to a room temperature and return to the initial dimension, the chromium film was compressed and formed wrinkles spontaneously.

5.5.7. *Photoluminescence Measurement*

Photoluminescence (PL) spectra were measured using a confocal Raman microscopy (LabRAM HR Evolution, Horiba) under a 532-nm laser excitation. The excitation power was kept below 1mW to avoid damage to MoS$_2$. PL from samples was collected with an Olympus 100x objective and dispersed by a diffraction grating (600 lines/mm). Focal spot size and depth resolution were approximately 1 µm.

5.6. **Summary and Outlook**

In summary, we engineered structural hierarchy of spontaneously formed wrinkle patterns for tuning functional responses such as water condensation characteristics, antibacterial fouling properties, and photoluminescence. We revealed that combining nano- and microscale features into hierarchical architectures is crucial for realizing unprecedented properties. With the capability to produce near unlimited combinations of wrinkle wavelengths and orientations and to transfer the patterns into other materials, we expect that our platform will be beneficial for designing various functional systems.

REFERENCES

1. Sidorenko, A.; Krupenkin, T.; Taylor, A.; Fratzl, P.; Aizenberg, J., Reversible Switching of Hydrogel-Actuated Nanostructures into Complex Micropatterns. *Science* **2007,** *315*, 487.

2. Grinthal, A.; Aizenberg, J., Adaptive All the Way Down: Building Responsive Materials from Hierarchies of Chemomechanical Feedback. *Chem. Soc. Rev.* **2013,** *42*, 7072-7085.

3. Zarzar, L. D.; Aizenberg, J., Stimuli-Responsive Chemomechanical Actuation: A Hybrid Materials Approach. *Acc. Chem. Res.* **2013,** *47*, 530-539.

4. Kim, P.; Zarzar, L.; Khan, M.; Aizenberg, M.; Aizenberg, J., Environmentally Responsive Active Optics Based on Hydrogel-Actuated Deformable Mirror Arrays. *Proc. SPIE* **2011,** *7927*, 792705.

5. Zarzar, L. D.; Kim, P.; Aizenberg, J., Bio-Inspired Design of Submerged Hydrogel-Actuated Polymer Microstructures Operating in Response to pH. *Adv. Mater.* **2011,** *23*, 1442-1446.

6. He, X.; Aizenberg, M.; Kuksenok, O.; Zarzar, L. D.; Shastri, A.; Balazs, A. C.; Aizenberg, J., Synthetic Homeostatic Materials with Chemo-Mechano-Chemical Self-Regulation. *Nature* **2012,** *487*, 214-218.

7. Kim, J.; Yoon, J.; Hayward, R. C., Dynamic Display of Biomolecular Patterns Through an Elastic Creasing Instability of Stimuli-Responsive Hydrogels. *Nature Materials* **2010,** *9*, 159-164.

8. Kim, P.; Zarzar, L. D.; Zhao, X.; Sidorenko, A.; Aizenberg, J., Microbristle in Gels: Toward All-Polymer Reconfigurable Hybrid Surfaces. *Soft Matter* **2010,** *6*, 750-755.

9. Quan, Y.-J.; Kim, Y.-G.; Kim, M.-S.; Min, S.-H.; Ahn, S.-H., Stretchable Biaxial and Shear Strain Sensors Using Diffractive Structural Colors. *ACS Nano* **2020,** *14*, 5392-5399.

10. Baik, S.; Kim, D. W.; Park, Y.; Lee, T.-J.; Bhang, S. H.; Pang, C., A Wet-Tolerant Adhesive Patch Inspired by Protuberances in Suction Cups of Octopi. *Nature* **2017,** *546*, 396-400.

11. Hu, B.; Berkey, C.; Feliciano, T.; Chen, X.; Li, Z.; Chen, C.; Amini, S.; Nai, M. H.; Lei, Q.-L.; Ni, R.; Wang, J.; Leow, W. R.; Pan, S.; Li, Y.-Q.; Cai, P.; Miserez, A.; Li, S.; Lim, C. T.; Wu, Y.-L.; Odom, T. W., et al., Thermal-Disrupting Interface Mitigates Intercellular Cohesion Loss for Accurate Topical Antibacterial Therapy. *Adv. Mater.* **2020,** *32*, 1907030.

12. Lee, S. G.; Lee, D. Y.; Lim, H. S.; Lee, D. H.; Lee, S.; Cho, K., Switchable Transparency and Wetting of Elastomeric Smart Windows. *Adv. Mater.* **2010,** *22*, 5013-5017.

13. Lee, G. H.; Choi, T. M.; Kim, B.; Han, S. H.; Lee, J. M.; Kim, S.-H., Chameleon-Inspired Mechanochromic Photonic Films Composed of Non-Close-Packed Colloidal Arrays. *ACS Nano* **2017,** *11*, 11350-11357.

14. Wang, Q.; Zhao, X., A Three-Dimensional Phase Diagram of Growth-Induced Surface Instabilities. *Sci. Rep.* **2015,** *5*, 8887.

15. Genzer, J.; Groenewold, J., Soft Matter with Hard Skin: From Skin Wrinkles to Templating and Material Characterization. *Soft Matter* **2006,** *2*, 310-323.

16. Rodríguez-Hernández, J., Wrinkled Interfaces: Taking Advantage of Surface Instabilities to Pattern Polymer Surfaces. *Prog. Polym. Sci.* **2015,** *42*, 1-41.

17. Yang, S.; Khare, K.; Lin, P. C., Harnessing Surface Wrinkle Patterns in Soft Matter. *Adv. Func. Mater.* **2010,** *20*, 2550-2564.

18. Taylor, J. M.; Argyropoulos, C.; Morin, S. A., Soft Surfaces for the Reversible Control of Thin-Film Microstructure and Optical Reflectance. *Adv. Mater.* **2016,** *28*, 2595-2600.

19. Chiche, A.; Stafford, C. M.; Cabral, J. T., Complex Micropatterning of Periodic Structures on Elastomeric Surfaces. *Soft Matter* **2008,** *4*, 2360-2364.

20. Jiang, H.; Khang, D.-Y.; Song, J.; Sun, Y.; Huang, Y.; Rogers, J. A., Finite Deformation Mechanics in Buckled Thin Films on Compliant Supports. *Proc. Natl. Acad. Sci. U. S. A.* **2007,** *104*, 15607-15612.

21. Brau, F.; Vandeparre, H.; Sabbah, A.; Poulard, C.; Boudaoud, A.; Damman, P., Multiple-Length-Scale Elastic Instability Mimics Parametric Resonance of Nonlinear Oscillators. *Nat. Phys.* **2011,** *7*, 56-60.

22. Lin, P.-C.; Yang, S., Spontaneous Formation of One-Dimensional Ripples in Transit to Highly Ordered Two-Dimensional Herringbone Structures Through Sequential and Unequal Biaxial Mechanical Stretching. *Appl. Phys. Lett.* **2007,** *90*, 241903.

23. Kim, P.; Hu, Y.; Alvarenga, J.; Kolle, M.; Suo, Z.; Aizenberg, J., Rational Design of Mechano-Responsive Optical Materials by Fine Tuning the Evolution of Strain-Dependent Wrinkling Patterns. *Adv. Opt. Mater.* **2013,** *1*, 381-388.

24. Lin, P.-C.; Vajpayee, S.; Jagota, A.; Hui, C.-Y.; Yang, S., Mechanically Tunable Dry Adhesive from Wrinkled Elastomers. *Soft Matter* **2008,** *4*, 1830-1835.

25. Graz, I. M.; Cotton, D. P. J.; Lacour, S. P., Extended Cyclic Uniaxial Loading of Stretchable Gold Thin-Films on Elastomeric Substrates. *Appl. Phys. Lett.* **2009,** *94*, 071902.

26. Zhang, Q.; Tang, Y.; Hajfathalian, M.; Chen, C.; Turner, K. T.; Dikin, D. A.; Lin, G.; Yin, J., Spontaneous Periodic Delamination of Thin Films To Form Crack-Free Metal and Silicon Ribbons with High Stretchability. *ACS Appl. Mater. Interfaces* **2017,** *9*, 44938-44947.

27. Cordill, M. J.; Taylor, A.; Schalko, J.; Dehm, G., Fracture and Delamination of Chromium Thin Films on Polymer Substrates. *Metall. Mater. Trans. A* **2010,** *41*, 870-875.

28. Bowden, N.; Brittain, S.; Evans, A. G.; Hutchinson, J. W.; Whitesides, G. M., Spontaneous Formation of Ordered Structures in Thin Films of Metals Supported on an Elastomeric Polymer. *Nature* **1998,** *393*, 146-149.

29. Tang, J.; Guo, H.; Chen, M.; Yang, J.; Tsoukalas, D.; Zhang, B.; Liu, J.; Xue, C.; Zhang, W., Wrinkled Ag Nanostructured Gratings Towards Single Molecule Detection by

Ultrahigh Surface Raman Scattering Enhancement. *Sens. Actuators B Chem.* **2015,** *218*, 145-151.

30. Bowden, N.; Huck, W. T. S.; Paul, K. E.; Whitesides, G. M., The Controlled Formation of Ordered, Sinusoidal Structures by Plasma Oxidation of an Elastomeric Polymer. *Appl. Phys. Lett.* **1999,** *75*, 2557.

31. Douville, N. J.; Li, Z.; Takayama, S.; Thouless, M., Fracture of Metal Coated Elastomers. *Soft Matter* **2011,** *7*, 6493-6500.

32. Lee, Y. T.; Lee, J. M.; Kim, Y. J.; Joe, J. H.; Lee, W., Hydrogen Gas Sensing Properties of PdO Thin Films with Nano-Sized Cracks. *Nanotechnology* **2010,** *21*, 165503.

33. Lee, J.; Shim, W.; Lee, E.; Noh, J.-S.; Lee, W., Highly Mobile Palladium Thin Films on an Elastomeric Substrate: Nanogap-Based Hydrogen Gas Sensors. *Angew. Chem. Int. Ed.* **2011,** *50*, 5301-5305.

34. Park, B.; Kim, J.; Kang, D.; Jeong, C.; Kim, K. S.; Kim, J. U.; Yoo, P. J.; Kim, T. I., Dramatically Enhanced Mechanosensitivity and Signal-to-Noise Ratio of Nanoscale Crack-Based Sensors: Effect of Crack Depth. *Adv. Mater.* **2016,** *28*, 8130-8137.

35. Phillips, K. R.; Vogel, N.; Burgess, I. B.; Perry, C. C.; Aizenberg, J., Directional Wetting in Anisotropic Inverse Opals. *Langmuir* **2014,** *30*, 7615-7620.

36. Wang, Z.; Volinsky, A. A.; Gallant, N. D., Crosslinking Effect on Polydimethylsiloxane Elastic Modulus Measured by Custom-Built Compression Instrument. *J. Appl. Polym. Sci.* **2014,** *131*, 41050.

37. Li, T.; Huang, Z.; Suo, Z.; Lacour, S. P.; Wagner, S., Stretchability of Thin Metal Films on Elastomer Substrates. *Appl. Phys. Lett.* **2004,** *85*, 3435-3437.

38. Jiang, B.; Liu, L.; Gao, Z.; Feng, Z.; Zheng, Y.; Wang, W., Fast Dual-Stimuli-Responsive Dynamic Surface Wrinkles with High Bistability for Smart Windows and Rewritable Optical Displays. *ACS Appl. Mater. Interfaces* **2019,** *11*, 40406-40415.

39. Lipomi, D. J.; Tee, B. C. K.; Vosgueritchian, M.; Bao, Z., Stretchable Organic Solar Cells. *Adv. Mater.* **2011,** *23*, 1771-1775.

40. Kayser, L. V.; Lipomi, D. J., Stretchable Conductive Polymers and Composites Based on PEDOT and PEDOT:PSS. *Adv. Mater.* **2019,** *31*, 1806133.

41. Ashby, M. F., *Materials and the Environment*. Elsevier: 2012; p 227-273.

42. Jiang, B.; Liu, L.; Gao, Z.; Wang, W., A General and Robust Strategy for Fabricating Mechanoresponsive Surface Wrinkles with Dynamic Switchable Transmittance. *Adv. Optical Mater.* **2018,** *6*, 1800195.

43. Li, H.; Buesen, D.; Williams, R.; Henig, J.; Stapf, S.; Mukherjee, K.; Freier, E.; Lubitz, W.; Winkler, M.; Happe, T.; Plumeré, N., Preventing the Coffee-Ring Effect and Aggregate Sedimentation by *In Situ* Gelation of Monodisperse Materials. *Chem. Sci.* **2018,** *9*, 7596-7605.

44. Poulard, C.; Damman, P., Control of Spreading and Drying of a Polymer Solution from Marangoni Flows. *EPL* **2007,** *80*, 64001.

45.   Gu, X.; Shaw, L.; Gu, K.; Toney, M. F.; Bao, Z., The Meniscus-Guided Deposition of Semiconducting Polymers. *Nature Commun.* **2018**, *9*, 534.

46.   Lu, Z.; Wang, C.; Deng, W.; Achille, M. T.; Jie, J.; Zhang, X., Meniscus-Guided Coating of Organic Crystalline Thin Films for High-Performance Organic Field-Effect Transistors. *J. Mater. Chem. C* **2020**, *8*, 9133-9146.

47.   Richard, M.; Al-Ajaji, A.; Ren, S.; Foti, A.; Tran, J.; Frigoli, M.; Gusarov, B.; Bonnassieux, Y.; Caurel, E. G.; Bulkin, P.; Ossikovski, R.; Yassar, A., Large-scale patterning of π-conjugated materials by meniscus guided coating methods. *Adv. Colloid Interface Sci.* **2020**, *275*, 102080.

48.   Scarratt, L. R. J.; Hoatson, B. S.; Wood, E. S.; Hawkett, B. S.; Neto, C., Durable Superhydrophobic Surfaces *via* Spontaneous Wrinkling of Teflon AF. *ACS Appl. Mater. Interfaces* **2016**, *8*, 6743-6750.

49.   Oscurato, S. L.; Formisano, F.; de Lisio, C.; d'Ischia, M.; Gesuele, F.; Maddalena, P.; Manini, P.; Migliaccio, L.; Pezzella, A., Spontaneous Wrinkle Emergence in Nascent Eumelanin Thin Films. *Soft Matter* **2019**, *15*, 9261-9270.

50.   Li, F.; Hou, H.; Yin, J.; Jiang, X., Near-Infrared Light–Responsive Dynamic Wrinkle Patterns. *Sci. Adv.* **2018**, *4*, eaar5762.

51.   Fowler, P. D.; Ruscher, C.; McGraw, J. D.; Forrest, J. A.; Dalnoki-Veress, K., Controlling Marangoni-Induced Instabilities in Spin-Cast Polymer Films: How to Prepare Uniform Films. *Eur. Phys. J. E* **2016**, *39*, 90.

52.   Lipomi, D. J.; Lee, J. A.; Vosgueritchian, M.; Tee, B. C. K.; Bolander, J. A.; Bao, Z., Electronic Properties of Transparent Conductive Films of PEDOT:PSS on Stretchable Substrates. *Chem. Mater.* **2012**, *24*, 373-382.

53.   Alf, M. E.; Asatekin, A.; Barr, M. C.; Baxamusa, S. H.; Chelawat, H.; Ozaydin-Ince, G.; Petruczok, C. D.; Sreenivasan, R.; Tenhaeff, W. E.; Trujillo, N. J.; Vaddiraju, S.; Xu, J.; Gleason, K. K., Chemical Vapor Deposition of Conformal, Functional, and Responsive Polymer Films. *Adv. Mater.* **2010**, *22*, 1993-2027.

54.   Coclite, A. M.; Howden, R. M.; Borrelli, D. C.; Petruczok, C. D.; Yang, R.; Yagüe, J. L.; Ugur, A.; Chen, N.; Lee, S.; Jo, W. J.; Liu, A.; Wang, X.; Gleason, K. K., 25th Anniversary Article: CVD Polymers: A New Paradigm for Surface Modifi cation and Device Fabrication. *Adv. Mater.* **2013**, *25*, 5392-5423.

55.   Yin, J.; Yagüe, J. L.; Eggenspieler, D.; Gleason, K. K.; Boyce, M. C., Deterministic Order in Surface Micro-Topologies through Sequential Wrinkling. *Adv. Mater.* **2012**, *24*, 5441-5446.

56.   Howden, R. M.; Flores, E. J.; Bulović, V.; Gleason, K. K., The Application of Oxidative Chemical Vapor Deposited (oCVD) PEDOT to Textured and Non-Planar Photovoltaic Device Geometries for Enhanced Light Trapping. *Org. Electron.* **2013**, *14*, 2257-2268.

57.   Khang, D.-Y.; Jiang, H.; Huang, Y.; Rogers, J. A., A Stretchable Form of Single-Crystal Silicon for High-Performance Electronics on Rubber Substrates. *Science* **2006**, *311*, 208-212.

58. Epstein, A. K.; Hong, D.; Kim, P.; Aizenberg, J., Biofilm Attachment Reduction on Bioinspired, Dynamic, Micro-Wrinkling Surfaces. *New J. Phys.* **2013,** *15*, 095018.

59. Chan, E. P.; Smith, E. J.; Hayward, R. C.; Crosby, A. J., Surface Wrinkles for Smart Adhesion. *Adv. Mater.* **2008,** *20*, 711-716.

60. Beuth, J., Cracking of Thin Bonded Films in Residual Tension. *Int. J. Solids Struct.* **1992,** *29*, 1657-1675.

61. Shenoy, V.; Schwartzman, A.; Freund, L., Crack Patterns in Brittle Thin Films. *Int. J. Fract.* **2000,** *103*, 1-17.

62. Huh, D.; Mills, K.; Zhu, X.; Burns, M. A.; Thouless, M.; Takayama, S., Tuneable Elastomeric Nanochannels for Nanofluidic Manipulation. *Nat. Mater.* **2007,** *6*, 424-428.

63. Chung, J. Y.; Youngblood, J. P.; Stafford, C. M., Anisotropic Wetting on Tunable Micro-Wrinkled Surfaces. *Soft Matter* **2007,** *3*, 1163-1169.

64. Bico, J.; Tordeux, C.; Quéré, D., Rough Wetting. *Europhys. Lett.* **2001,** *55*, 214–220.

65. Huntington, M. D.; Engel, C. J.; Hryn, A. J.; Odom, T. W., Polymer Nanowrinkles with Continuously Tunable Wavelengths. *ACS Appl. Mater. Interfaces* **2013,** *5*, 6438-6442.

66. Rae, P. J.; Brown, E. N., The Properties of Poly(Tetrafluoroethylene) (PTFE) in Tension. *Polymer* **2005,** *46*, 8128-8140.

67. Rae, P.; Dattelbaum, D., The Properties of Poly(Tetrafluoroethylene) (PTFE) in Compression. *Polymer* **2004,** *45*, 7615-7625.

68. Speerschneider, C.; Li, C., A Correlation of Mechanical Properties and Microstructure of Polytetrafluoroethylene at Various Temperatures. *J. Appl. Phys.* **1963,** *34*, 3004-3007.

69. Galliot, C.; Luchsinger, R., Uniaxial and Biaxial Mechanical Properties of ETFE Foils. *Polym. Test.* **2011,** *30*, 356-365.

70. Lee, W.-K.; Engel, C. J.; Huntington, M. D.; Hu, J.; Odom, T. W., Controlled Three-Dimensional Hierarchical Structuring by Memory-Based, Sequential Wrinkling. *Nano Lett.* **2015,** *15*, 5624-5629.

71. Dilks, A.; Kay, E., Plasma Polymerization of Ethylene and the Series of Fluoroethylenes: Plasma Effluent Mass Spectrometry and ESCA Studies. *Macromolecules* **1981,** *14*, 855-862.

72. Agraharam, S.; Hess, D. W.; Kohl, P. A.; Allen, S. A. B., Plasma Chemistry in Fluorocarbon Film Deposition from Pentafluoroethane/Argon Mixtures. *J. Vac. Sci. Technol. A* **1999,** *17*, 3265-3271.

73. Astell-Burt, P.; Cairns, J.; Cheetham, A.; Hazel, R., A Study of the Deposition of Polymeric Material onto Surfaces from Fluorocarbon RF Plasmas. *Plasma Chem. Plasma Process.* **1986,** *6*, 417-427.

74. Ferraria, A. M.; da Silva, J. D. L.; do Rego, A. M. B., XPS Studies of Directly Fluorinated HDPE: Problems and Solutions. *Polymer* **2003,** *44*, 7241-7249.

75. Limb, S. J.; Labelle, C. B.; Gleason, K. K.; Edell, D. J.; Gleason, E. F., Growth of Fluorocarbon Polymer Thin Films with High CF_2 Fractions and Low Dangling Bond Concentrations by Thermal Chemical Vapor Deposition. *Appl. Phys. Lett.* **1996,** *68*, 2810.

76. Xie, H.; Wei, J.; Zhang, X., Characterisation of Sol-Gel Thin Films by Spectroscopic Ellipsometry. *J. Phys. Conf. Ser.* **2006,** *28*, 95.

77. Leadley, S.; O'Hare, L.-A.; McMillan, C., *Surface Analysis of Silicones*. Springer: 2012.

78. Hillborg, H.; Ankner, J.; Gedde, U. W.; Smith, G.; Yasuda, H.; Wikström, K., Crosslinked Polydimethylsiloxane Exposed to Oxygen Plasma Studied by Neutron Reflectometry and Other Surface Specific Techniques. *Polymer* **2000,** *41*, 6851-6863.

79. Alexander, M. R.; Short, R.; Jones, F.; Michaeli, W.; Blomfield, C., A Study of $HMDSO/O_2$ Plasma Deposits Using a High-Sensitivity and -Energy Resolution XPS Instrument: Curve Fitting of the Si 2p Core Level. *Appl. Surf. Sci.* **1999,** *137*, 179-183.

80. Ouyang, M.; Yuan, C.; Muisener, R.; Boulares, A.; Koberstein, J., Conversion of Some Siloxane Polymers to Silicon Oxide by UV/Ozone Photochemical Processes. *Chem. Mater.* **2000,** *12*, 1591-1596.

81. Bayley, F. A.; Liao, J. L.; Stavrinou, P. N.; Chiche, A.; Cabral, J. T., Wavefront Kinetics of Plasma Oxidation of Polydimethylsiloxane: Limits for Sub-Micrometer Wrinkling. *Soft Matter* **2014,** *10*, 1155-1166.

82. Nelson, A., Co-Refinement of Multiple-Contrast Neutron/X-Ray Reflectivity Data Using MOTOFIT. *J. Appl. Crystallogr.* **2006,** *39*, 273-276.

83. Stafford, C. M.; Harrison, C.; Beers, K. L.; Karim, A.; Amis, E. J.; VanLandingham, M. R.; Kim, H. C.; Volksen, W.; Miller, R. D.; Simonyi, E. E., A Buckling-Based Metrology for Measuring the Elastic Moduli of Polymeric Thin Films. *Nat. Mater.* **2004,** *3*, 545-550.

84. Johnston, I. D.; McCluskey, D. K.; Tan, C. K. L.; Tracey, M. C., Mechanical Characterization of Bulk Sylgard 184 for Microfluidics and Microengineering. *J. Micromech. Microeng.* **2014,** *24*, 035017.

85. Ebnesajjad, S.; Khaladkar, P. R., *Fluoropolymer Applications in the Chemical Processing Industries: The Definitive User's Guide and Handbook*. William Andrew: 2017.

86. Béfahy, S.; Lipnik, P.; Pardoen, T.; Nascimento, C.; Patris, B.; Bertrand, P.; Yunus, S., Thickness and Elastic Modulus of Plasma Treated PDMS Silica-like Surface Layer. *Langmuir* **2010,** *26*, 3372-3375.

87. Ohishi, T.; Noda, H.; Matsui, T. S.; Jile, H.; Deguchi, S., Tensile Strength of Oxygen Plasma-Created Surface Layer of PDMS. *J. Micromech. Microeng.* **2016,** *27*, 015015.

88. Huntington, M. D.; Engel, C. J.; Odom, T. W., Controlling the Orientation of Nanowrinkles and Nanofolds by Patterning Strain in a Thin Skin Layer on a Polymer Substrate. *Angew. Chem. Int. Ed.* **2014,** *53*, 8117-8121.

89. Mei, H.; Huang, R.; Chung, J. Y.; Stafford, C. M.; Yu, H.-H., Buckling Modes of Elastic Thin Films on Elastic Substrates. *Appl. Phys. Lett.* **2007,** *90*, 151902.

90. Longley, J. E.; Chaudhury, M. K., Determination of the Modulus of Thin Sol-Gel Films Using Buckling Instability. *Macromolecules* **2010,** *43*, 6800-6810.

91. Efimenko, K.; Rackaitis, M.; Manias, E.; Vaziri, A.; Mahadevan, L.; Genzer, J., Nested Self-Similar Wrinkling Patterns in Skins. *Nat. Mater.* **2005,** *4*, 293-297.

92. Lee, J.-H.; Ro, H. W.; Huang, R.; Lemaillet, P.; Germer, T. A.; Soles, C. L.; Stafford, C. M., Anisotropic, Hierarchical Surface Patterns *via* Surface Wrinkling of Nanopatterned Polymer Films. *Nano Lett.* **2012,** *12*, 5995-5999.

93. Aaron, P. G.; Ivan, P.; Sarah, B., *In Situ* Characterization of PDMS in SOI-MEMS. *J. Micromech. Microeng.* **2013,** *23*, 045003.

94. Zhao, Y.; Lu, Q.; Li, M.; Li, X., Anisotropic Wetting Characteristics on Submicrometer-Scale Periodic Grooved Surface. *Langmuir* **2007,** *23*, 6212-6217.

95. Wu, D.; Chen, Q.-D.; Yao, J.; Guan, Y.-C.; Wang, J.-N.; Niu, L.-G.; Fang, H.-H.; Sun, H.-B., A Simple Strategy to Realize Biomimetic Surfaces with Controlled Anisotropic Wetting. *Appl. Phys. Lett.* **2010,** *96*, 053704.

96. Xia, D.; He, X.; Jiang, Y.-B.; Lopez, G. P.; Brueck, S., Tailoring Anisotropic Wetting Properties on Submicrometer-Scale Periodic Grooved Surfaces. *Langmuir* **2010,** *26*, 2700-2706.

97. Xia, D.; Brueck, S. R. J., Strongly Anisotropic Wetting on One-Dimensional Nanopatterned Surfaces. *Nano Lett.* **2008,** *8*, 2819-2824.

98. Lee, W.-K.; Jung, W.-B.; Nagel, S. R.; Odom, T. W., Stretchable Superhydrophobicity from Monolithic, Three-Dimensional Hierarchical Wrinkles. *Nano Lett.* **2016,** *16*, 3774.

99. Cheng, X.; Putz, K. W.; Wood, C. D.; Brinson, L. C., Characterization of Local Elastic Modulus in Confined Polymer Films *via* AFM Indentation. *Macromol. Rapid Commun.* **2015,** *36*, 391-397.

100. Sangwan, V. K.; Hersam, M. C., Electronic Transport in Two-Dimensional Materials. *Annu. Rev. Phys. Chem.* **2018,** *69*, 299-325.

101. Schwierz, F., Graphene Transistors. *Nat. Nanotechnol.* **2010,** *5*, 487-496.

102. Berkelbach, T. C.; Reichman, D. R., Optical and Excitonic Properties of Atomically Thin Transition-Metal Dichalcogenides. *Annu. Rev. Condens. Matter Phys.* **2018,** *9*, 379-396.

103. Sherrott, M. C.; Whitney, W. S.; Jariwala, D.; Biswas, S.; Went, C. M.; Wong, J.; Rossman, G. R.; Atwater, H. A., Anisotropic Quantum Well Electro-Optics in Few-Layer Black Phosphorus. *Nano Lett.* **2018**, 269-276.

104. Akinwande, D.; Brennan, C. J.; Bunch, J. S.; Egberts, P.; Felts, J. R.; Gao, H.; Huang, R.; Kim, J.-S.; Li, T.; Li, Y.; Liechti, K. M.; Lu, N.; Park, H. S.; Reed, E. J.; Wang, P.; Yakobson, B. I.; Zhang, T.; Zhang, Y.-W.; Zhou, Y.; Zhu, Y., A Review on Mechanics and Mechanical Properties of 2D Materials—Graphene and Beyond. *Extreme Mech. Lett.* **2017,** *13*, 42-77.

105. Reserbat-Plantey, A.; Schädler, K. G.; Gaudreau, L.; Navickaite, G.; Güttinger, J.; Chang, D.; Toninelli, C.; Bachtold, A.; Koppens, F. H. L., Electromechanical Control of Nitrogen-Vacancy Defect Emission using Graphene NEMS. *Nat. Commun.* **2016,** *7*, 10218.

106. Özyilmaz, B.; Jarillo-Herrero, P.; Efetov, D.; Abanin, D. A.; Levitov, L. S.; Kim, P., Electronic Transport and Quantum Hall Effect in Bipolar Graphene *p-n-p* Junctions. *Phys. Rev. Lett.* **2007,** *99*, 166804.

107. Wang, G.; Zhang, M.; Chen, D.; Guo, Q.; Feng, X.; Niu, T.; Liu, X.; Li, A.; Lai, J.; Sun, D.; Liao, Z.; Wang, Y.; Chu, P. K.; Ding, G.; Xie, X.; Di, Z.; Wang, X., Seamless Lateral Graphene *p–n* Junctions Formed by Selective *In Situ* Doping for High-Performance Photodetectors. *Nat. Commun.* **2018,** *9*, 5168.

108. Williams, J. R.; DiCarlo, L.; Marcus, C. M., Quantum Hall Effect in a Gate-Controlled *p-n* Junction of Graphene. *Science* **2007,** *317*, 638-641.

109. Bai, J.; Zhong, X.; Jiang, S.; Huang, Y.; Duan, X., Graphene Nanomesh. *Nat. Nanotechnol.* **2010,** *5*, 190-194.

110. Bottari, G.; Herranz, M. Á.; Wibmer, L.; Volland, M.; Rodríguez-Pérez, L.; Guldi, D. M.; Hirsch, A.; Martín, N.; D'Souza, F.; Torres, T., Chemical Functionalization and Characterization of Graphene-Based Materials. *Chem. Soc. Rev.* **2017,** *46*, 4464-4500.

111. Kim, T.; Kim, D.; Choi, C. H.; Joung, D.; Park, J.; Shin, J. C.; Kang, S.-W., Structural Defects in a Nanomesh of Bulk MoS_2 Using an Anodic Aluminum Oxide Template for Photoluminescence Efficiency Enhancement. *Sci. Rep.* **2018,** *8*, 6648-6648.

112. Wu, Q.; Wu, Y.; Hao, Y.; Geng, J.; Charlton, M.; Chen, S.; Ren, Y.; Ji, H.; Li, H.; Boukhvalov, D. W.; Piner, R. D.; Bielawski, C. W.; Ruoff, R. S., Selective Surface Functionalization at Regions of High Local Curvature in Graphene. *Chem. Commun.* **2013,** *49*, 677-679.

113. Feng, W.; Long, P.; Feng, Y.; Li, Y., Two-Dimensional Fluorinated Graphene: Synthesis, Structures, Properties and Applications. *Adv. Sci.* **2016,** *3*, 1500413.

114. Lee, J.-K.; Yamazaki, S.; Yun, H.; Park, J.; Kennedy, G. P.; Kim, G.-T.; Pietzsch, O.; Wiesendanger, R.; Lee, S.; Hong, S.; Dettlaff-Weglikowska, U.; Roth, S., Modification of Electrical Properties of Graphene by Substrate-Induced Nanomodulation. *Nano Lett.* **2013,** *13*, 3494-3500.

115. Castellanos-Gomez, A.; Roldán, R.; Cappelluti, E.; Buscema, M.; Guinea, F.; van der Zant, H. S. J.; Steele, G. A., Local Strain Engineering in Atomically Thin MoS_2. *Nano Lett.* **2013,** *13*, 5361-5366.

116. Yang, S.; Wang, C.; Sahin, H.; Chen, H.; Li, Y.; Li, S.-S.; Suslu, A.; Peeters, F. M.; Liu, Q.; Li, J.; Tongay, S., Tuning the Optical, Magnetic, and Electrical Properties of $ReSe_2$ by Nanoscale Strain Engineering. *Nano Lett.* **2015,** *15*, 1660-1666.

117. Bai, L.; Xu, Y.; Jiang, Y.; Chen, H.; Li, X.; Zhang, J.; Song, G., Transfer Method of Crumpled Graphene and Its Application for Human Strain Monitoring. *Sens. Actuators A* **2017,** *260*, 153-160.

118. Deng, S.; Berry, V., Wrinkled, Rippled and Crumpled Graphene: An Overview of Formation Mechanism, Electronic Properties, and Applications. *Mater. Today* **2016,** *19*, 197-212.

119. Kang, P.; Kim, K.-H.; Park, H.-G.; Nam, S., Mechanically Reconfigurable Architectured Graphene for Tunable Plasmonic Resonances. *Light Sci. Appl.* **2018,** *7*, 17.

120. Zang, J.; Ryu, S.; Pugno, N.; Wang, Q.; Tu, Q.; Buehler, M. J.; Zhao, X., Multifunctionality and Control of the Crumpling and Unfolding of Large-Area Graphene. *Nat. Mater.* **2013,** *12*, 321-325.

121. Thomas, A. V.; Andow, B. C.; Suresh, S.; Eksik, O.; Yin, J.; Dyson, A. H.; Koratkar, N., Controlled Crumpling of Graphene Oxide Films for Tunable Optical Transmittance. *Adv. Mater.* **2015,** *27*, 3256-3265.

122. Liu, N.; Chortos, A.; Lei, T.; Jin, L.; Kim, T. R.; Bae, W.-G.; Zhu, C.; Wang, S.; Pfattner, R.; Chen, X.; Sinclair, R.; Bao, Z., Ultratransparent and Stretchable Graphene Electrodes. *Sci. Adv.* **2017,** *3*, e1700159.

123. Lee, W.-K.; Kang, J.; Chen, K.-S.; Engel, C. J.; Jung, W.-B.; Rhee, D.; Hersam, M. C.; Odom, T. W., Multiscale, Hierarchical Patterning of Graphene by Conformal Wrinkling. *Nano Lett.* **2016,** *16*, 7121-7127.

124. Ruffini, A.; Durinck, J.; Colin, J.; Coupeau, C.; Grilhé, J., Interface Step-Induced Thin-Film Delamination and Buckling. *Acta Mater.* **2013,** *61*, 4429-4438.

125. Wang, Z.; Tonderys, D.; Leggett, S. E.; Williams, E. K.; Kiani, M. T.; Spitz Steinberg, R.; Qiu, Y.; Wong, I. Y.; Hurt, R. H., Wrinkled, Wavelength-Tunable Graphene-Based Surface Topographies for Directing Cell Alignment and Morphology. *Carbon* **2016,** *97*, 14-24.

126. Lee, C.; Wei, X.; Kysar, J. W.; Hone, J., Measurement of the Elastic Properties and Intrinsic Strength of Monolayer Graphene. *Science* **2008,** *321*, 385-388.

127. Stafford, C. M.; Guo, S.; Harrison, C.; Chiang, M. Y. M., Combinatorial and High-Throughput Measurements of the Modulus of Thin Polymer Films. *Rev. Sci. Instrum.* **2005,** *76*, 062207.

128. Xiang, Y.; Li, T.; Suo, Z.; Vlassak, J. J., High Ductility of a Metal Film Adherent on a Polymer Substrate. *Appl. Phys. Lett.* **2005,** *87*, 161910.

129. Li, T.; Huang, Z. Y.; Xi, Z. C.; Lacour, S. P.; Wagner, S.; Suo, Z., Delocalizing Strain in a Thin Metal Film on a Polymer Substrate. *Mech. Mater.* **2005,** *37*, 261-273.

130. Kotakoski, J.; Meyer, J. C., Mechanical Properties of Polycrystalline Graphene Based on a Realistic Atomistic Model. *Phys. Rev. B* **2012,** *85*, 195447.

131. Zhang, P.; Ma, L.; Fan, F.; Zeng, Z.; Peng, C.; Loya, P. E.; Liu, Z.; Gong, Y.; Zhang, J.; Zhang, X.; Ajayan, P. M.; Zhu, T.; Lou, J., Fracture Toughness of Graphene. *Nat. Commun.* **2014,** *5*, 3782.

132. Wang, Q. H.; Jin, Z.; Kim, K. K.; Hilmer, A. J.; Paulus, G. L. C.; Shih, C.-J.; Ham, M.-H.; Sanchez-Yamagishi, J. D.; Watanabe, K.; Taniguchi, T.; Kong, J.; Jarillo-Herrero, P.;

Strano, M. S., Understanding and Controlling the Substrate Effect on Graphene Electron-Transfer Chemistry *via* Reactivity Imprint Lithography. *Nat. Chem.* **2012,** *4*, 724-732.

133. Zhao, G.; Li, X.; Huang, M.; Zhen, Z.; Zhong, Y.; Chen, Q.; Zhao, X.; He, Y.; Hu, R.; Yang, T.; Zhang, R.; Li, C.; Kong, J.; Xu, J.-B.; Ruoff, R. S.; Zhu, H., The Physics and Chemistry of Graphene-on-Surfaces. *Chem. Soc. Rev.* **2017,** *46*, 4417-4449.

134. Wang, Y. y.; Ni, Z. h.; Yu, T.; Shen, Z. X.; Wang, H. m.; Wu, Y. h.; Chen, W.; Shen Wee, A. T., Raman Studies of Monolayer Graphene: The Substrate Effect. *J. Phys. Chem. C* **2008,** *112*, 10637-10640.

135. Lee, J. E.; Ahn, G.; Shim, J.; Lee, Y. S.; Ryu, S., Optical Separation of Mechanical Strain from Charge Doping in Graphene. *Nat. Commun.* **2012,** *3*, 1024.

136. Das, A.; Pisana, S.; Chakraborty, B.; Piscanec, S.; Saha, S. K.; Waghmare, U. V.; Novoselov, K. S.; Krishnamurthy, H. R.; Geim, A. K.; Ferrari, A. C.; Sood, A. K., Monitoring Dopants by Raman Scattering in an Electrochemically Top-Gated Graphene Transistor. *Nat. Nanotech.* **2008,** *3*, 210-215.

137. Lin, Y.-C.; Lu, C.-C.; Yeh, C.-H.; Jin, C.; Suenaga, K.; Chiu, P.-W., Graphene Annealing: How Clean Can It Be? *Nano Lett.* **2012,** *12*, 414-419.

138. Bissett, M. A.; Izumida, W.; Saito, R.; Ago, H., Effect of Domain Boundaries on the Raman Spectra of Mechanically Strained Graphene. *ACS Nano* **2012,** *6*, 10229-10238.

139. Yu, C.; O'Brien, K.; Zhang, Y.-H.; Yu, H.; Jiang, H., Tunable Optical Gratings Based on Buckled Nanoscale Thin Films on Transparent Elastomeric Substrates. *Appl. Phys. Lett.* **2010,** *96*, 041111.

140. Khare, K.; Zhou, J.; Yang, S., Tunable Open-Channel Microfluidics on Soft Poly(Dimethylsiloxane) (PDMS) Substrates with Sinusoidal Grooves. *Langmuir* **2009,** *25*, 12794-12799.

141. Lee, M. H.; Huntington, M. D.; Zhou, W.; Yang, J. C.; Odom, T. W., Programmable Soft Lithography: Solvent-Assisted Nanoscale Embossing. *Nano Lett.* **2011,** *11*, 311-315.

142. Shi, H.; Pan, H.; Zhang, Y.-W.; Yakobson, B. I., Quasiparticle Band Structures and Optical Properties of Strained Monolayer MoS_2 and WS_2. *Phys. Rev. B* **2013,** *87*, 155304.

143. He, K.; Poole, C.; Mak, K. F.; Shan, J., Experimental Demonstration of Continuous Electronic Structure Tuning via Strain in Atomically Thin MoS_2. *Nano Lett.* **2013,** *13*, 2931-2936.

144. Peng, Z.; Chen, X.; Fan, Y.; Srolovitz, D. J.; Lei, D., Strain Engineering of 2D Semiconductors and Graphene: From Strain Fields to Band-Structure Tuning and Photonic Applications. *Light Sci. Appl.* **2020,** *9*, 190.

145. Castellanos-Gomez, A.; Singh, V.; van der Zant, H. S. J.; Steele, G. A., Mechanics of Freely-Suspended Ultrathin Layered Materials. *Ann. Phys. (Berlin)* **2015,** *527*, 27-44.

146. Deng, S.; Rhee, D.; Lee, W.-K.; Che, S.; Keisham, B.; Berry, V.; Odom, T. W., Graphene Wrinkles Enable Spatially Defined Chemistry. *Nano Lett.* **2019,** *19*, 5640-5646.

147. Splendiani, A.; Sun, L.; Zhang, Y.; Li, T.; Kim, J.; Chim, C.-Y.; Galli, G.; Wang, F., Emerging Photoluminescence in Monolayer MoS$_2$. *Nano Lett.* **2010,** *10*, 1271-1275.

148. Shao, Z.-C.; Zhao, Y.; Zhang, W.; Cao, Y.; Feng, X.-Q., Curvature Induced Hierarchical Wrinkling Patterns in Soft Bilayers. *Soft Matter* **2016,** *12*, 7977-7982.

149. Suk, J. W.; Kitt, A.; Magnuson, C. W.; Hao, Y.; Ahmed, S.; An, J.; Swan, A. K.; Goldberg, B. B.; Ruoff, R. S., Transfer of CVD-Grown Monolayer Graphene onto Arbitrary Substrates. *ACS Nano* **2011,** *5*, 6916-6924.

150. Cha, S.; Cha, M.; Lee, S.; Kang, J. H.; Kim, C., Low-Temperature, Dry Transfer-Printing of a Patterned Graphene Monolayer. *Sci. Rep.* **2015,** *5*, 17877.

151. Politano, A.; Chiarello, G., Probing the Young's Modulus and Poisson's Ratio in Graphene/Metal Interfaces and Graphite: A Comparative Study. *Nano Res.* **2015,** *8*, 1847-1856.

152. Wang, M. C.; Chun, S.; Han, R. S.; Ashraf, A.; Kang, P.; Nam, S., Heterogeneous, Three-Dimensional Texturing of Graphene. *Nano Lett.* **2015,** *15*, 1829-1835.

153. Kang, P.; Wang, M. C.; Knapp, P. M.; Nam, S., Crumpled Graphene Photodetector with Enhanced, Strain-Tunable, and Wavelength-Selective Photoresponsivity. *Adv. Mater.* **2016,** *28*, 4639-4645.

154. Kim, H.-J.; Song, Y.-W.; Namgung, S. D.; Song, M.-K.; Yang, S.; Kwon, J.-Y., Optical Properties of the Crumpled Pattern of Selectively Layered MoS$_2$. *Opt. Lett.* **2018,** *43*, 4590-4593.

155. Chen, P.-Y.; Sodhi, J.; Qiu, Y.; Valentin, T. M.; Steinberg, R. S.; Wang, Z.; Hurt, R. H.; Wong, I. Y., Multiscale Graphene Topographies Programmed by Sequential Mechanical Deformation. *Adv. Mater.* **2016,** *28*, 3564-3571.

156. Cho, H.; Chung, J.; Shin, G.; Sim, J.-Y.; Kim, D. S.; Lee, S.; Hwang, W., Toward Sustainable Output Generation of Liquid–Solid Contact Triboelectric Nanogenerators: The Role of Hierarchical Structures. *Nano Energy* **2019,** *56*, 56-64.

157. Park, S.; Park, J.; Kim, Y.-g.; Bae, S.; Kim, T.-W.; Park, K.-I.; Hong, B. H.; Jeong, C. K.; Lee, S.-K., Laser-Directed Synthesis of Strain-Induced Crumpled MoS$_2$ Structure for Enhanced Triboelectrification Toward Haptic Sensors. *Nano Energy* **2020,** *78*, 105266.

158. Kang, J.; Sangwan, V. K.; Wood, J. D.; Hersam, M. C., Solution-Based Processing of Monodisperse Two-Dimensional Nanomaterials. *Accounts of Chemical Research* **2017,** *50*, 943-951.

159. Christian, P.; Ehmann, H. M. A.; Werzer, O.; Coclite, A. M., Wrinkle Formation in a Polymeric Drug Coating Deposited *via* Initiated Chemical Vapor Deposition. *Soft Matter* **2016,** *12*, 9501-9508.

160. Robinson, A. P. G.; Palmer, R. E.; Tada, T.; Kanayama, T.; Preece, J. A., A Fullerene Derivative as an Electron Beam Resist for Nanolithography. *Appl. Phys. Lett.* **1998,** *72*, 1302-1304.

161. Chan, E. P.; Page, K. A.; Im, S. H.; Patton, D. L.; Huang, R.; Stafford, C. M., Viscoelastic Properties of Confined Polymer Films Measured *via* Thermal Wrinkling. *Soft Matter* **2009,** *5*, 4638-4641.

162. Greaves, G. N.; Greer, A. L.; Lakes, R. S.; Rouxel, T., Poisson's Ratio and Modern Materials. *Nat. Mater.* **2011,** *10*, 823-837.

163. Joshi, A.; Fussell, G.; Thomas, J.; Hsuan, A.; Lowman, A.; Karduna, A.; Vresilovic, E.; Marcolongo, M., Functional Compressive Mechanics of a PVA/PVP Nucleus Pulposus Replacement. *Biomaterials* **2006,** *27*, 176-184.

164. Flores-Merino, M. V.; Chirasatitsin, S.; LoPresti, C.; Reilly, G. C.; Battaglia, G.; Engler, A. J., Nanoscopic Mechanical Anisotropy in Hydrogel Surfaces. *Soft Matter* **2010,** *6*, 4466-4470.

165. Xia, Y.; Whitesides, G. M., Soft Lithography. *Angew. Chem. Int. Ed.* **1998,** *37*, 550-575.

166. Qin, D.; Xia, Y.; Whitesides, G. M., Soft Lithography for Micro- and Nanoscale Patterning. *Nat. Protoc.* **2010,** *5*, 491-502.

167. Xia, Y.; Kim, E.; Zhao, X.-M.; Rogers, J. A.; Prentiss, M.; Whitesides, G. M., Complex Optical Surfaces Formed by Replica Molding Against Elastomeric Masters. *Science* **1996,** *273*, 347.

168. Lee, W.-K.; Jung, W.-B.; Rhee, D.; Hu, J.; Lee, Y.-A. L.; Jacobson, C.; Jung, H.-T.; Odom, T. W., Monolithic Polymer Nanoridges with Programmable Wetting Transitions. *Adv. Mater.* **2018,** *30*, 1706657.

169. Odom, T. W.; Love, J. C.; Wolfe, D. B.; Paul, K. E.; Whitesides, G. M., Improved Pattern Transfer in Soft Lithography Using Composite Stamps. *Langmuir* **2002,** *18*, 5314-5320.

170. Potyrailo, R. A.; Bonam, R. K.; Hartley, J. G.; Starkey, T. A.; Vukusic, P.; Vasudev, M.; Bunning, T.; Naik, R. R.; Tang, Z.; Palacios, M. A.; Larsen, M.; Le Tarte, L. A.; Grande, J. C.; Zhong, S.; Deng, T., Towards Outperforming Conventional Sensor Arrays with Fabricated Individual Photonic Vapour Sensors Inspired by *Morpho* Butterflies. *Nat. Commun.* **2015,** *6*, 7959.

171. Wakerley, D.; Lamaison, S.; Ozanam, F.; Menguy, N.; Mercier, D.; Marcus, P.; Fontecave, M.; Mougel, V., Bio-Inspired Hydrophobicity Promotes CO_2 Reduction on a Cu Surface. *Nat. Mater.* **2019,** *18*, 1222-1227.

172. Bonnefont, A.; Ruvinskiy, P.; Rouhet, M.; Orfanidi, A.; Neophytides, S.; Savinova, E., Advanced Catalytic Layer Architectures for Polymer Electrolyte Membrane Fuel Cells. *WIREs Energy Environ.* **2014,** *3*, 505-521.

173. Sun, Y.; Choi, W. M.; Jiang, H.; Huang, Y. Y.; Rogers, J. A., Controlled Buckling of Semiconductor Nanoribbons for Stretchable Electronics. *Nat. Nanotech.* **2006,** *1*, 201-207.

174. Mouterde, T.; Lehoucq, G.; Xavier, S.; Checco, A.; Black, C. T.; Rahman, A.; Midavaine, T.; Clanet, C.; Quéré, D., Antifogging Abilities of Model Nanotextures. *Nat. Mater.* **2017,** *16*, 658-663.

175. van Lare, M. C.; Polman, A., Optimized Scattering Power Spectral Density of Photovoltaic Light-Trapping Patterns. *ACS Photonics* **2015,** *2*, 822-831.

176. Li, T.; Ren, T.; He, J., Chapter 1 - The Inspiration of Nature: Natural Counterparts with Self-cleaning Functions. In *Self-cleaning Coatings: Structure, Fabrication and Application*, The Royal Society of Chemistry: 2017.

177. Tian, Y.; Pesika, N.; Zeng, H.; Rosenberg, K.; Zhao, B.; McGuiggan, P.; Autumn, K.; Israelachvili, J., Adhesion and Friction in Gecko Toe Attachment and Detachment. *Proc. Natl. Acad. Sci. U. S. A.* **2006,** *103*, 19320.

178. Su, B.; Tian, Y.; Jiang, L., Bioinspired Interfaces with Superwettability: From Materials to Chemistry. *J. Am. Chem. Soc.* **2016,** *138*, 1727-1748.

179. Yong, J.; Chen, F.; Yang, Q.; Huo, J.; Hou, X., Superoleophobic Surfaces. *Chem. Soc. Rev.* **2017,** *46*, 4168-4217.

180. Butt, H.; Yetisen, A. K.; Mistry, D.; Khan, S. A.; Hassan, M. U.; Yun, S. H., *Morpho* Butterfly-Inspired Nanostructures. *Adv. Opt. Mater.* **2016,** *4*, 497-504.

181. Zhang, S.; Chen, Y., Nanofabrication and Coloration Study of Artificial *Morpho* Butterfly Wings with Aligned Lamellae Layers. *Sci. Rep.* **2015,** *5*, 16637.

182. Miljkovic, N.; Enright, R.; Nam, Y.; Lopez, K.; Dou, N.; Sack, J.; Wang, E. N., Jumping-droplet-enhanced condensation on scalable superhydrophobic nanostructured surfaces. *Nano letters* **2013,** *13*, 179-187.

183. Bai, H.; Wang, L.; Ju, J.; Sun, R.; Zheng, Y.; Jiang, L., Efficient Water Collection on Integrative Bioinspired Surfaces with Star-Shaped Wettability Patterns. *Advanced Materials* **2014,** *26*, 5025-5030.

184. Wisdom, K. M.; Watson, J. A.; Qu, X.; Liu, F.; Watson, G. S.; Chen, C.-H., Self-cleaning of superhydrophobic surfaces by self-propelled jumping condensate. *Proceedings of the National Academy of Sciences* **2013,** *110*, 7992-7997.

185. Mulroe, M. D.; Srijanto, B. R.; Ahmadi, S. F.; Collier, C. P.; Boreyko, J. B., Tuning Superhydrophobic Nanostructures to Enhance Jumping-Droplet Condensation. *ACS Nano* **2016**.

186. Hou, Y.; Yu, M.; Chen, X.; Wang, Z.; Yao, S., Recurrent filmwise and dropwise condensation on a beetle mimetic surface. *ACS nano* **2014,** *9*, 71-81.

187. Ölçeroğlu, E.; McCarthy, M., Self-Organization of Microscale Condensate for Delayed Flooding of Nanostructured Superhydrophobic Surfaces. *ACS Applied Materials & Interfaces* **2016,** *8*, 5729-5736.

188. Garrod, R.; Harris, L.; Schofield, W.; McGettrick, J.; Ward, L.; Teare, D.; Badyal, J., Mimicking a Stenocara beetle's back for microcondensation using plasmachemical patterned superhydrophobic− superhydrophilic surfaces. *Langmuir* **2007,** *23*, 689-693.

189. Zhai, L.; Berg, M. C.; Cebeci, F. Ç.; Kim, Y.; Milwid, J. M.; Rubner, M. F.; Cohen, R. E., Patterned superhydrophobic surfaces: toward a synthetic mimic of the Namib Desert beetle. *Nano Letters* **2006,** *6*, 1213-1217.

190. Singh, R., Chapter 2 - Water and Membrane Treatment. In *Membrane Technology and Engineering for Water Purification*, Butterworth-Heinemann: 2015.

191. Natarajan, K. A., *Chapter 12 - Biofouling and Microbially Influenced Corrosion*. Elsevier: 2018.

192. Tacconelli, E.; Carrara, E.; Savoldi, A.; Harbarth, S.; Mendelson, M.; Monnet, D. L.; Pulcini, C.; Kahlmeter, G.; Kluytmans, J.; Carmeli, Y.; Ouellette, M.; Outterson, K.; Patel, J.; Cavaleri, M.; Cox, E. M.; Houchens, C. R.; Grayson, M. L.; Hansen, P.; Singh, N.; Theuretzbacher, U., et al., Discovery, Research, and Development of New Antibiotics: The WHO Priority List of Antibiotic-Resistant Bacteria and Tuberculosis. *Lancet Infect. Dis.* **2018,** *18*, 318-327.

193. Costerton, J. W.; Stewart, P. S.; Greenberg, E. P., Bacterial Biofilms: A Common Cause of Persistent Infections. *Science* **1999,** *284*, 1318-1322.

194. Zhao, K.; Tseng, B. S.; Beckerman, B.; Jin, F.; Gibiansky, M. L.; Harrison, J. J.; Luijten, E.; Parsek, M. R.; Wong, G. C. L., Psl Trails Guide Exploration and Microcolony Formation in *Pseudomonas aeruginosa* Biofilms. *Nature* **2013,** *497*, 388-391.

195. Kiedrowski, M. R.; Horswill, A. R., New Approaches for Treating Staphylococcal Biofilm Infections. *Ann. N. Y. Acad. Sci.* **2011,** *1241*, 104-121.

196. Stoodley, P.; Sauer, K.; Davies, D.; Costerton, J. W., Biofilms as Complex Differentiated Communities. *Annu. Rev. Microbiol.* **2002,** *56*, 187-209.

197. Zhang, H.; Chiao, M., Anti-Fouling Coatings of Poly(Dimethylsiloxane) Devices for Biological and Biomedical Applications. *J. Med. Biol. Eng.* **2015,** *35*, 143-155.

198. Yang, W. J.; Neoh, K.-G.; Kang, E.-T.; Teo, S. L.-M.; Rittschof, D., Polymer Brush Coatings for Combating Marine Biofouling. *Prog. Polym. Sci.* **2014,** *39*, 1017-1042.

199. Banerjee, I.; Pangule, R. C.; Kane, R. S., Antifouling Coatings: Recent Developments in the Design of Surfaces That Prevent Fouling by Proteins, Bacteria, and Marine Organisms. *Adv. Mater.* **2011,** *23*, 690-718.

200. Feng, G.; Cheng, Y.; Wang, S.-Y.; Borca-Tasciuc, D. A.; Worobo, R. W.; Moraru, C. I., Bacterial Attachment and Biofilm Formation on Surfaces are Reduced by Small-Diameter Nanoscale Pores: How Small is Small Enough? *npj Biofilms Microbiomes* **2015,** *1*, 15022.

201. Hizal, F.; Choi, C.-H.; Busscher, H. J.; Van der Mei, H. C., Staphylococcal Adhesion, Detachment and Transmission on Nanopillared Si Surfaces. *ACS Appl. Mater. Interfaces* **2016,** *8*, 30430-30439.

202. Chung, K. K.; Schumacher, J. F.; Sampson, E. M.; Burne, R. A.; Antonelli, P. J.; Brennan, A. B., Impact of Engineered Surface Microtopography on Biofilm Formation of *Staphylococcus aureus*. *Biointerphases* **2007,** *2*, 89-94.

203. Crawford, R. J.; Webb, H. K.; Truong, V. K.; Hasan, J.; Ivanova, E. P., Surface Topographical Factors Influencing Bacterial Attachment. *Adv. Colloid Interface Sci.* **2012,** *179*, 142-149.

204. Martins, E. R.; Li, J.; Liu, Y.; Depauw, V.; Chen, Z.; Zhou, J.; Krauss, T. F., Deterministic Quasi-Random Nanostructures for Photon Control. *Nat. Commun.* **2013,** *4*, 2665.

205. Wang, R.; Xu, L.-H.; Li, Y.-Q.; Zhou, L.; Li, C.; Ou, Q.-D.; Chen, J.-D.; Shen, S.; Tang, J.-X., Broadband Light Out-Coupling Enhancement of Flexible Organic Light-Emitting Diodes Using Biomimetic Quasirandom Nanostructures. *Adv. Opt. Mater.* **2015,** *3*, 203-210.

206. Forster, J. D.; Noh, H.; Liew, S. F.; Saranathan, V.; Schreck, C. F.; Yang, L.; Park, J.-G.; Prum, R. O.; Mochrie, S. G. J.; O'Hern, C. S.; Cao, H.; Dufresne, E. R., Biomimetic Isotropic Nanostructures for Structural Coloration. *Adv. Mater.* **2010,** *22*, 2939-2944.

207. Li, K.; Li, J.; Reardon, C.; Schuster, C. S.; Wang, Y.; Triggs, G. J.; Damnik, N.; Müenchenberger, J.; Wang, X.; Martins, E. R.; Krauss, T. F., High Speed E-Beam Writing for Large Area Photonic Nanostructures — A Choice of Parameters. *Sci. Rep.* **2016,** *6*, 32945.

208. Pala, R. A.; Liu, J. S. Q.; Barnard, E. S.; Askarov, D.; Garnett, E. C.; Fan, S.; Brongersma, M. L., Optimization of Non-Periodic Plasmonic Light-Trapping Layers for Thin-Film Solar Cells. *Nat. Commun.* **2013,** *4*, 2095.

209. Shirasaki, Y.; Supran, G. J.; Bawendi, M. G.; Bulović, V., Emergence of Colloidal Quantum-Dot Light-Emitting Technologies. *Nat. Photon.* **2013,** *7*, 13-23.

210. Tan, Y.; Li, R.; Xu, H.; Qin, Y.; Song, T.; Sun, B., Ultrastable and Reversible Fluorescent Perovskite Films Used for Flexible Instantaneous Display. *Adv. Func. Mater.* **2019,** *29*, 1900730.

211. Choi, M.; Park, Y. J.; Sharma, B. K.; Bae, S.-R.; Kim, S. Y.; Ahn, J.-H., Flexible Active-Matrix Organic Light-Emitting Diode Display Enabled by MoS_2 Thin-Film Transistor. *Sci. Adv.* **2018,** *4*, eaas8721.

212. Cao, Y.; Wang, N.; Tian, H.; Guo, J.; Wei, Y.; Chen, H.; Miao, Y.; Zou, W.; Pan, K.; He, Y.; Cao, H.; Ke, Y.; Xu, M.; Wang, Y.; Yang, M.; Du, K.; Fu, Z.; Kong, D.; Dai, D.; Jin, Y., et al., Perovskite Light-Emitting Diodes Based on Spontaneously Formed Submicrometre-Scale Structures. *Nature* **2018,** *562*, 249-253.

213. Lee, Y.-J.; Kim, S.-H.; Huh, J.; Kim, G.-H.; Lee, Y.-H.; Cho, S.-H.; Kim, Y.-C.; Do, Y. R., A high-Extraction-Efficiency Nanopatterned Organic Light-Emitting Diode. *Appl. Phys. Lett.* **2003,** *82*, 3779-3781.

214. Richter, J. M.; Abdi-Jalebi, M.; Sadhanala, A.; Tabachnyk, M.; Rivett, J. P. H.; Pazos-Outón, L. M.; Gödel, K. C.; Price, M.; Deschler, F.; Friend, R. H., Enhancing Photoluminescence Yields in Lead Halide Perovskites by Photon Recycling and Light Out-Coupling. *Nat. Commun.* **2016,** *7*, 13941.

<div align="center">

CURRICULUM VITAE

Dongjoon Rhee

</div>

<div align="center">

Department of Materials Science and Engineering
Northwestern University, Evanston, IL 60208, USA
Phone: 847-284-8797 / Email: djrhee89@u.northwestern.edu

</div>

EDUCATION

Northwestern University, Evanston, IL, USA
　Ph.D. candidate in Materials Science and Engineering (GPA: 3.98/4.00)　　　2017-
　M.S. in Materials Science and Engineering (GPA: 3.97/4.00)　　　　　　　2014-2016

Hanyang University, Seoul, South Korea
　B.S. in Materials Science and Engineering　　　　　　　　　　　　　　2007-2013
　(Overall GPA: 4.40/4.50, Major GPA: 4.48/4.50)

RESEARCH EXPERIENCE

The Odom group, Northwestern University
Graduate Student Researcher (Advisor: Prof. Teri W. Odom), 2015-present
　Multiscale patterning based on polymer nanowrinkles
- Developed crack-free, reconfigurable patterns with switchable wetting properties
- Established methods to texture 2D materials with spatially defined feature sizes
- Designed hierarchical structures for superhydrophobic and antibiofouling surfaces
- Fabricated quasi-random nanostructures for light manipulation

Haile group, Northwestern University
Graduate Student Researcher (Advisor: Prof. Sossina M. Haile), 2014-2015
　Metal nanocatalyst arrays for solid oxide fuel cell anodes
- Patterned metal nanoparticles using nanosphere lithography
- Evaluated catalytically active sites in the model anodes

Computational Materials Science and Engineering Lab, Hanyang University
Undergraduate Student Researcher (Advisor: Prof. Yong-Chae Chung), 2014
　Density functional theory study of nitrogen-doped graphene for hydrogen storage
- Calculated adsorption sites of H_2 molecules on graphene and the binding energies
- Analyzed electronic structures of the system

Korgel group, The University of Texas at Austin
Undergraduate Student Researcher (Advisor: Prof. Brian A. Korgel), 2012-2013
　Colloidal $CuInSe_2$ quantum dot solar cells
- Synthesized colloidal $CuInSe_2$ nanoparticles with controlled optical gaps
- Fabricated solar cells using spray-coating and tested power conversion efficiencies

Nano Electronic Devices & Materials Lab, Hanyang University
Undergraduate Student Researcher (Advisor: Prof. Changhwan Choi), 2011-2012
Sol-gel processed Cu_2ZnSnS_4 light absorber layers for thin film solar cells
  • Optimized precursor solution for spin-coating
  • Characterized optical properties and crystallinity of the resulting thin films

PUBLICATIONS

1. **D. Rhee**, S. Deng, T.W. Odom, "Soft Skin Layers for Reconfigurable and Programmable Nanowrinkles," *Nanoscale* **2020**, *12*, 23920-23928. DOI: 10.1039/d0nr07054h

2. Y.-A.L. Lee, V. Pryamitsyn, **D. Rhee**, M. Olvera de la Cruz, T.W. Odom, "Strain-Dependent Nanowrinkle Confinement of Block Copolymers," *Nano Lett.* **2020**, *20*, 1433-1439. DOI: 10.1021/acs.nanolett.9b05189

3. **D. Rhee**,[†] J.T. Paci,[†] S. Deng, W.-K. Lee, G.C. Schatz, T.W. Odom, "Soft Skin Layers Enable Area-Specific Multiscale Graphene Wrinkles with Switchable Orientations," *ACS Nano* **2020**, *14*, 166-174. DOI: 10.1021/acsnano.9b06325 ([†]Equal contribution)

4. S. Deng, **D. Rhee**, W.-K. Lee, S. Che, B. Keisham, V. Berry, T.W. Odom, "Graphene Wrinkles Enable Spatially Defined Chemistry," *Nano Lett.* **2019**, *19*, 5640-5646. DOI: 10.1021/acs.nanolett.9b02178

5. M. Anni, **D. Rhee**, W.-K. Lee, "Random Lasing Engineering in Poly-(9-9dioctylfluorene) Active Waveguides Deposited on Wrinkles Corrugated Surfaces," *ACS Appl. Mater. Interfaces* **2019**, *11*, 9385-9393. DOI: 10.1021/acsami.8b18187

6. W.-K. Lee, W.-B. Jung, **D. Rhee**, J. Hu, Y.L. Lee, C. Jacobson, H.-T. Jung, T.W. Odom, "Monolithic Polymer Nanoridges with Programmable Wetting Transitions," *Adv. Mater.* **2018**, *30*, 1706657. DOI: 10.1002/adma.201706657

7. W.-K. Lee, S. Yu, C.J. Engel, T. Reese, **D. Rhee**, W. Chen, T.W. Odom, "Concurrent Design of Quasi-Random Photonic Nanostructures," *Proc. Natl. Acad. Sci. U.S.A.* **2017**, *114*, 8734-8739. DOI: 10.1073/pnas.1704711114

8. A. Paul, M. Stührenberg, S. Chen, **D. Rhee**, W.-K. Lee, T.W. Odom, S. Heilshorn, A. Enejder, "Micro- and Nano-Patterned Elastin-Like Polypeptide Hydrogels for Stem Cell Culture," *Soft Matter 2017, 13, 5665-5675.* DOI: 10.1039/C7SM00487G

9. **D. Rhee**, W.-K. Lee, T.W. Odom, "Crack-Free, Soft Wrinkles Enable Switchable Anisotropic Wetting," *Angew. Chem. Int. Ed.* **2017**, *56*, 6523-6527. DOI: 10.1002/anie.201701968

10. J. Hu, X. Ren, A.N. Reed, T. Reese, **D. Rhee**, B. Howe, L.J. Lauhon, A.M. Urbas, T.W. Odom, "Evolutionary Design and Prototyping of Single Crystalline Titanium Nitride Lattice Optics," *ACS Photonics* **2017**, *4*, 606-612. DOI: 10.1021/acsphotonics.6b00955

11. W.-K. Lee, J. Kang, K.-S. Chen, C.J. Engel, W.-B. Jung, **D. Rhee**, M.C. Hersam, T.W. Odom, "Multiscale, Hierarchical Patterning of Graphene by Conformal Wrinkling," *Nano Lett.* **2016**, *16*, 7121-7127. DOI: 10.1021/acs.nanolett.6b03415

12. C.J. Stolle, T.B. Harvey, D.R. Pernik, J.I. Hibbert, J. Du, **D. Rhee**, V.A. Akhavan, R.D. Schaller, B.A. Korgel, "Multiexciton Solar Cells of $CuInSe_2$ Nanocrystals," *J. Phys. Chem. Lett.* **2014**, 5, 304-309. DOI: 10.1021/jz402596v

13. M.G. Panthani, C.J. Stolle, D.K. Reid, **D. Rhee**, T.B. Harvey, V.A. Akhavan, Y. Yu, B.A. Korgel, "CuInSe$_2$ Quantum Dot Solar Cells with High Open Circuit Voltage," *J. Phys. Chem. Lett.* **2013**, 4, 2030-2034. DOI: 10.1021/jz4010015

14. C. Chung, **D. Rhee**, D. Yoo, M. Choi, S. Heo, D. Kim, C. Choi, "Properties of Kesterite Cu$_2$ZnSnS$_4$ (CZTS) Thin Films Prepared by Sol-Gel Method Using Two Types of Solution," *J. Ceram. Process. Res.* **2013**, *14*, 255-259. Link

MANUSCRIPTS IN PREPARATION

1. **D. Rhee**, C. Machado, M.-K. Kim, Y.-S. Kim, N. Miljkovic, K.-C. Park, T.W. Odom, "Superhydrophobic Hierarchical Wrinkles Supporting Spatially Defined Water Condensation," In preparation In preparation

2. **D. Rhee**,[†] Y.-A.L. Lee,[†] T.W. Odom, "Multiscale Patterning of Two-Dimensional Materials by Wrinkling with Solution-Processible Skin Layers," In preparation. ([†]Equal contribution)

3. **D. Rhee**, W.-K. Lee, T.W. Odom, "Nanowrinkles: Fundamentals and Applications," In preparation

HONORS AND AWARDS

2018   Outstanding Research Awards from the International Institute for Nanotechnology
2014-2017   Scholarship from Jeongsong Cultural Foundation ($20,000 per year)
2013   Graduated 1st place in the College of Engineering at Hanyang University
2013   Summer Research Fellowship from the University of Texas at Austin
2008-2012   Academic Excellence Scholarship from Hanyang University

CONFERENCE PRESENTATIONS

1. "Graphene Wrinkles with Area-Specific Wavelengths and Switchable Orientations," Oral presentation, *Hilliard Symposium at Northwestern University*, Evanston, IL, USA. (May 21, 2020)

2. "Crack-Free, Area-Specific Graphene Wrinkles with Switchable Orientation on Soft Skin Layers," Oral presentation, *MRS Fall Meeting*, Boston, MA, USA. (Dec 1-6, 2019)

3. "Conformal Graphene Wrinkles with Switchable Orientation on Soft Skin Layers," Poster presentation, *IMECE*, Salt Lake City, UT, USA. (Nov 8-14, 2019)

4. "Functional and Hierarchical Nanoscale Metamaterials," Poster presentation, *Vannevar Bush Faculty Fellowship 10th Anniversary*, Washington, USA. (Apr 9-10, 2018)

5. "Switchable Anisotropic Wetting on Crack-Free, Soft Wrinkles," Oral presentation, *MRS Fall Meeting*, Boston, MA, USA. (Nov 26 - Dec 1, 2017)

6. "Properties of Cu$_2$ZnSnS$_4$ Thin Films Prepared by Sol-Gel Method Using Two Types of Solution," Poster presentation, *IUMRS-ICA*, Busan, South Korea. (Aug 26-31, 2012)

SKILLS

Miro/nano fabrication techniques
Soft lithography, photolithography, 2D material transfer, plasma etching, wet etching, focused ion beam milling, physical vapor deposition techniques, spin coating

Materials characterization and spectroscopy
Raman spectroscopy, x-ray photoelectron spectroscopy, ellipsometry, nanoindentation, thin film x-ray diffraction measurement, UV-vis spectroscopy, FT-IR spectroscopy, water contact angle measurement, Hall effect measurement, current-voltage testing

Microscopy
AFM, SEM, TEM, and fluorescence microscopy

Other experimental skills
Wrinkle fabrication, directed self-assembly of nanoparticles, bacteria culture

Computer skills
MATLAB, Python, Origin, Blender, Adobe Illustrator, Adobe Photoshop, Microsoft Office

LEADERSHIP POSITIONS

2018-	Nanowrinkles subgroup leader, the Odom group
2018-	Surface modification subgroup leader, the Odom group
2016-2017	Board member, Korean Student Association at Northwestern University
2015-2016	President, Korean Student Association at Northwestern University
2008-2009	Board member, Ars Amangdi (student hiphop dance team at Hanyang University)

COMMUNITY/VOLUNTEER SERVICES

1. "NU SPLASH: Nanoscience in everyday life," Sample fabrication, Northwestern University, Evanston, IL, USA. (Apr 8, 2018)
2. "All Scout Nano Day," Experimental demo, Northwestern University, Evanston, IL, USA. (Apr 8, 2017)
3. "All Scout Nano Day," Experimental demo, Northwestern University, Evanston, IL, USA. (Apr 9, 2016)
4. "KSEA-MW Open Seminar Series," Research presentation, Korean-American Scientists and Engineers Association, Chicago, IL, USA. (Mar 11, 2016)